



University of Kentucky
UKnowledge

Theses and Dissertations--Chemical and
Materials Engineering

Chemical and Materials Engineering

2019

SYNTHESIS, FUNCTIONALIZATION, AND APPLICATION OF NANOFILTRATION AND COMPOSITE MEMBRANES FOR SELECTIVE SEPARATIONS

Andrew Steven Colburn

University of Kentucky, andrew.colburn@uky.edu

Digital Object Identifier: <https://doi.org/10.13023/etd.2019.114>

[Right click to open a feedback form in a new tab to let us know how this document benefits you.](#)

Recommended Citation

Colburn, Andrew Steven, "SYNTHESIS, FUNCTIONALIZATION, AND APPLICATION OF NANOFILTRATION AND COMPOSITE MEMBRANES FOR SELECTIVE SEPARATIONS" (2019). *Theses and Dissertations--Chemical and Materials Engineering*. 98.

https://uknowledge.uky.edu/cme_etds/98

This Doctoral Dissertation is brought to you for free and open access by the Chemical and Materials Engineering at UKnowledge. It has been accepted for inclusion in Theses and Dissertations--Chemical and Materials Engineering by an authorized administrator of UKnowledge. For more information, please contact UKnowledge@lsv.uky.edu.

STUDENT AGREEMENT:

I represent that my thesis or dissertation and abstract are my original work. Proper attribution has been given to all outside sources. I understand that I am solely responsible for obtaining any needed copyright permissions. I have obtained needed written permission statement(s) from the owner(s) of each third-party copyrighted matter to be included in my work, allowing electronic distribution (if such use is not permitted by the fair use doctrine) which will be submitted to UKnowledge as Additional File.

I hereby grant to The University of Kentucky and its agents the irrevocable, non-exclusive, and royalty-free license to archive and make accessible my work in whole or in part in all forms of media, now or hereafter known. I agree that the document mentioned above may be made available immediately for worldwide access unless an embargo applies.

I retain all other ownership rights to the copyright of my work. I also retain the right to use in future works (such as articles or books) all or part of my work. I understand that I am free to register the copyright to my work.

REVIEW, APPROVAL AND ACCEPTANCE

The document mentioned above has been reviewed and accepted by the student's advisor, on behalf of the advisory committee, and by the Director of Graduate Studies (DGS), on behalf of the program; we verify that this is the final, approved version of the student's thesis including all changes required by the advisory committee. The undersigned agree to abide by the statements above.

Andrew Steven Colburn, Student

Dr. Dibakar Bhattacharyya, Major Professor

Dr. Stephen Rankin, Director of Graduate Studies

SYNTHESIS, FUNCTIONALIZATION, AND APPLICATION
OF NANOFILTRATION AND COMPOSITE MEMBRANES FOR SELECTIVE
SEPARATIONS

DISSERTATION

A dissertation submitted in partial fulfillment of the
requirements for the degree of Doctor of Philosophy in the
College of Engineering
at the University of Kentucky

By
Andrew Steven Colburn
Lexington, Kentucky
Director: Dr. Dibakar Bhattacharyya, Alumni Professor of Chemical Engineering
Lexington, Kentucky
2019

Copyright © Andrew Steven Colburn 2019

ABSTRACT OF DISSERTATION

SYNTHESIS, FUNCTIONALIZATION, AND APPLICATION OF NANOFILTRATION AND COMPOSITE MEMBRANES FOR SELECTIVE SEPARATIONS

Future nanofiltration (NF) membranes used for selective separations of ions and small organic molecules must maintain performance in environments where high concentrations of total dissolved solvents or foulants are present. These challenges can be addressed through the development of composite membranes, as well as the engineering of enhanced surface properties and operating conditions for existing commercial membranes.

In this work, ion transport through commercial thin film composite (TFC) polyamide NF membranes were studied in both lab-prepared salt solutions and industrial wastewater. The dependence of several variables on ion rejection was investigated, including ion radius, ion charge, ionic strength, and temperature. The impact of scaling and increasing ionic concentration on membrane performance during recovery of industrial wastewater was investigated. Fouling of the membrane surface was reduced by enhancing commercial NF membrane surfaces via aqueous-phase esterification of lignin sulfonate.

NF membranes were also created utilizing an ionic liquid solvent (1-ethyl-3-methylimidazolium acetate) to integrate composite materials into cellulose. Composite materials such as graphene oxide quantum dots, iron III particles, and lignin have been shown to interact strongly with cellulose in solution with ionic liquid and bind together cellulose chains via hydrogen bonds following nonsolvent induced phase inversion. Studies suggest the composite materials modify membrane surface chemistry and improve selectivity of small organic molecules (~300 nm) while allowing for the complete passage of ions.

KEYWORDS: Nanofiltration, Ion Transport, Desalination, Cellulose, Graphene,
Industrial Wastewater

Andrew Steven Colburn

(Name of Student)

1/14/2019

Date

SYNTHESIS, FUNCTIONALIZATION, AND APPLICATION
OF NANOFILTRATION AND COMPOSITE MEMBRANES FOR SELECTIVE
SEPARATIONS

By
Andrew Steven Colburn

Dr. Dibakar Bhattacharyya

Director of Dissertation

Dr. Stephen Rankin

Director of Graduate Studies

1/14/2019

Date

DEDICATION

Dedicated to my wife, Lauren, who has walked through this period of life with me, giving me the strength, I didn't have during the most difficult days of my PhD research. I thank God for you every day.

Revelation 21:6 "Then he said to me, "It is done! I am the Alpha and the Omega, the beginning and the end. To the thirsty I will give water as a gift from the spring of the water of life."

ACKNOWLEDGMENTS

First and foremost, I'd like to recognize my advisor, Professor Dibakar Bhattacharyya for his mentorship during my PhD study. Dr. DB inspired me to pursue my PhD in chemical engineering, and his passion for his work is truly inspiring. I am thankful for all the opportunities Dr. DB has given me including conferences, road trips to meet with industrial collaborators, and the hours of time he has dedicated toward helping me improve my publications and grow as a scientist. I consider Dr. DB family, and hope that continues.

I would also like to thank my committee members: Professor Doo Young Kim, Professor Isabel Escobar, and Professor Barbara Knutson. It has been an honor to work with Doo Young for part of this research, and I greatly appreciate his scientific input as well as his assistance in improving my technical writing. I am thankful for the energy that Dr. Escobar has brought to the seventh floor of FPAT since coming here, even if she did appropriate my old office. It's been great to get to know and work with her lab group, and the Center of Membrane Sciences is much better with her. Dr. Knutson has taught several of my classes, which had academic highs and lows, but beyond that I appreciate her mentorship over the course of my dissertation.

My research was supported through NSF KY EPSCoR program (Grant number: 1355438) and NIH-NIEHS-SRC (Award number: P42ES007380). Industrial partners such as Southern Company, Chevron, and UOP Honeywell have also contributed valuable funding to make this work possible. Thank you to the North American Membrane Society,

the University of Kentucky, and AIChE for travel grants that have made it possible to share my research at conferences.

I'd like to recognize my colleagues in lab. I've been very fortunate to work with some high-class researchers and good friends. It's been a great experience collaborating with Namal Wanninayake to really do some exciting research with cellulose composite membranes. I also thank Dr. Steven Weinman for his collaboration in nanofiltration studies and continued friendship over the years. Ashish Aher has been a consistent source of intellectual discussion, and he has made it possible to tackle the challenge of ion transport during nanofiltration. Xiaobo Dong has been a good office-mate, friend, and source for scientific discussion. Hongyi Wang has been an invaluable source for microscopy assistance and has often restored lab morale with tea breaks. It has been great to see Saiful Islam, John Craven, and John Miles grow into excellent researchers. I am also grateful for my former labmates: Dr. Sebastian Hernandez, Dr. Minghui Gui, Dr. Li Xiao, and Andrew Tomaino for mentoring and training me when I came into the lab. I'm also grateful for the undergraduates who have contributed to this work: Alex Whitehead, Jordan Wells, Fox Thorpe, Joseph Tapia, Aum Patel, Victoria Klaus, Mariah Bezold, and RJ Vogler.

I want to thank Dali Qian, Nicolas Briot, and Azin Akbari of Electron Microscopy Center, University of Kentucky for providing support for electron microscopy. Jiazhi Hu and Professor Y.T. Cheng's lab have provided assistance in understanding viscosity of casting solutions. Kirtley Amos and Dr. Seth DeBolt's lab at the University of Kentucky provided support for confocal fluorescence spectroscopy. Dow FilmTec and Solecta Membranes have provided membrane materials and backing for study in this research. Tricia Coakley, Megan Combs, and John May from the Environmental Research and

Training Laboratory for assistance with ion analysis.

The departmental staff have been of major assistance to me during my PhD research. I am thankful for all the help Chelsea Hansing, Marlene Spurlock, and Josh Duruttya have provided with travel reimbursement and ordering. Melissia Witt provided encouragement (and candy). Bruce Cole, in addition to having the best decorated office at UK, has advised me throughout my college career. Dr. Dziubla and Dr. Kalika were major supporters of MACE and are doing great things for the department. Thanks also go to Nancy Miller, Nick Cprek, and Dr. Rankin.

And lastly, I'd like to thank my family for their support during my PhD. Both the Colburns and the Bowmans have been there to support my wife and I through our time in graduate school. We love you and are so thankful for you.

TABLE OF CONTENTS

ACKNOWLEDGMENTS	iv
LIST OF TABLES.....	x
LIST OF FIGURES.....	xi
CHAPTER 1. INTRODUCTION AND BACKGROUND	1
1.1 <i>Introductory Remarks.....</i>	<i>1</i>
1.2 <i>General Background.....</i>	<i>2</i>
1.2.1 Nanofiltration Membranes.....	2
1.2.2 Nanofiltration Applications	4
1.2.3 Ion Transport in Nanofiltration Membranes	5
1.2.4 Interfacial Polymerization	6
1.2.5 Cellulose Based Membranes	8
1.2.6 Graphene Oxide Quantum Dots	9
1.3 <i>Objectives and Outlines.....</i>	<i>11</i>
CHAPTER 2. OVERVIEW OF GENERAL METHODS	13
2.1 <i>Zeta Potential Analysis.....</i>	<i>13</i>
2.2 <i>Contact Angle Measurement by Drop Shape Analysis</i>	<i>15</i>
2.3 <i>Membrane Equations.....</i>	<i>16</i>
2.4 <i>Stirred Tank Membrane Study</i>	<i>17</i>
2.5 <i>Crossflow Membrane Study</i>	<i>18</i>
CHAPTER 3. ION TRANSPORT DURING NANOFILTRATION OF SINGLE AND MIXED SALT SOLUTIONS.....	20
3.1 <i>Introduction.....</i>	<i>20</i>
3.2 <i>Experimental Methods and Theory</i>	<i>21</i>
3.2.1 Membranes and Solutions.....	21
3.2.2 Experimental Apparatus and Methods.....	22
3.2.3 Sample Analysis	23
3.2.4 Model for Ion Transport	23
3.3 <i>Results and Discussion</i>	<i>26</i>
3.3.1 Characterization of PNF2A Membrane Surface.....	26
3.3.2 Ion Rejection in Synthetic Single Salt Solutions.....	29
3.3.3 Ion Rejection in Synthetic Mixed-Salt Solutions.....	31
3.3.4 Ion rejection as a function of ionic strength.....	33
CHAPTER 4. NANOFILTRATION FOR INDUSTRIAL WASTEWATER TREATMENT	36
4.1 <i>Introduction.....</i>	<i>36</i>
4.2 <i>Experimental</i>	<i>36</i>
4.2.1 Commercial NF Membranes.....	36

4.2.2	Plant Bowen Flue Gas Desulfurization Wastewater	37
4.2.3	High TDS Produced Water	38
4.2.4	Nanofiltration apparatus and methods.....	39
4.2.5	Analysis of Samples	41
4.2.6	Naphthenic acid (NA) separation by nanofiltration (NF):.....	42
4.3	<i>Results and Discussion</i>	43
4.3.1	Partial Desalination of High TDS Scrubber Wastewater	44
4.3.2	High Water Recovery of Scrubber Wastewater.....	46
4.3.3	Gypsum formation.....	49
4.3.4	Retentate and Overall Permeate Concentration During Water Recovery	51
4.3.5	Long Term Module Stability	53
4.3.6	Heavy Metal Remediation	55
4.3.7	Naphthenic Acid Removal from Produced Wastewater.....	58
4.4	<i>Conclusions</i>	62
CHAPTER 5. CELLULOSE GRAPHENE QUANTUM DOT COMPOSITE MEMBRANES FOR SELECTIVE SEPARATIONS 64		
5.1	<i>Introduction</i>	64
5.2	<i>Experimental Methods</i>	67
5.2.1	5.2.1 Materials.....	67
5.2.2	5.2.2 GQD Synthesis	68
5.2.3	Cellulose membrane preparation.....	68
5.2.4	GQD cellulose acetate membrane.....	69
5.2.5	GQD Cellulose membrane preparation	69
5.2.6	Casting Solution Viscosity	70
5.2.7	Quantification of GQD loaded on the membrane	70
5.2.8	Zeta potential characterization	70
5.2.9	Contact angle characterization.....	71
5.2.10	Confocal Fluorescence Microscopy	71
5.2.11	Determination of Membrane Morphology.....	71
5.2.12	Membrane Performance	72
5.2.13	GQD Leaching in GQD cellulose membranes.....	72
5.2.14	XRD characterization of microcrystalline cellulose and composite membranes.....	73
5.3	<i>Results and Discussion</i>	73
5.3.1	GQD Characterization	73
5.3.2	Interaction between Cellulose and GQD in Ionic Liquid.....	77
5.3.3	Leaching of GQD during Phase Inversion	80
5.3.4	Morphology of GQD-Cellulose Composite Membrane.....	83
5.3.5	ATR-FTIR characterization of membrane post phase inversion	86
5.3.6	Membrane Surface Properties	88
5.3.7	Water Permeability	95
5.3.8	Rejection of Model Dye	97
5.3.9	Methylene Sorption in Membranes	104
5.3.10	Long Term Study.....	106
5.4	<i>Conclusion</i>	108
CHAPTER 6. FURTHER ADVANCEMENTS IN CELLULOSE COMPOSITE MEMBRANES AND LIGNIN FUNCTIONALIZED NANOFILTRATION MEMBRANES..... 110		
6.1	<i>Introduction</i>	110

6.2	<i>Experimental</i>	111
6.2.1	Materials	111
6.2.2	Cellulose Composite Membranes	112
6.2.3	Zeta potential characterization	113
6.2.4	Contact angle characterization	113
6.2.5	Membrane Performance	114
6.2.6	Divalent Ion Capture by Cellulose-PAA Membranes	114
6.2.7	Lignin Sulfonate Functionalized Nanofiltration Membrane	115
6.2.8	Bacteria Fouling Studies	116
6.3	<i>Results and Discussion</i>	117
6.3.1	Summary of Membranes	117
6.3.2	Iron Cellulose Composite Membranes	118
6.3.3	Poly Acrylic Acid Cellulose Composite Membranes	124
6.3.4	Lignin Cellulose Composite Membranes	129
6.3.5	Lignin Functionalized Nanofiltration Membrane	131
6.4	<i>Conclusion</i>	136
CHAPTER 7. CONCLUSIONS		137
7.1	<i>Key Advancements to Science and Engineering</i>	137
7.2	<i>Specific Accomplishments</i>	138
7.2.1	Nanofiltration of mixed salt solutions	138
7.2.2	Selective Desalination for Industrial Wastewater Treatment	138
7.2.3	Cellulose composite membranes	139
7.3	<i>Future Work</i>	140
NOMENCLATURE		142
APPENDIX		144
	<i>M-file Nernst Planck Model</i>	144
	<i>Working file</i>	144
REFERENCES		149
VITA		160

LIST OF TABLES

Table 1.1 Monomers commonly used in interfacial polymerization. Copied with permission from Lau et al. ²⁵	7
Table 1.2 Primary methods of GQD synthesis with quantum yield. Copied from Zhou et al. with permission. ³⁶	10
Table 3.1: XPS surface characterization for O, N, and C performed for PNF2A membrane compared to literature values for DOW NF-270 membrane.	27
Table 3.2: Water Permeability and Single Salt rejection performance of selected commercial membranes and PNF2A. Operating pressure for NF3A, PNF2A, and NF4 was 10.3 bar. Feed pH 5-6.	30
Table 4.1: Concentration of various ions and trace metals in scrubber wastewater received from Plant Bowen, GA. Water pH= 4.5. Trace metal concentrations determined by inductively coupled plasma dynamic reaction cell mass spectrometry (ICP-DRC-MS) by Applied Speciation and Consulting LLC.	38
Table 4.2. Inorganic and organic analysis of produced water samples.	39
Table 4.3: Summary of organic and inorganic contents of oil sands produced water used in the study	42
Table 4.4: Feed, retentate, and overall permeate analysis for high water recovery operation of PNF2A membrane module.	48
Table 4.4 NF Rejection of Naphthenic acid and major ionic species in oil sands produced water.....	62
Table 5.1- Cellulose Ionic Liquid Membrane Performance	101
Table 5.2- Methylene Blue Sorption in Membranes.....	105
Table 6.1 Solute dyes tested for rejection.	112
Table 6.2 Composite membranes studied with compositions and relevant properties. ..	117
Table 6.3. Rejection of Na ₂ SO ₄ in unmodified NF 270 and lignin sulfonate functionalized NF 270.	134

LIST OF FIGURES

Figure 1.1. Key areas of NF membranes development and breakthrough technology.....	4
Figure 1.1. Interfacial polymerization in thin film composite polyamide membranes.....	8
Figure 2.1 Simplified schematic of flow channel for zeta potential analysis.	13
Figure 2.2. Zeta potential of a charged membrane surface (NF270) vs ionic strength (mM).	15
Figure 2.3. Contact angle and for a liquid drop on a solid surface.	16
Figure 2.4 Stirred cell setup for determination of membrane performance.....	18
Figure 2.5. Cross flow setup employed in studying ion transport through NF membranes and recovering industrial wastewater.....	19
Figure 3.1 Membrane unit for the experimental testing of 2514 scale NF Membrane modules.	23
Figure 3.2. XPS survey scan of PS35, NF3A, and PNF2A membranes.....	27
Figure 3.3 Zeta Potential of the Nanostone PNF2A and DOW NF-270 membranes vs. pH.	28
Figure 3.4. Ion rejection for mixed salt solutions as determined experimentally and by optimization of the extended Nernst Planck model. All salt solutions 2000 mg/L. pH=5.9.	31
Figure 3.5. PNF2A water flux and rejection data for 18 mM CaCl ₂ / 34.2 mM NaCl mixed salt solution. Operating temperature was 27°C. Feed pH was 5.9. Retentate flowrate was maintained at 10.1 L/min. Line denotes predicted trend.	32
Figure 3.6. PNF2A Water flux and rejection data for 14.1 mM Na ₂ SO ₄ / 34.2 mM NaCl mixed salt solution. Operating temperature was 27°C. Feed pH was 5.9. Retentate flowrate was maintained at 10.1 L/min. Line denotes predicted trend.	33
Figure 3.7: Rejection of Ca ²⁺ and Na ⁺ normalized using the single salt rejection in Table 1 vs. NaCl concentration as NaCl was progressively added into the mixed salt feed. Initial feed concentration is equal to 18 mM CaCl ₂ . Temperature = 28-30 degrees C. Retentate flowrate = 10.1 L/min. Feed pH = 6.	35
Figure 4.1. Nanofiltration apparatus for industrial wastewater recovery.	40
Figure 4.2: PNF2A ion rejection for Plant Bowen scrubber wastewater. Experiment performed at 25°C. Operating pressure was held at 13.45 bar. Water flux was observed to be 32.2 LM. Feed pH = 4.5.	45
Figure 4.3: Water flux throughout high recovery operation of the PNF2A, NF3A, and NF4 membranes. Operating pressure maintained at 13.8 bar. Retentate flowrate maintained at 11.4 L/min. Tank temperature varied from 20-27°C. Feed pH= 4.5.	47
Figure 4.4: Retentate concentration during feed and bleed recovery of Plant Bowen scrubber water... Assume ΔP=13.8 bar and cross flow is maintained at 11.4 L/min. Feed pH =4.5.....	52

Figure 4.5: Overall permeate concentration during feed and bleed recovery of Plant Bowen scrubber water. Assume $\Delta P=13.8$ bar and cross flow is maintained at 11.4 L/min. Feed pH = 4.5.....	53
Figure 4.6. PNF2A Stability over the course of testing. Temperature varied throughout testing. Outlying values of high permeability were observed during high temperature runs (~44°C). Viscosity and osmotic pressure used to correct experimental data for comparison.....	54
Figure 4.7: PNF2A rejection of various trace metals in FGD process water from Plant Bowen. Water flux for PNF2A was 32.2 LMH. Temperature and operating pressure was maintained at 25°C and 13.45, respectively. Feed pH =4.5.	55
Figure 4.8. Selenium removal with iron functionalized membranes in different water matrix under convective flow condition. [Se] ₀ =1.3±0.1 mg/L in scrubber water, [Fe] ₀ =8.4 mg (20.7 % weight gain), [TDS] ₀ =12 g/L ([SO ₄ ²⁻] ₀ =11.7 mM or 1120 mg/L); [Se] ₀ =52.3 µg/L in NF permeate-1 (positively charged NF membrane), [Fe] ₀ =9.9 mg (23 % weight gain), [TDS] ₀ =2.4 g/L ([SO ₄ ²⁻] ₀ =292 µM or 28 mg/L); [Se] ₀ =11.0 µg/L in NF permeate-2 (negatively charged NF membrane), [Fe] ₀ =9.2 mg (23 % weight gain), [TDS] ₀ =0.92 g/L ([SO ₄ ²⁻] ₀ =0.094 µM or 9 mg/L); [Se] ₀ =2±0.2 mg/L in DI water, [Fe] ₀ =4.0 mg (12.5 % weight gain). pH of feed solution: 4.5-5.5.	57
Figure 4.9. Process for combine TDS removal and Se capture for FGD scrubber water reuse and remediation.	57
Figure 4.10. Schematic of suggested use of NF and Iron Functionalized Membranes for naphthenic acid concentration and degradation from high-TDS produced water. ...	59
Figure 4.11: Naphthenic acid (NA) rejection by nanofiltration membranes from different water matrices. Synthetic solution: NA concentrations: synthetic solution (mixture from Sigma-Aldrich dissolved in produced water): 38 mg/L, DI solution: 48 mg/L, Produced water: 34 mg/L.....	60
Figure 4.12: Flux of produced water through nanofiltration membrane with increasing water recovery (filtration cell operated at dead end mode, pressure: 10.3 bar, temperature: 22oc). Insert: Flux of produced water through nanofiltration membranes for 20 hours at 0% recovery (filtration cell operated at crossflow mode, Pressure: 6.8 bar, temperature: 22oc)	61
Figure 5.1. Schematic of dissolution of GQD and Cellulose in ionic liquid and subsequent casting of GQD cellulose membrane.	69
Figure 5.2. Typical Structure and Functional Groups of GQDs.	74
Figure 5.3. Solutions a) 2 mg/ml GQD, b) 1-Ethyl-3-Methylimidazolium Acetate c) 2 mg/ml GQD in 1-Ethyl-3-Methylimidazolium Acetate under visible and short-wave UV light. As can be seen the GQD are readily soluble in water and ionic liquid, fluorescing under excitation with UV light.	75
Figure 5.4: UV-Visible absorption spectrum of a GQD suspension	75

Figure 5.5 TEM image of GQDs, HRTEM of a GQD (top left and bottom), GQD size distribution histogram (top right), and IR (bottom inset).	76
Figure 5.6: XPS spectrum of GQD (a) Survey spectrum. (b) C1s spectrum.	77
Figure 5.7 Viscosity vs Shear Rate (1/s) for dope solutions (10 wt% Avicel PH-101 in 1-ethyl-3-methylimidazoliumacetate) with 0, 0.025, and 0.05 wt% of GQD added. Known viscosity denoted by dotted line. Average viscosity of 1-ethyl-3-methylimidazoliumacetate solvent was 0.098 Pa s.....	79
Figure 5.8 : (Left) Absorbance vs. Wavelength for GQD calibration solutions with ionic liquid background. (Right) Calibration curve of absorbance vs. concentration verifying linear behavior.....	81
Figure 5.9. XRD analysis of the Cellulose and GQD Cellulose Membrane as compared to the Avicel – PH 101 powder.	82
Figure 5.10 a) SEM cross-section of unmodified cellulose membrane. b) SEM cross-section of GQD cellulose membrane. c) STEM cross-section of GQD cellulose membrane.....	84
Figure 5.11 TEM Cross-section of GQD/Cellulose with the relevant regions marked. ...	85
Figure 5.12: FT-IR analysis of membranes and precursor materials.....	87
Figure 5.13 Zeta Potential of Unmodified Cellulose and GQD Cellulose membranes. [KCl]=.01M. Flow channel thickness 100 μ m. Pressure range 0-400 mbar.	89
Figure 5.14. Contact angle of water (bars, left axis) and wt % GQD (diamonds, right axis) for the unmodified cellulose membrane and GQD cellulose hybrid membranes prepared using water and IPA gelation bath, respectively. All membranes soaked in IPA and air dried before testing.	91
Figure 5.16. <i>Top left insert.</i> a) 17 wt% Cellulose Acetate, 12 wt% water, 71 wt% acetone casting solution. b) Casting solution a) with .01 wt% GQD added. <i>Bottom left insert.</i> Resulting membranes made with solution a) and b). <i>Right figure.</i> Fluorescence microscopy (100x) of GQD cellulose membrane using 440nm light source.....	95
Figure 5.17. Volumetric Water Flux vs Pressure for GQD cellulose membrane as compared to unmodified cellulose membrane.	96
Figure 5.18. Rejection of model solute through selected membranes. Experiments performed @ 1.37 bar using Blue Dextran (1000 ppm) and Methylene Blue.....	99
Figure 5.19 UV-Vis absorbance of permeate solution through the GQD cellulose membrane (25°C water gelation) 10mL of DIUF permeated through the membrane at 1.4 bar. <i>Figure insert:</i> UV-Vis absorbance of known concentrations of GQD in DIUF and EMIMAc in DIUF respectively.	103
Figure 5.20 Measurement of ionic liquid absorbance at 300 nm vs. volume permeated through GQD cellulose membrane (25°C water gelation). Pressure 1.4 bar.	104
Figure 5.21 Unmodified Cellulose (A) and GQD Cellulose (B) membranes after soaking in 10 mg/L methylene blue solution for 24 hours and being rinsed for 30 min. GQD	

cellulose membrane (C) after passage of 300 mL of 100 mg/L 5kDa Blue Dextran solution included as reference.....	106
Figure 5.22 Long term study of water flux through GQD cellulose membrane (25°C water gelation) at an operating pressure of 1.38 bar.....	107
Figure 5.23 Rejection of 5kDa Blue Dextran by GQD cellulose (25°C Water Gelation) during long-term permeation study.....	108
Figure 6.1. Unmodified cellulose, GQD cellulose, and iron cellulose composite membranes.....	118
Figure 6.2. Flux (LMH) vs Pressure (bar) behavior for iron cellulose composite membranes in water, isopropanol (IPA), and neutral red in water.....	119
Figure 6.3. Viscosity Corrected Flux vs. Pressure for unmodified cellulose membrane (10 wt. %).....	121
Figure 6.4. Volumetric permeability of total solvent mixture as volume % of isopropanol is varied in iron cellulose composite membranes. Remaining volume % water. ...	122
Figure 6.5. Dye rejection in iron cellulose composite membrane in water and isopropanol solvent.....	123
Figure 6.6. Rejection of model dyes and molecules in Iron Cellulose composite membranes.....	124
Fig. 6.7. Zeta potential of PVDF 700, PVDF-PAA (weight gain of 7.28% with functionalization), cellulose (10 wt% cellulose in casting solution)1, and cellulose-PAA membranes in the pH range of 3-9.....	125
Figure 6.8. Permeability of cellulose-PAA membrane at pH 3 and 7. Membrane surface is 13.2 cm ²	126
Figure 6.9. Total Ca ²⁺ capture of a 13.2-cm ² cellulose-PAA membrane during convective flow of CaCl ₂ (overall flux = 89 LMH and average pressure of 50-mL increments = 0.72 bar) and of a PVDF-PAA membrane from literature after convective flow of CaCl ₂	128
Fig. 6.10 (a) Iron EDS map of the cross section of a PVDF-PAA-Fe sample and (b) Calcium EDS map of most of the cross section of a cellulose-PAA-Ca ²⁺ sample.....	129
Figure 6.11. Pressure dependent flux of lignin sulfonate membranes as compared to cellulose membranes.....	130
Figure 6.12. Bacteria growth on A) unmodified cellulose membrane and B) lignin cellulose membrane.....	131
Figure 6.13. Functionalization of commercial DowFilmtec NF270 membrane using heat to esterify lignin sulfonate to unreacted carboxyl groups.....	132
Figure 6.14 Pressure dependent water flux of unmodified NF270 and LS Functionalized membrane.....	133
Figure 6.15. Zeta potential vs. pH for lignin functionalized and pristine NF270 membrane. 100 mg/L KCl used as an electrolyte.....	134

Figure 6.16 . Normalized water flux of lignin sulfonate functionalized and unmodified NF270 during filtration of 100 mg/L BSA. Dotted lines indicate 10 minutes of tangential rinsing with deionized water (pH=5.6) 135

CHAPTER 1. INTRODUCTION AND BACKGROUND

1.1 Introductory Remarks

Water has often been thought of as an inexhaustible resource in many regions throughout the United States. However only 0.8% of the Earth's water is available in fresh water reserves¹. Recent droughts in Texas and Southern California along with contaminated water situation in Flint, Michigan and Toledo, Ohio have shown that usable water is a major concern even in areas where water resources were thought to be secure².³ Water security continues to be an issue in the developing world, and research has shown that water scarcity has been a source of conflict and water stewardship is of great importance in international relations⁴. Therefore, conversion of unusable water sources, including industrial, brackish, and salt water must be prioritizing to reduce the burden on regional and global water resources.

Since development in the 1960s, membranes have emerged as a promising technology for desalination and water recovery. Reverse osmosis membranes have been developed and refined to effectively desalinate brackish and seawater into potable water. While desalination of brackish and salt water is now a mature and commercialized technology, there are still opportunities for industrial wastewater treatment and reuse. Many industrial wastewater treatment applications only require separation of some of the solutes in solution, including ions contributing to water hardness, heavy metals, and organic solutes. Complete desalination of the water may not be required and may be energetically unfavorable. Nanofiltration (NF) membranes have been used for selectively removing hardness from industrial wastewater and removing pesticides molecules for

wastewater treatment⁵. In this work we look to better understand at ion transport during nanofiltration of mixed salt solutions and apply NF membranes for industrial wastewater recovery.

The selectivity of nanofiltration membranes can also be utilized for rejection of small organic molecules⁶. Commercial NF membranes have been implemented for diafiltration monovalent ions and concentration of small organic molecules in aqueous solutions⁷. Further potential for development lies in membranes that can selectively reject small organic molecules such as active pharmaceutical ingredients while allowing passage of monovalent and multivalent ions. Organic solvent compatibility is also a desired membrane property for further application in the pharmaceutical processes. This work seeks to address these challenges for small molecule separations through the development of cellulose composite membranes.

In this chapter the history of nanofiltration membrane development will be covered. Applications and synthesis of nanofiltration membranes will be discussed along with the current literature understanding of ion transport during desalination. Our specific contributions to the field of nanofiltration must be understood within the full picture of nanofiltration research. Further background on cellulose materials and methods will be addressed along with composite materials used in membrane synthesis.

1.2 General Background

1.2.1 Nanofiltration Membranes

Nanofiltration membranes were initially developed out of the interfacial polymerization chemistry that had been used to great commercial success in reverse osmosis. Requests for more selective membrane properties prompted manufacturers such

as FilmTec to modify the monomers used in interfacial polymerization to create a more open structure⁸. The first papers to use the phrase nanofiltration in the late 1980s describe membranes that, unlike RO, selectively reject based on charge and solute radius⁹. An additional benefit of this the new nanofiltration chemistry was higher water permeability, which made the technology attractive for lower pressure applications. Thin film composite nanofiltration membranes using this chemistry currently dominate the commercial market for nanofiltration. Recent research has focused on integrating composite materials such as graphene oxide or zwitterionic brushes into the thin film composite membrane membranes to improve membrane properties such as fouling resistance¹⁰. Commercial NF membranes also show a tendency to swell when exposed to organic solvents, thus work is being done on creating membranes out of polymers or materials such as graphene oxide that will be stable during organic solvent filtration¹¹⁻¹³. Nonsolvent induced phase inversion, a technology for membrane synthesis dating from the 1960s, has found new applications for casting solvent resistant nanofiltration membranes, as the technique allows for many different polymers to be prepared into membranes¹⁴. Beyond these technologies Figure 1.1 details future development of nanofiltration membranes beyond what has previously been discussed.

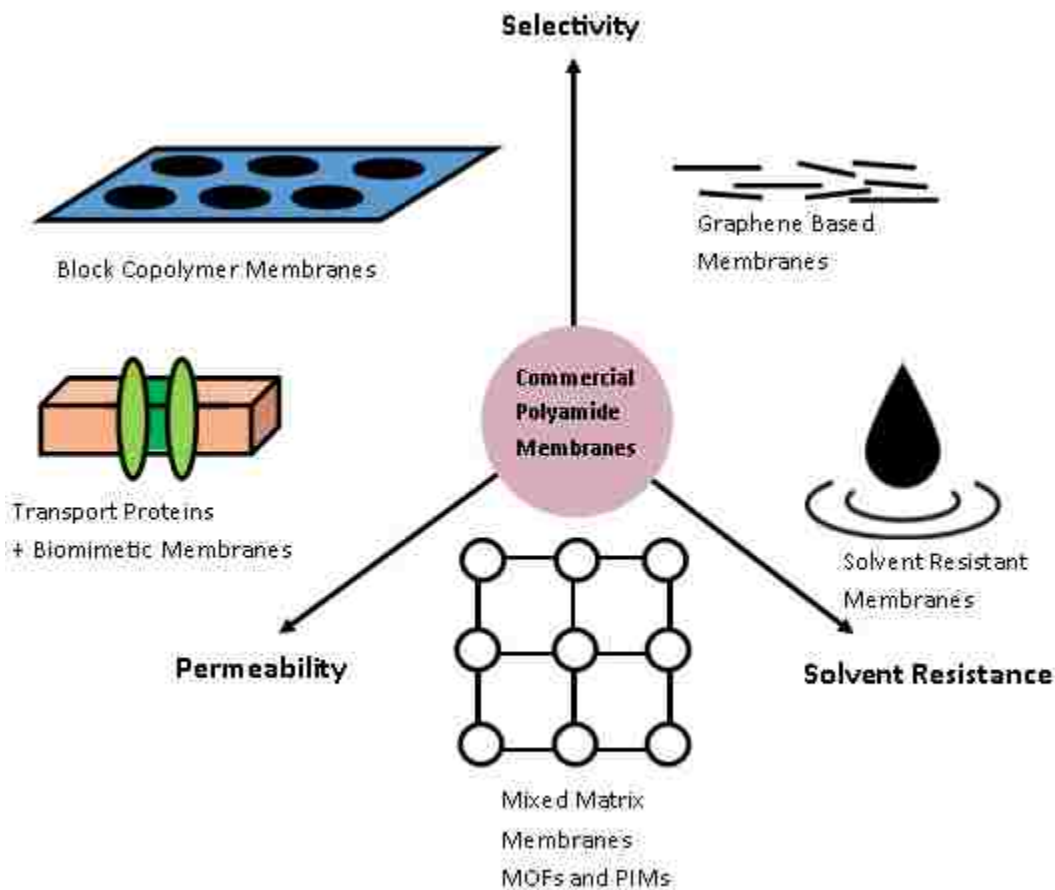


Figure 1.1. Key areas of NF membranes development and breakthrough technology.

1.2.2 Nanofiltration Applications

Nanofiltration membranes have seen wide application for treatment of several different types of wastewater. The selectivity of NF membranes to remove divalent ions such as Ca^{2+} while allowing partial or full passage of Na^+ lead to interest in water softening applications¹⁵. Request for these applications are a significant motivation for the development of NF membranes from RO. Molecular weight cut-off for most commercial NF membranes lies between 150-400 Da, allowing them to be utilized for removal of dyes from textile effluent¹⁶. The high permeability of monovalent ions through NF membranes

allow for removal of organics from high TDS produce water without incurring a osmotic penalty¹⁷. Nanofiltration (NF) membranes have been proven effective at rejecting (>90%) pharmaceuticals such as sulfamethoxazole, carbamazepine, and ibuprofen from DI water solutions¹⁸. Lactose and hardness removal by NF allows for reuse of dairy wastewater¹⁹.

In addition to wastewater treatment, NF membranes have also been used for concentration and purification applications. Selectivity for multivalent ions is advantageous for employing NF membranes for rare earth elements from coal fly ash for downstream extraction¹⁹.

1.2.3 Ion Transport in Nanofiltration Membranes

In the membrane community there is still no agreement on the exact structure of pores in the polyamide selective layer of nanofiltration membranes. Determination of membrane structure is complicated by the size scale of selectivity. Traditionally the solution diffusion model has been applied to describe solute transport through RO membranes²⁰. The structure of RO membranes is dense enough for the solution diffusion model to be valid. The small scale of selectivity complicates the understanding of the selective surface of the nanofiltration membrane. Other studies have applied the pore flow model with the assumption that solute transport through NF membranes can be understood as diffusion into and through a cylindrical pore of a given radius²¹. In the pore flow model, the classical Nernst-Planck equation has been modified to describe the effects of diffusion, electrical, and convection dependent transport through NF membranes²². The application of the modified Nernst-Planck equation will be further discussed in Chapter 2, as it pertains to ion selectivity in mixed salt solutions. Largely the emphasis on research in nanofiltration modeling has been in the areas of understanding partitioning into the membrane pores and

accurate determination of membrane parameters^{23, 24}. Our work expands on the current model research by predicting rejection in mixed salt solutions.

1.2.4 Interfacial Polymerization

The development of ultra-thin polyamide membranes through interfacial polymerization was a groundbreaking achievement that set the foundation for modern commercial desalination membranes²⁵. Diffusion of amine into an organic solution with acyl chloride or other highly reactive monomer results in formation of a dense polymeric membrane. The resulting membrane is referred to as a thin film composite membrane. As the membrane layer grows, it will eventually limit diffusion of amine, thus limiting the active layer to a thickness between 50-200 nm. Common monomers used in interfacial polymerization are given in Table 1.1. Among the most common monomers used for nanofiltration membranes are piperazine and trimesoyl chloride (TMC). While TMC is also used in reverse osmosis membrane, piperazine is less bulk than m-phenyldiamine used in reverse osmosis membranes and is critical for giving NF membranes selective separations properties. Because the interfacial polymerization layer is very thin, interfacial polymerization is done on an ultrafiltration membrane, so that the membrane is formed without defect and has structural reinforcement during pressure-based filtration. A schematic for interfacial polymerization in the nanofiltration membranes tested in this study is shown in Figure 1.2.

Table 1.1 Monomers commonly used in interfacial polymerization. Copied with permission from Lau et al.²⁵

Amine monomer (abbreviation)	Chemical structure	Molecular weight	Acyl chloride monomer (abbreviation)	Chemical structure	Molecular weight
Piperazine (PIP)		86.14	Trimesoyl chloride (TMC)		265.48
m-Phenylenediamine (MPD)		108.10	Isophthaloyl chloride (IPC)		203.02
p-Phenylenediamine (PPD)		108.10	5-tricyanato-isophthaloyl chloride (ICX)		244.04
Sulfonated cardo poly(arylene ether sulfone) (SPES-NH ₂) [19]		774.71	mm-Biphenyl tetracyl chloride (mm-BTEC) [18]		404.03
3,5-diamino-N-(4-aminophenyl) benzamide (DABA) [20]		242.27	om-Biphenyl tetracyl chloride (om-BTEC) [18]		404.03
Triethanolamine (TEOA) [21]		149.19	op-Biphenyl tetracyl chloride (op-BTEC) [18]		404.03
Methyl-diethanolamine (MDEGA) [22]		119.16	Cyclohexane-1,3,5-tricarbonyl chloride (HTC) [27]		271.53
1,3-cyclohexanedithiol (methylamine) (CHMA) [26]		142.24	5-chloroformyl-oxo-naphthaloyl chloride (CFX) [28]		281.48
m-phenylenediamine-4-methyl (MMPD) [27]		122.17			
Hexafluoroalcohol-m-Phenylenediamine (HFA-MPD) [28]		530.31			



Figure 1.2. Interfacial polymerization in thin film composite polyamide membranes.

It is important to note that in addition to hindered diffusion through the tightly crosslinked network, charge interaction in unreacted amine and carboxylic groups also dictate transport of solutes through nanofiltration membranes. Additives like mixed amines can be incorporated during interfacial polymerization to modify membrane surface charge and selectivity. Work is currently being done on creating alternating charge in NF membranes by performing layer by layer interfacial polymerization to create alternating positive and negative areas of surface charge²⁶. Other work is looking to increase selectivity and permeability of thin film composite membranes by integrating water selective transport proteins into the structure²⁷

1.2.5 Cellulose Based Membranes

Archaeological evidence suggests cotton cellulose was first used for textile making in the 6th millennium BC in modern day India and Pakistan²⁸. Eventually use of cotton for textiles spread globally, and cotton was a major textile material. Industrialization of textile

manufacturing in Britain combined with exploitation of colonial holdings led to wide scale textile manufacturing from cotton²⁹. While one can argue that clothing itself is indeed a membrane, cellulose based textiles have been proven as an effective filtration material. Sari cloth has been shown effective at remove 99% of *V. cholerae*, cholera causing bacteria that attach to algae clusters allowing for effective filtration³⁰. Cellulose based polymers would find themselves among the first materials used in membrane manufacture as cellulose acetate³¹. Unfortunately, cellulose itself is not soluble in commercial solvents, so regenerated cellulose materials were developed by use of NaOH or NMMO to modify cellulose fibers for dispersion, then restoration of cellulose structure by rinsing or drying after the material was formed³². Recent developments and molecular dynamic studies have identified ionic liquids such as 1-ethyl-3-methylimidazolium acetate as being among the most promising solvents for cellulose, even with water present³³. Ionic liquids have been used for dissolution and preparation of nanofiltration membranes³⁴.

1.2.6 Graphene Oxide Quantum Dots

After the Nobel prize winning discovery of 2D carbon materials, known as graphene, by Novoselov et al. there has been immense interest in the utilization of 2D carbon materials³⁵. Graphene quantum dots are an oxidized derivative of graphene, small enough in size (1-10 nm) to exhibit quantum confinement. They are either prepared through a top-down oxidation of a larger carbon source or bottom up construction from smaller building blocks like citric acid. Table 1.2 gives an overview of GQD synthesis methods. Out of these methods chemical oxidation is among the most scalable, as carbon materials for oxidation are widely available.

Table 1.2 Primary methods of GQD synthesis with quantum yield. Copied from Zhou et al. with permission. ³⁶

Methods	Sub classification	Quantum yield (QY)
Top-down	Chemical oxidation	27.5%
Top-down	Electrochemical exfoliation	14%
Top-down	Hydrothermal/solvothermal treatment	18.6%
Top-down	Microwave assisted method	70%
Bottom-up	Carbonization of organic precursors	78%
Bottom-up	Step organic synthesis of GQDs	2%
Bottom-up	High pressure and high temperature	86%

Initial studies have sought to utilize fluorescent properties of GQDs for medical imaging or photoionic sensing applications³⁷⁻³⁹. Further studies have shown GQDs exhibit antibacterial behavior generating of oxidative species and puncturing bacteria cell walls with the sharp edges in the 2D material ^{40, 41}. Recent studies have sought to incorporate GQDs within the membrane or on the membrane surface to leverage the antibacterial and antifouling properties to enhance membrane performance⁴².

GQD are readily water soluble, and as a result, GQDs may be present in significant concentrations in the environment as a result of their application in materials development. Toxicity of GQDs must be considered when studying GQD use in material development. Hydrophobic interactions of graphene materials result in disruption of the lipid bilayer of cellular membranes. Red blood cells were observed to form abnormal structures when exposed to nitrogen doped GQDs. There was no observed reduction of ATP content or hemolysis in the red blood cells exposed to GQDs which suggests that the small size of GQD prevents hydrophobic interactions from extracting the lipid from the cell membrane as seen in larger graphene materials⁴³. There is further evidence that toxicity of GQD

increases with particle size as larger particles have greater hydrophobic interactions⁴⁴. Cellular uptake of GQDs due to endocytosis has been determined to be concentration and time dependent. GQD uptake was shown to have negligible effect on human neural stem cell metabolism and differentiation potential⁴⁵.

Generation of reactive oxidative species (ROS) is the primary toxicity concern when considering GQDs. ROS generation in GQDs is only observed to occur in the presence of light, indicating that GQD toxicity may be photo-dependent⁴⁶. The ketonic carbonyl groups of GQD have been seen to contribute most significantly to ROS generation⁴⁷. As ROS generation may not be able to be ruled out in all applications, removal of GQD from aqueous solutions must be considered for processing of GQD-containing materials. Coagulation of GQD at low pH could be utilized to assist in size based exclusion of GQD from wastewater⁴⁸. Adsorption of GQD onto activated carbon materials may also be considered as remediation mechanism for water containing GQD⁴⁹.

1.3 Objectives and Outlines

- Apply commercial NF and composite membranes for application in which selective separation for ions or organic molecules is desired and in doing so develop new methods for reusing industrial wastewater and efficiently purifying organic molecules.
- Understand how presence and concentration of monovalent and divalent ions have on ion transport in mixed salt solutions of various compositions. (Chapter 3)
- Predict membrane rejection of divalent and monovalent ions using the extended Nernst-Planck equation with steric partitioning. (Chapter 3)

- Apply knowledge in nanofiltration transport behavior to removing divalent ions while also concentrating heavy metal ions and organic pollutants for downstream removal to recover and reuse FGD wastewater and oil sands produced water. (Chapter 4)
- Integrate graphene oxide quantum dots into cellulosic polymer network using an ionic liquid cosolvent and study the impact of the composite material on resulting membrane properties. (Chapter 5)
- Apply composite membrane synthesis techniques to other materials such as iron, PAA, and lignin to further enhance membrane performance and create membranes with unique properties that can be utilized in filtration applications. (Chapter 6)
- Functionalize commercial nanofiltration membranes with lignin derived materials in a scalable approach to improve antifouling behavior of membranes. (Chapter 6)

CHAPTER 2. OVERVIEW OF GENERAL METHODS

2.1 Zeta Potential Analysis

Surface charge of membranes is an important property in studying membranes surface chemistry, verifying successful functionalization, or determining presence of composite materials at the membrane surface. The Anton Parr Surpass electrokinetic analyzer was utilized in this study. An electric double layer forms along a charge surface that is dependent on the magnitude of the charged surface. While electrostatic forces bind ions close to the membrane surface too tightly to be displaced, there is a slip plane at a given distance where applied shear force will displace electrostatically adsorbed ions. Displaced ions create a potential in the flow channel which can be measured. In our studies we set the electrokinetic analyzer to apply and measure a back current (I) to neutralize any potential across the flow channel. A simplified schematic of the flow channel and subsequent measurement is given in Figure 2.1.

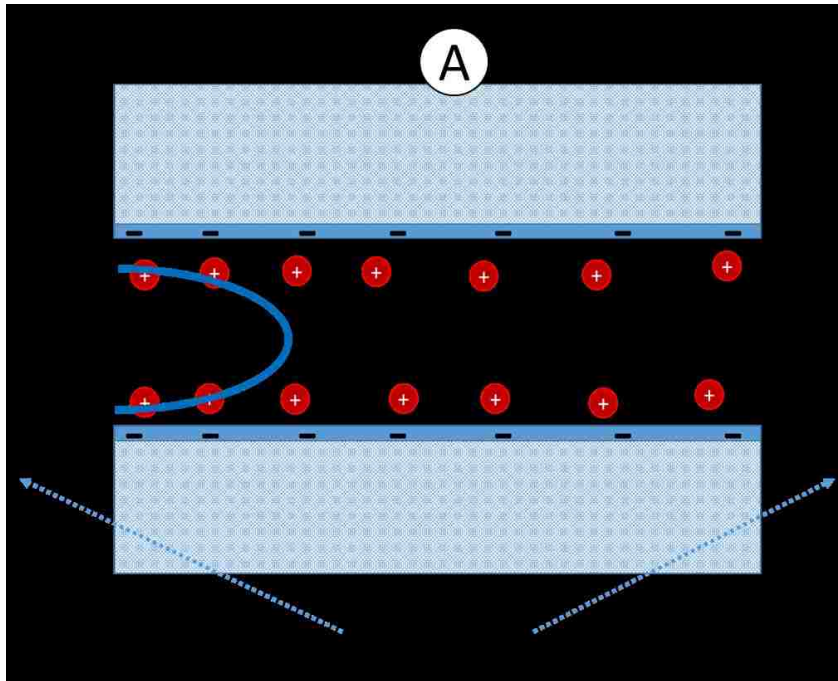


Figure 2.1 Simplified schematic of flow channel for zeta potential analysis.

As shear force, which ideally varies linearly with pressure, is increased in a channel additional ion are displaced. The slope of the current needed to neutralize the potential caused by displaced ions as pressure was increased was used to determine zeta potential, the charge at the slip plane in the electric double layer using a modification of the Helmholtz-Smoluchowski equation:

$$\zeta = \frac{dI_{str}}{d\Delta p} \times \frac{\eta}{\varepsilon \times \varepsilon_0} \times \frac{L}{A} \quad (2.1)$$

Where ζ is the zeta potential of the membrane. I_{str} is the streaming current or current needed to neutralize a potential formed by ion displacement from shear flow through the channel. Δp refers to the pressure drop in the channel. η is the dynamic viscosity of the electrolyte solution being passed through the channel. $\varepsilon \times \varepsilon_0$ refers to the dielectric coefficient of the electrolyte solution. L and A are simply the length and width of the channel.

The zeta potential at various pH values is dependent on the pKa of the functional groups. Zeta potential analysis unlike Fourier Transform Infra-Red Spectroscopy, is surface specific. That said, care must be taken to account for flow that might be travelling through more porous media. This may cause an erroneously large magnitude of charge to be measured for the material in question. Ionic strength may also be modified in the electrokinetic analyzer channel to study effective surface charge in different electrolyte environments. As shown in Figure 2.2 zeta potential decreases as ionic strength decreases due to ion shielding reducing the Debye length of the membrane. It is also important to know that instrument error increases as ionic strength increases due to increased conductivity of the electrolyte.

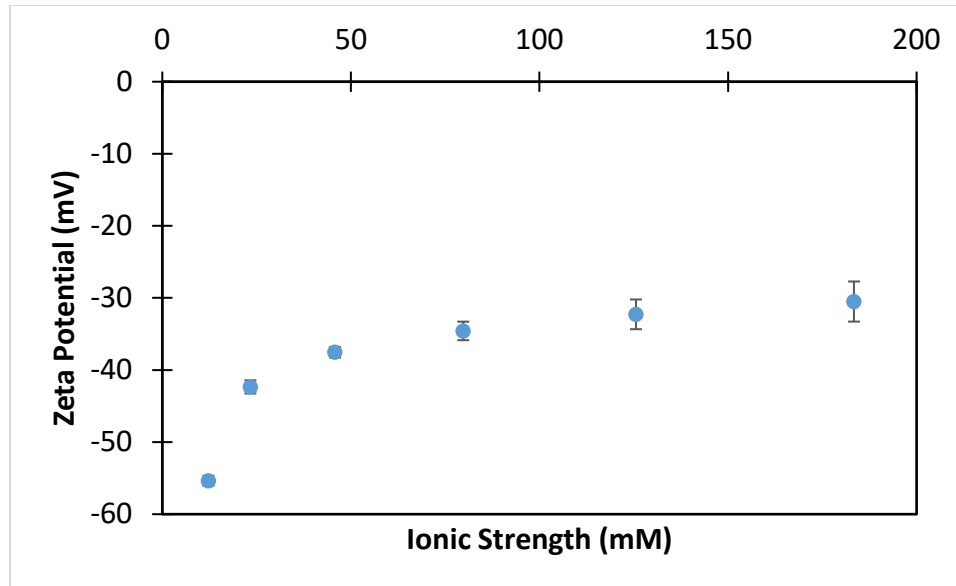


Figure 2.2. Zeta potential of a charged membrane surface (NF270) vs ionic strength (mM).

2.2 Contact Angle Measurement by Drop Shape Analysis

Contact angle has been used in these studies as a nondestructive way of determining surface chemistry of membranes and confirming functionalization. Generally, the as contact angle approaches zero, the surface chemistry is considered more hydrophilic. As the contact angle approaches 90 degrees the surface is viewed as hydrophobic. The relation of contact angle on surface tension of a solid liquid interface is given by Young’s equation.

$$\sigma_s = \sigma_{sl} + \sigma_l \cos\theta \quad (2.2)$$

Where σ_s is the surface tension of the solid (membrane, film, coating, etc.), σ_l is the surface tension of the liquid, and σ_{sl} is the surface tension and the solid liquid interface.

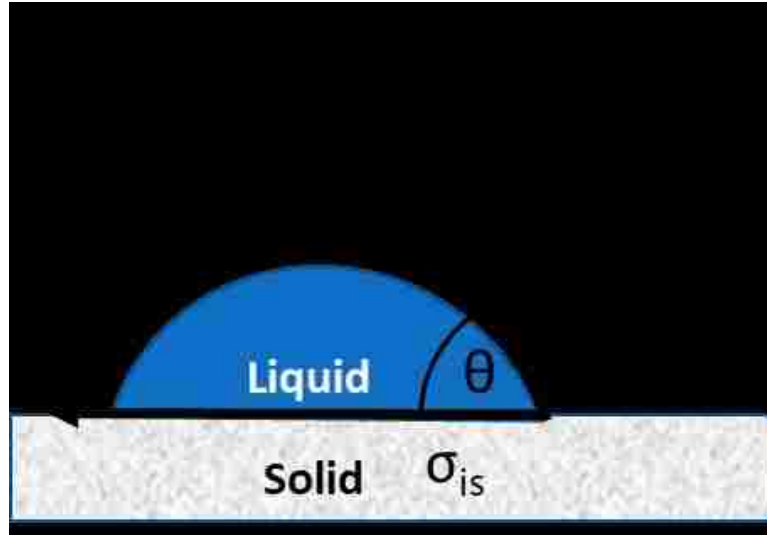


Figure 2.3. Contact angle and for a liquid drop on a solid surface.

2.3 Membrane Equations

For the various feed solutions, the membranes were characterized by volumetric flux and the rejection of various species. Rejection, for a given species i , is given by equation 2.2.

$$R_i = 1 - \frac{C_{i,p}}{C_{i,b}} \quad (2.2)$$

$C_{i,b}$ and $C_{i,p}$ correspond to the ion concentration of a species i in the bulk feed and the rejection respectively. Volumetric water flux, given by J_w , is related to the water permeability of the membrane by equation 2.3.

$$J_w = A(\Delta P - \Delta \Pi) \quad (2.3)$$

A , a constant, is defined as the water permeability of a membrane, presented in this work in units of LMH/bar. ΔP is the transmembrane pressure.

$$J_s = J_w C_{i,p} \quad (2.4)$$

Solute flux J_s through the membrane is related to the water flux and permeate concentration through a material balance on a specific ion, i .

The Van' t Hoff relation is used to determine osmotic pressure ($\Delta\Pi$) at ideal conditions, as seen in equation 4.

$$\Delta\Pi = R_g T \sum_i^n C_{i,b} R_i \quad (2.5)$$

Where R_g is the gas constant and T is temperature. This equation has been modified with the inclusion of the rejection term R_i , rejection of ion I , to account for the partial ion rejection on the osmotic pressure. $C_{i,b}$ is the bulk concentration of ion I in the feed. At higher concentrations of ions osmotic pressure deviates from the Van't Hoff relationship. Of course, one can use the well-known equation by relating osmotic pressure with water activity.

$$\Pi = -\frac{R_g T}{V} \ln(a_w) \quad (2.6)$$

Where V is the molar volume of water and a_w is the water activity. However, for this work, the Van't Hoff relation is determined to be sufficient to determine osmotic pressure in the concentration range between 10,000-30,000 mg/L TDS. At the beginning of recovery of scrubber water, the osmotic pressure calculated by the Van't Hoff relationship only varied by 6% compared to the observed value.

2.4 Stirred Tank Membrane Study

Stirred tank membrane cells were used to test performance for membranes created in lab, such as cellulose composite membranes. Membrane area for these tests were 13.2 cm². Mixing was achieved through a magnetic stir plate set at 300 rpm. The Sterlitech HP4750 cell holds 300 mL of solution and was used in our experiments to test membrane performance between 1-11 bar. Transmembrane pressure was set by pressurizing nitrogen

in the headspace of the pressure cell. Polar solvents and water are compatible using this setup shown in Figure 2.4.



Figure 2.4 Stirred cell setup for determination of membrane performance.

Flux was determined directly by electronic balance and samples were collected in centrifuge tubes as needed. Fifteen minutes were allowed before samples were collected after changing pressure to allow for the membrane to reach steady state. Flux was measured in triplicate and standard deviation was calculated to from the three measurements. One pressure was tested twice to ensure the membrane was stable throughout testing.

2.5 Crossflow Membrane Study

Spiral wound modules of commercial membranes were tested in crossflow setup to ensure consistent membrane performance over a long term of testing. Spiral wound

membrane area was 0.59 m^2 for the 2540 scale modules tested in this study. The schematic in Figure 2.5 depicts the cross flow set up in “feed and bleed mode” for water recovery. Water was collected in a separate container while only the retentate is returned to the feed tank, thus water is recovered at a flow rate equal to the permeate flowrate. For standard operation, the permeate is recycled back into the feed tank and no volume of water is lost during operation.

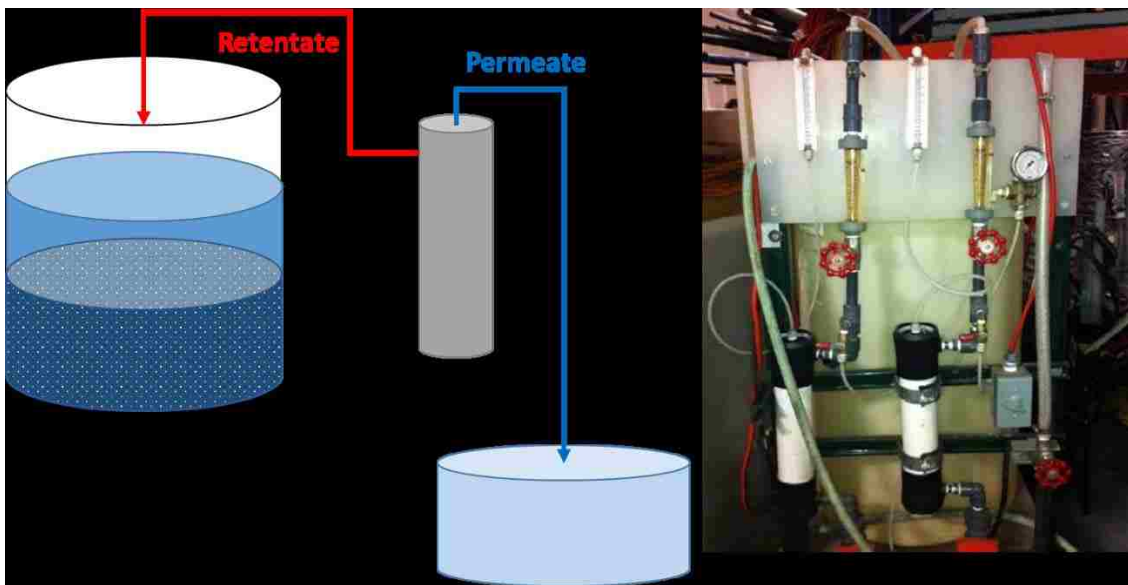


Figure 2.5. Cross flow setup employed in studying ion transport through NF membranes and recovering industrial wastewater.

The setup was tested for transmembrane pressures between 1-12 bar. Flux was measured through sampling with volumetric cylinders in triplicate. Thirty minutes were given in-between pressure changes for the system to reach steady state. Transmembrane pressure is controlled via the opening and closing of valves for retentate and bypass flow paths. Retentate flowrate was maintained around 10 L/min for most test to eliminate any effect of concentration polarization. Spiral wound elements tested in this have feed spacers that further enhance convective mass transport.

CHAPTER 3. ION TRANSPORT DURING NANOFILTRATION OF SINGLE AND MIXED SALT SOLUTIONS

3.1 Introduction

Cadotte et al, revolutionized membrane filtration with the development of the thin film composite membrane in 1980⁵⁰. Thin film composite (TFC) NF membrane is formed by the interfacial polymerization of an amine compound with an acyl chloride, resulting in a surface of 100-200 nm⁵¹. Presence of amine and carboxyl groups in TFC membranes result in a charge distribution throughout the membrane pores, which allows NF membranes to effectively reject ions which would not be rejected through size exclusion alone, thus maintaining a higher flux than denser reverse osmosis (RO) membranes.

Charged groups on the membrane surface repulse ions of like charge. Counter-ions to the repulsed ions are also rejected as charge must be conserved. This exclusion of ions, known as Donnan exclusion results from the impact of charge on equilibrium partitioning. Through Donnan exclusion, rejection of multivalent ions with like charge to the membrane is greater than that of monovalent ions or multivalent counter-ions (ions with opposite charge to the membrane)⁵². NF membranes have the potential to selectively separate ions depending on membrane charge and the valence states of the ions^{53, 54}. Therefore, NF membranes have relatively high ion rejection while maintaining greater water permeability than that of RO membranes. The confined nature of water at in membrane pore leads to dielectric exclusion. Repulsion from dielectric exclusion also contributes to ion rejection in a manner that is significantly more substantial for salts with divalent ions (1:2, 2:1, or 2:2) than for 1:1 monovalent salts⁵⁵. In summary Donnan exclusion occurs due to charge repulsion between the membrane surface and ions, while dielectric exclusion is dependent on the magnitude of charge only.

NF membranes have been proven to be effective at removing divalent ions from solution^{56, 57}. New polyamide-based composite hollow fiber NF membranes have been developed for low pressure water softening⁵⁸⁻⁶⁰. Work has been done to model the rejection behavior of NF membrane for mixed salt solutions^{61, 62}. The concentration polarization phenomenon in rejection of mixed salt solutions has also been studied⁶³. High water recovery (~85%) has been investigated for single salt solutions of NaCl/MgSO₄, and pre-treated lake water⁶⁴.

The goal of this work is to study ion rejection behavior of mixed salt solutions through NF membranes, with a focus on selective separations of mixed salt solutions through spiral wound NF membrane modules. Larger scale spiral-wound membrane modules (0.59 m² surface area) were used in testing to more accurately simulate industrial operating conditions and ensure consistency throughout testing.

Ion rejection phenomenon were studied for several synthetic single salt and mixed salt feed solutions. Selective rejection preferential to divalent ions was observed in PNF2A operation in both single salt and mixed salt synthetic solutions. The addition of similar concentrations of monovalent salt had minimal effects on the rejection of divalent ions, while the rejection of the ions making up the monovalent salt was reduced, becoming negligible at higher concentrations.

3.2 Experimental Methods and Theory

3.2.1 Membranes and Solutions

The PNF2A membrane studied was a charged polyamide thin film composite membrane developed in cooperation with Nanostone Membranes, Oceanside, CA. The PNF2A membrane is positively charged over a wider pH range than typical NF

membranes. For comparison the negatively charged Nanostone NF3A membrane and recently developed NF4 membranes were used. All NF membranes were formed through the well-known interfacial polymerization process of an amine with an acyl chloride, but the exact composition cannot be disclosed. The membranes were tested in the spiral wound module configuration (0.59 m²). The use of membrane modules allowed for more stable comparison than flat sheet membranes, as the same module was used for various tests. The larger surface area mitigates the impact of any membrane defects and the enclosed module protects the membrane from damage. The commercial NF3A and NF4 membranes were brought in for comparison.

Feed solutions composed of pure salts and various salt mixtures were prepared for this study from ACS certified salts purchased from Fisher.

3.2.2 Experimental Apparatus and Methods

Tests of 0.59 m² spiral wound membrane modules were conducted using a unit consisting of two parallel PVC pressure vessels. The schematic for this unit can be seen in Figure 3.1. Feed solution was stored in a polypropylene tank and was delivered by a Procon stainless-steel pump (200 psi max pressure). In the tests, pressure was varied between 2-14 bar. A cooling coil was used to stabilize tank temperature which remained between 25-28 °C unless increased for high-temperature study in which temperatures were increased to 40 °C. Concentrate flow rate was held between around 11.4 L/m. During normal operation, both concentrate and permeate were recycled back into the feed tank. The system was allowed thirty minutes to reach steady state before data collection after a change in operation pressure. The system was cleaned between test runs, with DI water being permeated through the membrane at a pressure of approximately 3.5 bar for 30 minutes. After cleaning, the water was disposed of to prevent contamination.

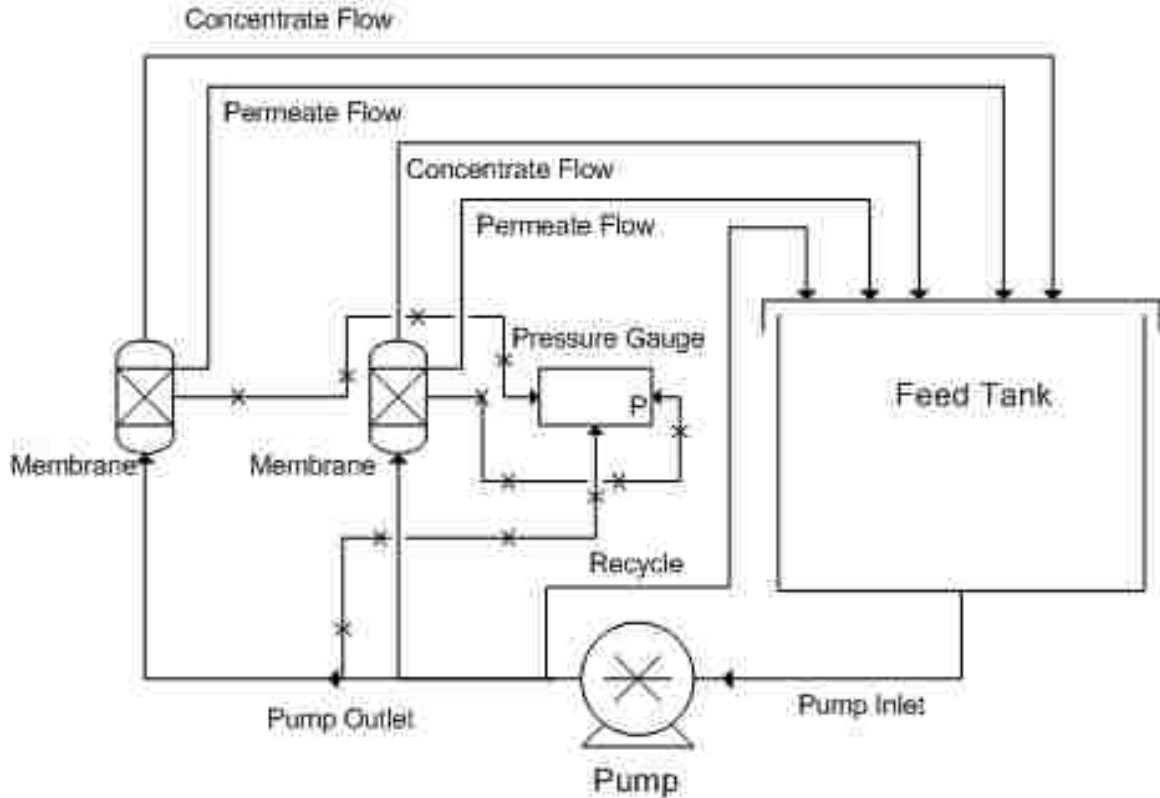


Figure 3.1 Membrane unit for the experimental testing of 2514 scale NF Membrane modules.

3.2.3 Sample Analysis

All conductivity analysis for feed solutions and permeates was measured using a Fisher Scientific conductivity probe with instrument error of 1%. Ca, Na, Mg, and Se concentration were measured through analysis with Inductively Coupled Plasma Optical Emission Spectrometry (ICP-OES Varian VISTA-PRO). Following conventional ICP protocol, yttrium chloride (1 mg/L) was used as a standard to account for variation in sample volumes. Samples were diluted with 1% nitric acid to aid in digestion of ions in solution. The wavelengths used for cation analysis were 318.127 nm (Ca), 285.213 nm (Mg), and 568.821 nm (Na). Calculated error for ICP-OES was determined to be 1% for Ca^{2+} , and 18% for Na^{+} .

3.2.4 Model for Ion Transport

The extended Nernst Planck equation has been applied to this system.

$$J_i = -K_d D_i \frac{dC_i}{dx} - \frac{Z_i C_i D_i F}{RT} \frac{d\varphi}{dx} + K_{ic} C_i J_v \quad (3.1)$$

J_i is the transport of ionic species through the membrane. The first term in the Equation 3.1 accounts for the diffusive transport through the membranes, where K_d is the hindered coefficient for diffusion of solute through the membrane. The second term in the equation corresponds to electrically The third term in the equation represents the convective transport of ions through the membrane, in which, K_c is the coupling coefficient. K_d and K_c are dependent on the ratio of solute radius to effective pore size (λ_i) of the membrane and can be estimated by (1.2 and Equation 3.3 [17].

$$K_{id} = 1.0 - 2.30\lambda_i + 1.154\lambda_i^2 + 0.224\lambda_i^3 \quad (1.2)$$

$$K_{ic} = 1.0 + 0.054\lambda_i - 0.988\lambda_i^2 + 0.441\lambda_i^3 \quad (3.3)$$

Where, $\lambda_i = r_i / r_p$ (solute radius/pore radius).

In order to determine r_p of the membrane the modified Nernst Planck equation was simplified for transport of uncharged solutes by removing the electrically driven transport term as seen in Equation 3.4.

$$J_i = -K_d D_i \frac{dC_i}{dx} + K_{ic} C_i J_v \quad (3.4)$$

There is no net current flowing through the membrane, i.e. no net flux of charge across the membranes. F_i account for the transport of cationic species through charged polyamide membranes the potential gradient term must be determined(second term in Equation 3.1. It can be estimated by Equation 3.5, which

is derived from $+K_i C_i J_v$ after using the condition of no net flux of charge through the membrane.

$$\frac{d\phi}{dx} = \frac{\sum_{i=1}^n \frac{z_i J_v}{K_{id} D_{i\infty}} (K_{ic} C_i - C_{i_permeate})}{\frac{F}{RT} \sum_{i=1}^n z_i^2 C_i} \quad (3.5)$$

The membrane was assumed to have a fixed charge density, X_d , across its entire thickness and it was assumed that charge must be balanced both at the feed and the permeate of the membrane.

$$\sum_{i=1}^n z_i C_i + X_d = 0 \quad (3.6)$$

Steric partitioning was also accounted for in the model and partitioning coefficient of various ions at membrane was calculated using Equation 3.7.

$$\phi = (1 - \lambda_i)^2 \dots \quad (3.7)$$

Concentration of the ions in permeate was calculated by Equation 3.8.

$$C_p = J_i / J_v \quad (3.8)$$

Influence of concentration polarization was assumed to be minimal for these studies, as tangential flow through the spiral wound modules was over 2.5 gallons per minute. Per pass recovery of water through the membranes was found to be ~1%, so ion concentration in the feed solution is assumed to be uniform as tangential convective mass transport dominates mass transfer through the membrane. Sherwood number was thus assumed to be high enough to neglect concentration polarization effects.

The model was utilized in conjunction with several sets of single salt rejection data for multiple ion of varying valency The X_d term was optimized to simultaneously

fit 4 sets of single salt rejection. It was assumed that X_d change for the experimental sets was largely a property of the membrane, and the concentration of solute was too low to have major impact on the X_a value outright. These assumptions were suitable to demonstrate that the data could be reasonably fit, thus the transport fundamentals in the Nernst Planck equation hold true in this scenario. Furthermore differences between ions that contribute to changes in rejection could be analyzed.

3.3 Results and Discussion

3.3.1 Characterization of PNF2A Membrane Surface

The Nanostone PNF2A membrane tested in these studies has unique surface properties and performance due to the addition of mixed amines during interfacial polymerization. Thus, the surface properties have been studied in order to better understand how the surface chemistry differs from commercial membranes. The surface composition of a flat sheet of PNF2A was characterized using X-ray photoelectric spectroscopy (Thermo Scientific K-Alpha) with Al/K ($h\nu=2000\text{eV}$) anode mono X-ray source. The results of a surface scan on PNF2A alongside NF3A, a commercial negatively charged polyamide NF membrane also produced by Nanostone, in addition to PS35, a polysulfone ultrafiltration membrane used as a support in NF casting are shown in Figure 3.2. The C1s, N1s, O1s, peaks were present at 285, 532, 399 eV respectively. It can clearly be seen that the intensity of the nitrogen peak in both of the NF membrane is much greater than the surface of the polysulfone backing (PS35). It can also be seen that the S2s and S2p3 peaks are not visible in the NF3A or PNF2A samples thus the backing is not being expressed through the NF surface. The elemental ratios were determined by peak area and compared to literature results for NF 270, a commercial membrane produced by DOW FILMTEC, in

Table 3.1⁶⁵. As indicated by the C:O:N ratio, PNF2A has a greater percentage of N than the NF-270 which results from the mixed amines added to the piperazine solution in the casting of the membrane.

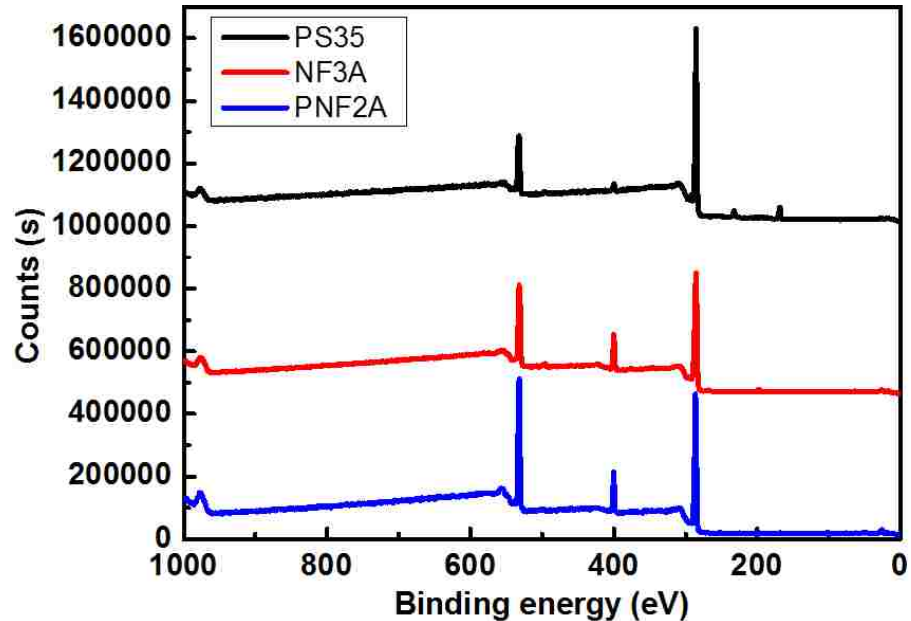


Figure 3.2. XPS survey scan of PS35, NF3A, and PNF2A membranes.

Table 3.1: XPS surface characterization for O, N, and C performed for PNF2A membrane compared to literature values for DOW NF-270 membrane.

PNF2A-Experimental Data			DOW NF 270 [19]	
Peak	Peak BE (eV)	Atomic %	Peak	Atomic %
O1s	532.21	24.36	O1s	22.3
N1s	400.16	10.27	N1s	7.5
C1s	286.03	65.37	C1s	64.4
C:O:N Ratio		6.4:2.4:1	C:O:N Ratio	
			8.6: 3.0:1.0	

Zeta potential analysis was performed with the Anton-Paar Surpass Electrokinetic Analyzer to characterize membrane surface charge of the Nanostone PNF2A. This data is compared to literature data for the Dow NF-270 membrane published by Tannien et al⁶⁶. The resulting data can be seen in Figure 3.3. Two pKa shifts, one at pH 4 and one at pH 8 in the PNF2A membrane indicate the presence of both acidic and basic groups which in

this case are both carboxyl and amine groups. The PNF2A membrane is shown to maintain a higher surface charge than the DOW NF-270 membrane over the pH range, due to the presence of primary amine groups. It must be stated that above pH 5 the PNF2A membrane is negatively charged. As a result, the comparing ion transport behavior regarding counter ion and co-ion properties should be comparable between membranes.

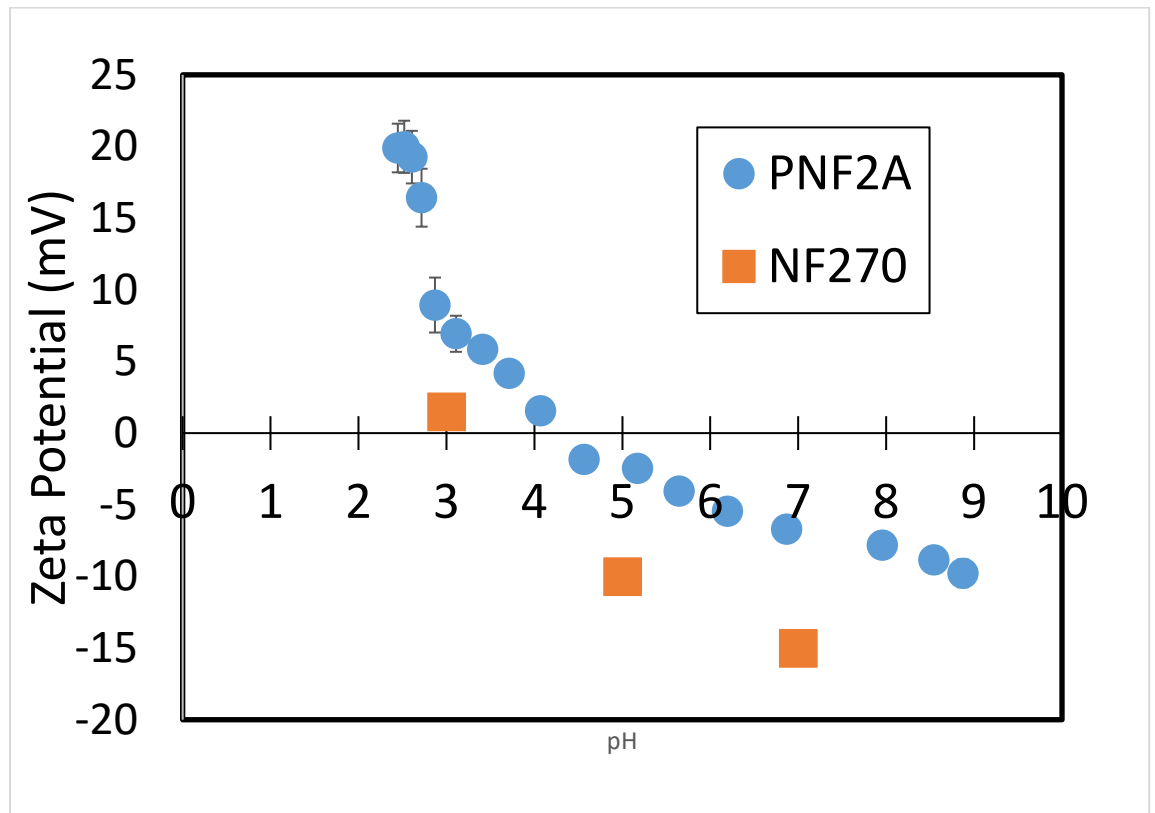


Figure 3.3 Zeta Potential of the Nanostone PNF2A and DOW NF-270 membranes vs. pH.

3.3.2 Ion Rejection in Synthetic Single Salt Solutions.

The water permeability and rejection characteristics of single salt solutions (Na_2SO_4 , CaCl_2 , MgSO_4 , NaCl) are presented for PNF2A. Table 3 lists these values with data for commercial membranes from literature^{66, 67}. Experimental results for NF3A and NF4, commercial negatively charged membranes also produced by Nanostone, have also been included for reference. Water permeability and single salt rejection of PNF2A are comparable to that of the commercial NF membranes. Concentrations were chosen to maintain charge equivalency of differing ions in later mixed salt experiments. At the concentrations chosen for synthetic salt solutions, the meq/L values are nearly equal to each other, 34.2 meq/L Na^+ compared to 36 meq/L Ca^{2+} and 34.2 meq/L Cl^- compared to 28.2 meq/L SO_4^{2-} (a 20% difference). PNF2A ion rejection for single salts was found to increase in the manner of $\text{NaCl} < \text{Na}_2\text{SO}_4 < \text{CaCl}_2 < \text{Mg}_2\text{SO}_4$. This corresponds to the combined influence of Donnan and dielectric forces in the rejection of ions. Higher rejection of divalent cations over divalent anions is explained by the larger hydrated ionic radius of Ca^{2+} (0.42 nm) and Mg^{2+} (0.44 nm) to SO_4^{2-} (0.392 nm).^{56, 68}

Table 3.2: Water Permeability and Single Salt rejection performance of selected commercial membranes and PNF2A. Operating pressure for NF3A, PNF2A, and NF4 was 10.3 bar. Feed pH 5-6.

NF Membrane	Manufacturer	Contact Angle ($^{\circ}$) ^{66,67} 676059585857	Water Permeability (LMH/bar)	Na ₂ SO ₄ Rejection (%) {Conc.}	CaCl ₂ Rejection (%) {Conc.}	MgSO ₄ Rejection (%) {Conc.}	NaCl Rejection (%) {Conc.}
NF270	Dow Filmtec	30 ± 2	8.5 ⁶⁶	96 ⁶⁶	63 ⁶⁶	99 ⁶⁷	59 ⁶⁶
NF90	Dow Filmtec	54	5.2 ⁶⁶	95 ⁶⁶	98.8 ⁶⁶	---	92 ⁶⁶
Desal-5 DK	SUEZ	74 ± 2	3.3 ⁶⁷	-----	---	96	80
NF3A	Nanostone	22.3 ± 2.5	5.5	99.5 {14.1 mM feed}	95.9 {18 mM feed}	99.1 {16.1 mM feed}	---
PNF2A	Nanostone	17.7 ± 1.8	5.1	82.6 {14.1 mM feed}	92.3 {18 mM feed}	95 {16.1 mM feed}	43.6 {34.2 mM feed}
NF4	Nanostone	---	8.5	---	98.3 {18 mM feed}	---	46.2 {34.2 mM feed}

The extended Nernst Planck equation with steric partitioning model was used to fit flux dependent rejection of several single salt solutions (Figure). Charge Density of the

membrane could be fit to accurately predict rejection of most salt solutions. CaCl_2 rejection is underestimated by the current model. This is likely due to dielectric exclusion effects that have not been incorporated into the current model.

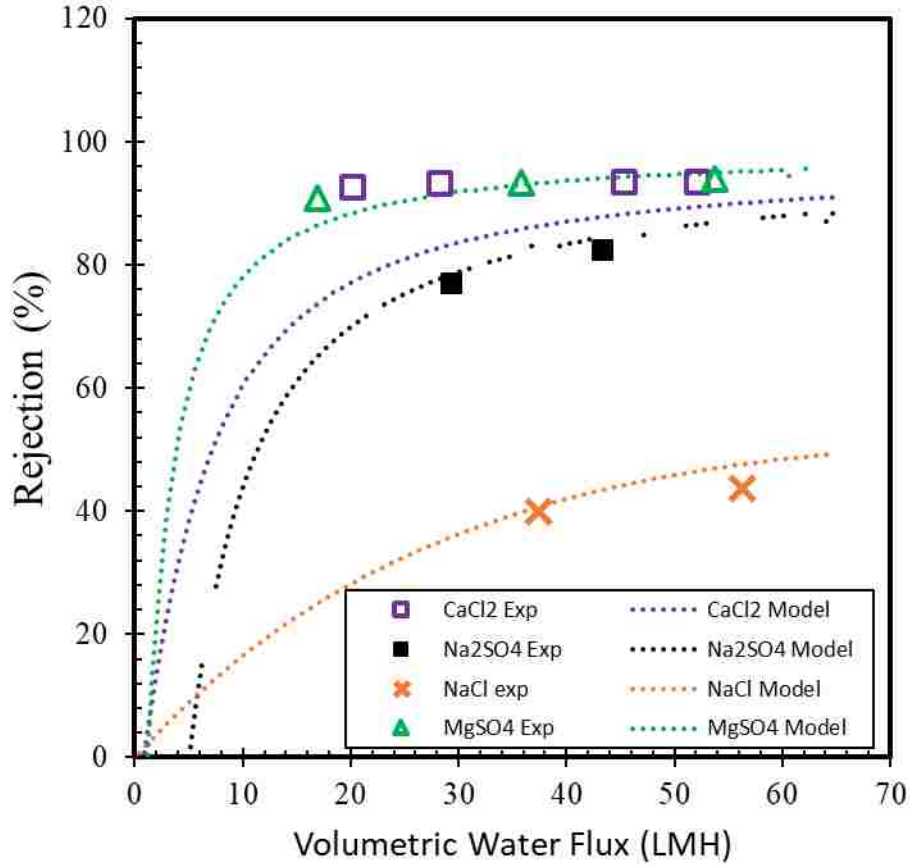


Figure 3.4. Ion rejection for mixed salt solutions as determined experimentally and by optimization of the extended Nernst Planck model. All salt solutions 2000 mg/L. pH=5.9.

3.3.3 Ion Rejection in Synthetic Mixed-Salt Solutions

A goal in this work was to study the rejection characteristic of mixed-salt solutions containing either multiple cations or multiple anions. Two synthetic mixed-salt solutions were created, 18 mM CaCl_2 /34.2 mM NaCl (Figure 3.5) and 14.1 mM Na_2SO_4 /34.2 mM NaCl . (Figure 3.6). In tests of both solutions it was evident that the rejection of the divalent ion was not significantly reduced in the presence of added monovalent salt. Monovalent

salt rejection was reduced roughly 10%. These results suggest that at similar concentrations charge shielding does not inhibit rejection of divalent ions due to combined Donnan and dielectric exclusion forces. This is consistent with current literature. In experimental data published by Deon et al. , a 1:2 ratio of $MgCl_2$ to $NaCl$ the Mg^{2+} rejection did not decrease from that of a similar concentration of solution of $MgCl_2$ ⁶³. The synthetic salt solution experiments were limited to similar concentrations of salt. Excess concentrations of monovalent salt are predicted to reduce the rejection of the divalent ion, as it is well established that significantly increasing ionic strength reduces effective surface charge through shielding⁶⁹. The greater magnitude of positive charge of Ca^{2+} interacts more closely with the membrane surface than Na^+ . This interaction helps to shield the Cl^- from the charge of the membrane surface, reducing Donnan exclusion. Na^+ has a smaller hydrated radius than Ca^{2+} , and thus will transport through the pores more easily when charge is shielded.

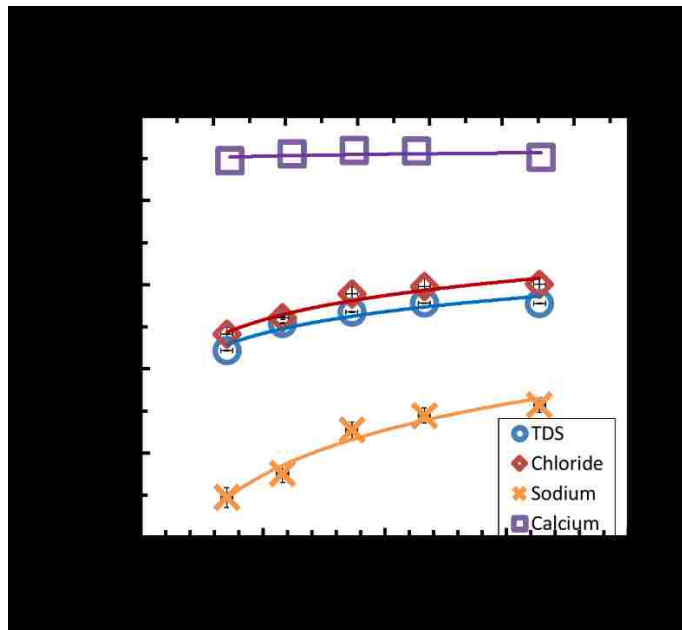


Figure 3.5. PNF2A water flux and rejection data for 18 mM $CaCl_2$ / 34.2 mM $NaCl$ mixed salt solution. Operating temperature was 27°C. Feed pH was 5.9. Retentate flowrate was maintained at 10.1 L/min. Line denotes predicted trend.

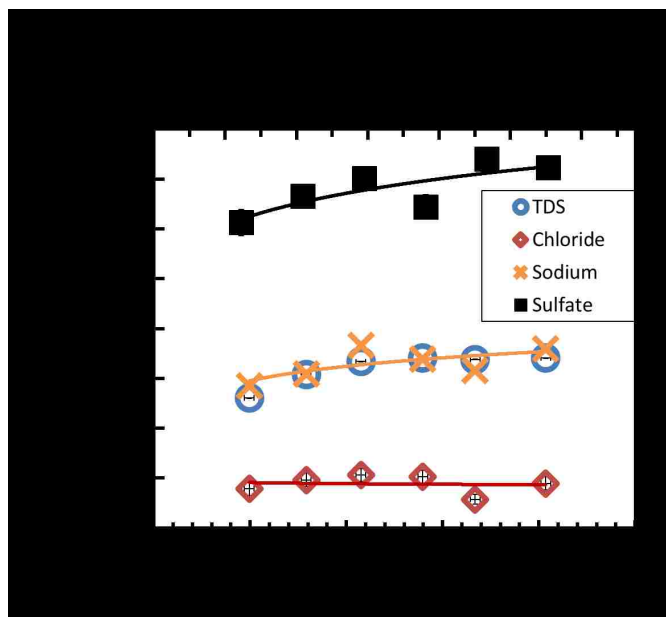


Figure 3.6. PNF2A Water flux and rejection data for 14.1 mM Na₂SO₄ / 34.2 mM NaCl mixed salt solution. Operating temperature was 27°C. Feed pH was 5.9. Retentate flowrate was maintained at 10.1 L/min. Line denotes predicted trend.

Similar results are also seen in Garcia-Aleman et al. in regards to how increasing Mg²⁺ increases Na⁺ transport across the membrane⁷⁰. The paper goes on to show Cl⁻ transport is also reduced in the presence of SO₄²⁻.

3.3.4 Ion rejection as a function of ionic strength

The effects of ionic strength on ion rejection are very significant in understanding transport and interactions for mixed salt solutions. This is particularly relevant as several industrial applications for NF membranes involve concentrations exceeding 10,000 mg/L TDS. To gain a better understanding of the effective of ionic strength and interaction of multiple salts, PNF2A rejection of Ca²⁺ and Na⁺ was studied as NaCl was progressively added to an 18mM CaCl₂ solution. Figure 3.7 shows the Ca²⁺ and Na⁺ rejection normalized over the pure CaCl₂ and NaCl rejection shown in Table 3.2. The presence of CaCl₂ corresponds to a reduced Na⁺ rejection when compared to the pure NaCl rejection at the same concentration. The initial added concentration of 34.2 mM NaCl however results in

only 3% loss in Ca^{2+} rejection compared to the single salt rejection. It can be reasoned that in the case of similar equivalencies, the screening effects of the divalent ion have significant implication for Donnan exclusion of the monovalent ion, while the monovalent ion has negligible influence with how the divalent ion interacts with the membrane. Further increase in ionic strength led to the substantial rejection loss for Na^+ compared to Ca^{2+} . Charge shielding as ionic strength increases inhibits Donnan exclusion. Thus, the effect of charge repulsion due to charge shielding appears less severe with divalent ions than monovalent ions. The trend in rejection loss seems to level off beyond 200mM NaCl. This concentration corresponds to the concentration beyond which membrane charge becomes constant, according to studies on membrane surface charge at high ionic strengths ⁷¹. Increased rejection of divalent ions at high ionic strength results from their larger hydrated ionic radius over monovalent ions as well as a larger potential for dielectric exclusion due to the magnitude of their charge. High selectivity becomes possible as charge repulsion remains significant enough to reject divalent ions, but monovalent ions can transport through the membrane.

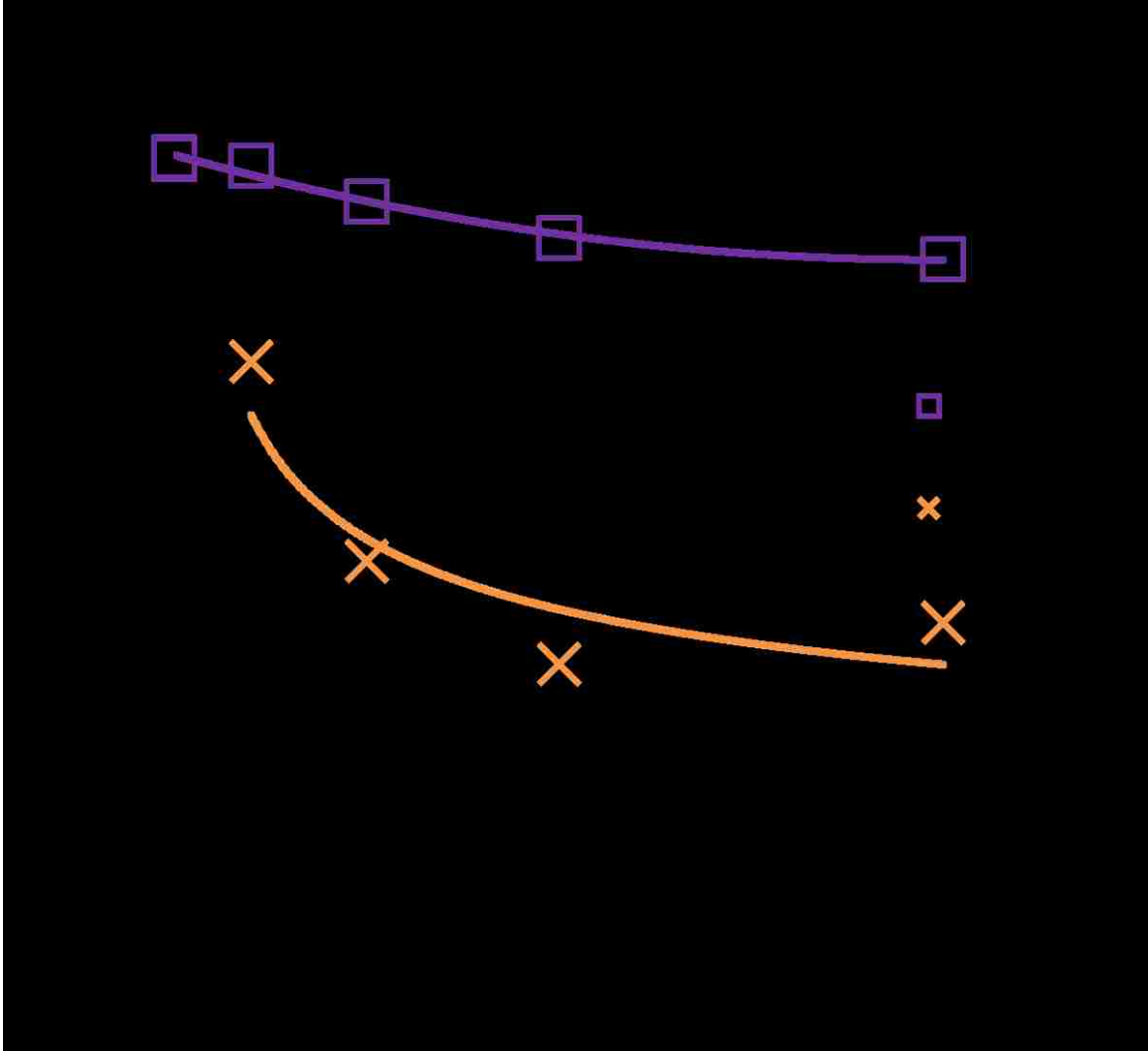


Figure 3.7: Rejection of Ca²⁺ and Na⁺ normalized using the single salt rejection in Table 1 vs. NaCl concentration as NaCl was progressively added into the mixed salt feed. Initial feed concentration is equal to 18 mM CaCl₂. Temperature = 28-30 degrees C. Retentate flowrate = 10.1 L/min. Feed pH = 6.

CHAPTER 4. NANOFILTRATION FOR INDUSTRIAL WASTEWATER TREATMENT

4.1 Introduction

Membrane processes have found extensive use in wastewater treatment and desalination in various industries such as textiles⁷², dairy⁷³, and pharmaceuticals⁷⁴. Treatment of wastewater containing high concentrations of dissolved solids (TDS) requires selective separations due to osmotic pressure issues. Charged nanofiltration (NF) membranes have found extensive use in the desalination of produced water in the oil and gas industry due to the capability for selective separations and lower energy costs than reverse osmosis (RO) membranes^{75,76}.

This work aims to test the effectiveness of desalination of scrubber wastewater at water recoveries exceeding 75%. Challenges of osmotic pressure increase during water recovery through NF desalination. This work also studies onset of gypsum ($\text{CaSO}_4 \cdot 2\text{H}_2\text{O}$) precipitation during water recovery, including the effect of counter ions such as Cl^- on gypsum solubility. This research expands on previous work in desalination of multicomponent feeds by incorporating the large-scale membrane modules in experiments with a variety of synthetic feed solutions and water recovery of actual scrubber water with limitedly soluble ions in solution.

4.2 Experimental

4.2.1 Commercial NF Membranes

The PNF2A membrane studied was a charged polyamide thin film composite membrane developed in cooperation with Nanostone Membranes, Oceanside, CA. The PNF2A membrane is positively charged over a wider pH range than typical NF

membranes. For comparison the negatively charged Nanostone NF3A membrane and recently developed NF4 membranes were used. All NF membranes were formed through the well-known interfacial polymerization process of an amine with an acyl chloride, but the exact composition cannot be disclosed. The membranes were tested in the spiral wound module configuration (0.59 m²). The use of membrane modules allowed for more stable comparison than flat sheet membranes, as the same module was used for various tests. The larger surface area mitigates the impact of any membrane defects and the enclosed module protects the membrane from damage. The commercial NF3A and NF4 membranes were brought in for comparison.

4.2.2 Plant Bowen Flue Gas Desulfurization Wastewater

Actual scrubber water (composition given in Table 4.1) received from Georgia Power Plant Bowen was also tested. The water contains high concentrations of Ca²⁺, Mg²⁺, Cl⁻, and SO₄²⁻ mostly divalent cations and a mixture of divalent and monovalent anions, along with some additional metals. The presence of Ca²⁺ ions from the limestone slurry and SO₄²⁻ ions from the removal of SO₂ from power plant flue gas is notable due to the potential of precipitation of CaSO₄ solid. The received water was slightly below saturation concentrations as no particulates were observed suspended in the water.

Table 4.1: Concentration of various ions and trace metals in scrubber wastewater received from Plant Bowen, GA. Water pH= 4.5. Trace metal concentrations determined by inductively coupled plasma dynamic reaction cell mass spectrometry (ICP-DRC-MS) by Applied Speciation and Consulting LLC.

Ion/Element	Concentration (mg/L)
Ca ²⁺	3184
Mg ²⁺	660
Na ⁺	100
Cl ⁻	6656
SO4 ²⁻	1169
Se	0.61
As	0.005
Ni	0.39
Cd	0.06
Mn	5.79
Zn	1.92

4.2.3 High TDS Produced Water

Produced water samples were provided by Chevron as seen in Table 4.2. Notably this water has high TDS (conductivity exceeding 6.24 mS/cm) largely made up of sodium and chloride ions. Higher valency ions as well as nonmetallic ions were present within the wastewater. Naphthenic acid was also present in the produced water (34 mg/L) and was the major target solute for removal in this study.

Table 4.2. Inorganic and organic analysis of produced water samples.

	mg/L
Br-	130
Cl-	130000
F-	0
NO ₃ -	0
NO ₂ -	0
Sulfate	20
NH ₃ as N	60
HCO ₃ - (as CaCO ₃)	182
CO ₃ -- (as CaCO ₃)	0
Total alkalinity (as CaCO ₃)	182
Ba	42
Ca	3500
Fe	46
Mg	1200
K	300
Na	61000
Silica	44
pH	6.06
Spec. Conduct (uS/cm)	624000
SG	1.13
TDS	220000
TOC	270
TSS	133

4.2.4 Nanofiltration apparatus and methods.

Tests of 0.59 m² spiral wound membrane modules were conducted using a unit consisting of two parallel PVC pressure vessels. The schematic for this unit can be seen in Figure 4.1. Feed solution was stored in a polypropylene tank and was delivered by a Procon stainless-steel pump (200 psi max pressure). In the tests, pressure was varied between 2-14 bar. A cooling coil was used to stabilize tank temperature which remained between 25-28 °C

unless increased for high-temperature study in which temperatures were increased to 40 °C. Concentrate flow rate was held between around 11.4 L/m. During normal operation, both concentrate and permeate were recycled back into the feed tank. The system was allowed thirty minutes to reach steady state before data collection after a change in operation pressure. The system was cleaned between test runs, with DI water being permeated through the membrane at a pressure of approximately 3.5 bar for 30 minutes. After cleaning, the water was disposed of to prevent contamination. After recovery runs, the membrane was cleaned with DI water in a similar fashion to avoid scaling caused by stagnation of water in the membrane. During water recovery testing, the system is operated in feed and bleed mode, meaning permeate was collected in a separate container, while the concentrate was recycled back into the feed tank.

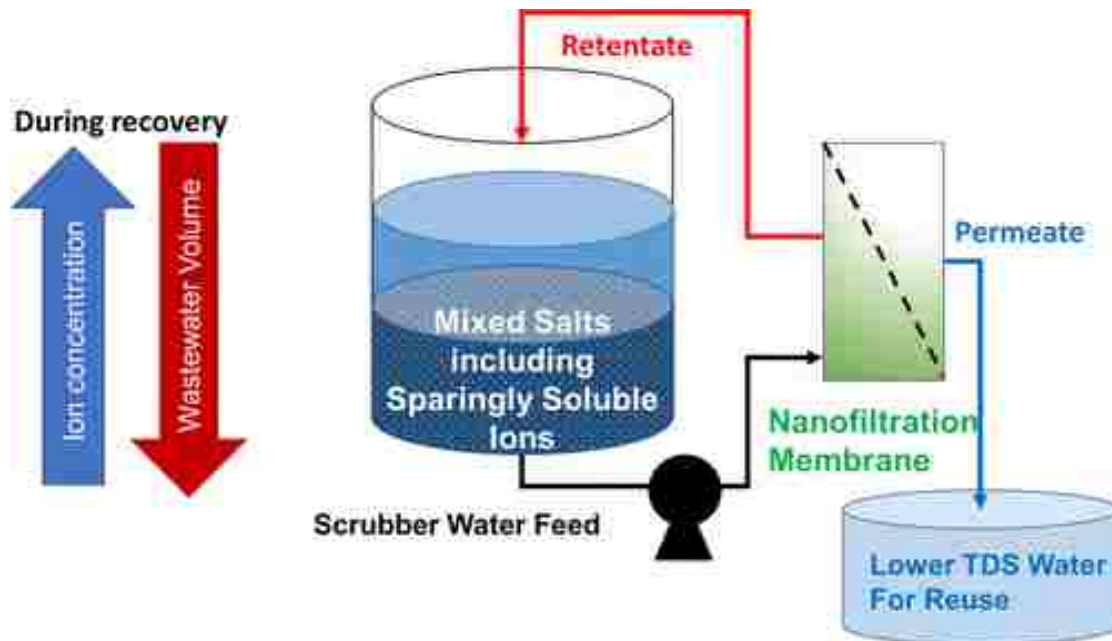


Figure 4.1. Nanofiltration apparatus for industrial wastewater recovery.

4.2.5 Analysis of Samples

All conductivity analysis for feed solutions and permeates was measured using a Fisher Scientific conductivity probe with instrument error of 1%. Ca, Na, Mg, and Se concentration were measured through analysis with Inductively Coupled Plasma Optical Emission Spectrometry (ICP-OES Varian VISTA-PRO). Following conventional ICP protocol, yttrium chloride (1 mg/L) was used as a standard to account for variation in sample volumes. Samples were diluted with 1% nitric acid to aid in digestion of ions in solution. The wavelengths used for cation analysis were 318.127 nm (Ca), 285.213 nm (Mg), and 568.821 nm (Na). Calculated error for ICP-OES was determined to be 1% for Ca^{2+} , 7% for Mg^{2+} , and 18% for Na^+ . Concentrations of Se exceeding 50 $\mu\text{g/L}$ were analyzed at a wavelength of 196.026 nm. For samples containing less than 50 $\mu\text{g/L}$ Se, graphite furnace atomic absorption spectrometer (GFAAS, Varian 880Z) was used. Samples were digested at 110 °C for 2 h. Selenium standards for analysis of selenium were prepared with similar concentrations of dissolved solids (accounting for dilution) to best match the matrix to the scrubber water samples. Concentrations of Cl^- , SO_4^{2-} were analyzed by DIONEX IC25 ion chromatograph (column: IonPac AS18 4x250 mm) with $\text{Na}_2\text{CO}_3/\text{NaHCO}_3$ buffer solution as mobile phase (1 mL/min, 2000 psi). Cl^- and SO_4^{2-} errors were determined to be 3.9% and 6.8% respectively.

Samples for scrubber water treated by NF and iron nanoparticle functionalized tab analysis was performed by ion chromatography inductively coupled plasma collision reaction cell mass spectrometry (IC-ICP-CRC-MS). Total elemental analyses for Se, As, Ni, Cd, Mn, and Zn were performed via inductively coupled plasma dynamic reaction cell mass spectrometry (ICP-DRC-MS).

4.2.6 Naphthenic acid (NA) separation by nanofiltration (NF):

High TDS produced water from oil sands tailings was provided by Chevron. The summary of the inorganic and organic composition of this water can be seen in Table 4.3. Among the TOC present are naphthenic acid in produced water is roughly 34 mg/L. Synthetic solutions were also used to study naphthenic acid removal in different ion conditions.

Table 4.3: Summary of organic and inorganic contents of oil sands produced water used in the study

pH	5.5-6
TOC (mg/L)	150
TDS (mg/L)	210,000
TSS (mg/L)	25.8
CO ³⁻ (mg/L)	182
Cl ⁻ (mg/L)	110,000
SO ₄ ²⁻ (mg/L)	80
Na (mg/L)	64000
Ca (mg/L)	5000
Fe (mg/L)	58
Mg (mg/L)	2400

NA separations by NF membrane were studied in Sterlitech filtration cell operated in dead-end mode. Two commercial membranes, DOW FLIMTEC NF270 and Nanostone Water Co. NF8, were used for the study. Before every experimental run, the membranes were rinsed with DIUF water and were tested for defects by measuring salt rejection using a magnesium sulfate standard.

Where, C_{per} and C_{feed} are the permeate and feed concentration of the species. Pressure normalized water flux (permeability) of the membranes was determined before and after the experiments with produced water samples. The flux was measured, by recording the mass of the permeate through the RS232 output of the balance at a sampling rate of 50 sec⁻¹. Produced water flux by NF membranes was monitored for 20 h in cross-flow setup. 10 L of feed produced water was used, and 10 ml of the permeate (0.1% recovery) was taken out for analysis during each sampling (10 samples over the course of the experiment). Produced water flux was also monitored with increasing recovery (up to 80 %) in dead-end mode filtration cell.

4.3 Results and Discussion

Ion rejection phenomenon were studied for scrubber wastewater from Plant Bowen, GA and high TDS oil sands produced water. Selective rejection preferential to divalent ions was observed in PNF2A operation in industrial wastewater water. The addition of similar concentrations of monovalent salt had minimal effects on the rejection of divalent ions, while the rejection of the ions making up the monovalent salt was reduced, becoming negligible at higher concentrations. The flux and rejection of ions were studied for up to 80% water recovery of the scrubber wastewater, at which point over 60% TDS rejection was observed in the overall permeate. Gypsum formation was also studied during recovery.

High recovery (~80%) of produced water was also achieved while removing naphthenic acid pollutants from solution.

4.3.1 Partial Desalination of High TDS Scrubber Wastewater

Unlike the high-TDS synthetic water feed solution, the scrubber water received from Plant Bowen, GA had a relatively low concentration of Na^+ (4.3 mM), while containing high concentrations of Ca^{2+} (~80 mM), Mg^{2+} (27.2 mM), Cl^- (~186.2 mM), and SO_4^{2-} (~12.1 mM). The overall TDS of the scrubber wastewater is 12,000 mg/L. As this water is largely composed of divalent ions, reduction of TDS through nanofiltration is hypothesized to be successful. Rejection of major ion components can be seen in Figure 4.2. The membrane rejected over 90% of all major ion species in the scrubber water with the exception of monovalent sodium. A flux 32.2 LMH was maintained during operation.

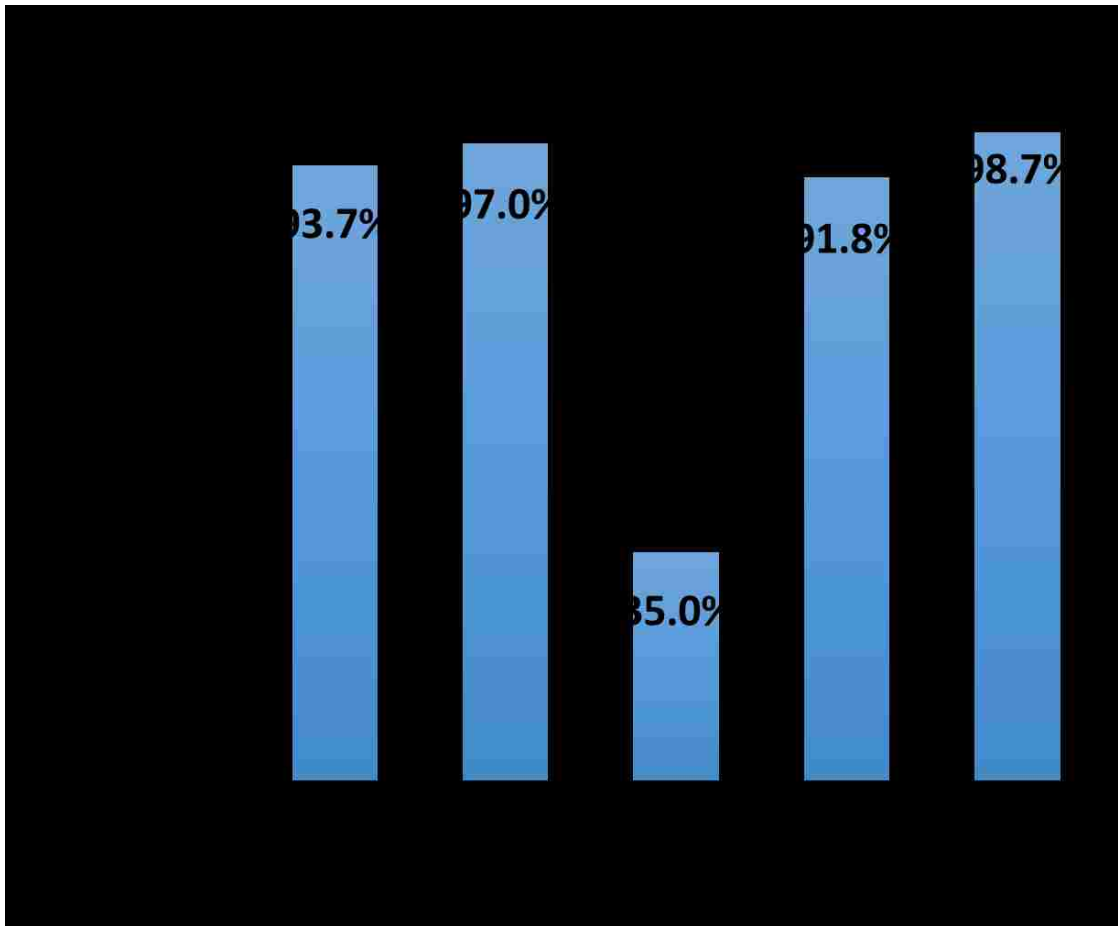


Figure 4.2: PNF2A ion rejection for Plant Bowen scrubber wastewater. Experiment performed at 25°C. Operating pressure was held at 13.45 bar. Water flux was observed to be 32.2 LM. Feed pH = 4.5.

4.3.2 High Water Recovery of Scrubber Wastewater

A single pass of scrubber wastewater through the NF membranes results in roughly 5% water recovery when concentrate flow rate is maintained at 3 GPM. Scrubber water feed was recirculated through the membrane while permeate was collected in a container to obtain high water recovery in a feed and bleed mode. Concentration polarization and surface scaling during feed and bleed operation is significantly reduced compared to operating at a high recovery during a single pass. Figure 4.3 shows the volumetric flux of the PNF2A, NF3A, and NF4 membranes. The decrease in volumetric flux corresponding to increasing water recovery is related to the increase in osmotic pressure of the feed solution with recovery. A higher water recovery could easily be obtained by operating at a higher pressure.

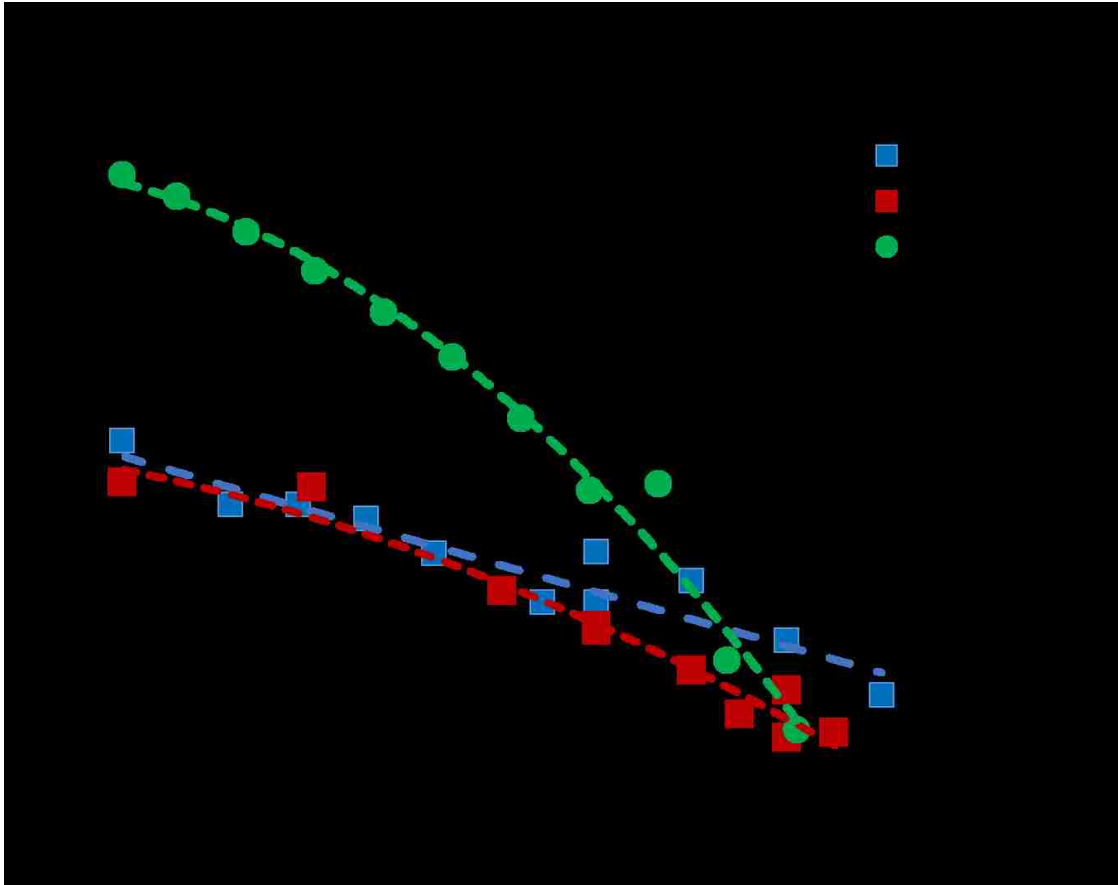


Figure 4.3: Water flux throughout high recovery operation of the PNF2A, NF3A, and NF4 membranes. Operating pressure maintained at 13.8 bar. Retentate flowrate maintained at 11.4 L/min. Tank temperature varied from 20-27°C. Feed pH= 4.5.

Table 4.4 shows the concentration of ions in the feed, PNF2A overall permeate, and retentate after 80% water recovery was achieved in feed and bleed operation. The selectivity of the membranes for ion removal were quantified by the overall rejection of ions, determined by comparing the concentration of the *total* permeate to the initial feed. This method of quantifying rejection is most practical to the intended application of recovering water suitable for reuse in process while reducing the volume of wastewater. Charge shielding from the increasing ion concentration at the boundary layer will reduce single pass rejection during the duration of water recovery. Even if this were not the case

and rejection were to remain constant, at overall rejection would still decrease over the course of water recovery. At 90% water recovery, 90% rejection of a particular ion would result in permeate that is close to the quality of the initial feed. Overall rejection of Ca^{2+} and Mg^{2+} were just over 60% and 76% respectively. Overall Cl^- rejection was observed to correlate Ca^{2+} rejection as expected due to Ca^{2+} and Cl^- composing the major cation/anion pair in solution. SO_4^{2-} rejection after 80% water recovery was observed to remain at over 93% due to the formation of gypsum at higher water recovery preventing the increase of SO_4^{2-} concentration during water recovery.

Table 4.4: Feed, retentate, and overall permeate analysis for high water recovery operation of PNF2A membrane module.

	Ca ²⁺ (mg/L)	Mg ²⁺ (mg/L)	Na ⁺ (mg/L)	Cl ⁻ (mg/L)	SO ₄ ²⁻ (mg/L)	NO ₃ ⁻ as N (mg/L)	Se (µg/L)	TSS (mg/L)
FGD Process Water Feed	2894	660	214	6585	1262	16	750	0
PNF2A Retentate 80% Water Recovery	6307	1907	215	15839	1614	26	1570	1398
PNF2A Overall Permeate	1140	157	75	2480	47	4	120	0
PNF2A Overall Rejection (%)	60.6%	76.2%	64.9%	62.3%	93.5%	71.6%	84.2%	---

NF membranes have the capability of achieving higher water recovery at lower operating pressures than RO membrane due to their selective rejection properties. As water recovery increases, rejection in an NF membrane decreases. RO membranes show relatively constant rejection vs water recovery, as size exclusion is the primary factor in rejection. At 80% water recovery the retentate concentration can be as high as 5 times that

of the feed concentration, leading the osmotic pressure to increase nearly 5 times in RO membranes. However, in the case of an NF membrane, the rejection is far below 99%, so only a fraction of the osmotic pressure difference of RO operation is encountered. PNF2A rejection decreases more substantially during water recovery than either NF3A and NF4 allowing for greater water flux at high recovery.

4.3.3 Gypsum formation

The scrubber wastewater contains high concentrations of Ca^{2+} and SO_4^{2-} , thus at high water recovery the precipitation of gypsum occurs as the solution reaches saturation. Gypsum fouling on the membrane surface and between feed spacers is well known to be a cause of reduced volumetric flux. It is desirable to know the point in water recovery that gypsum precipitation will begin in addition to the number of particles formed after recovery is complete. Gypsum that precipitates does not contribute to osmotic pressure differences across the membrane. Thus, the true effect of precipitation of gypsum on flux during water recovery is a combination of reduced osmotic pressure and fouling aspects. Gypsum precipitation, if controlled by a seed crystals or other methods, may also be utilized to reduce the retentate concentration and lower osmotic pressure effect during high water recovery operation⁷⁷.

Calcium sulfate dihydrate has been shown to only be soluble up to 0.015 molal at the temperature range between 20-40°C⁷⁸. The Handbook of Chemistry and Physics value for K_{sp} of Calcium Sulfate dihydrate is 3.14×10^{-5} at 25°C⁷⁹. However the presence of Mg^{2+} and Na^+ , both present in significant concentration in scrubber water, is expected to delay precipitation as soluble complexes compete with gypsum⁸⁰. Similar solubility increases are hypothesized with the significant concentration of Cl^- anions in solution.

Concentrations of Ca^{2+} and SO_4^{2-} were 0.158 M (6300 mg/L) and 0.017 M (1600 mg/L) in the final retentate respectively. The ionic strength of the scrubber water is expected to increase the solubility of calcium sulfate dihydrate somewhat as would the slight increase of temperature during operation. The experimental ionic strength at 50% water recovery, I , was calculated to be 0.12 M. Therefore, significant interaction between Ca^{2+} and Cl^- ions as well as Mg^{2+} and SO_4^{2-} ions must be occurring.

Experimental data for 80% water recovery for PNF2A operation suggests that the total suspended solid concentration was around 1400 mg/L in the retentate. This TSS concentration is a little over 5% the concentration of the retentate TDS. Magnesium, a non-precipitating divalent cation, tripled in concentration between feed and retentate after 80% of the water was recovered in during PNF2A tests. Comparatively the concentration species involved in the precipitation of gypsum, Ca^{2+} and SO_4^{2-} , increased by 2.2 and 1.3 times respectively during the same test. The maximum amount of gypsum that could theoretically be present before water recovery is 1800 mg/L. Therefore at 80% water recovery one would expect the maximum possible TSS value to be 9000 mg/L, far greater than the actual measured value. It is possible some CaSO_4 could be present as a scale layer on the membrane surface, but flux behavior during recovery doesn't indicate scale formation is significant. Thus, the presence of Cl^- and Mg^{2+} are believed to result in the reduced occurrence of dissolved solids unless there is significant presence of small particles that bypassed filtering during TSS collection.

As suggested by Mi and Elimelech, Ca^{2+} attraction to the surface of a negatively charged NF membrane may yield a higher concentration of Ca^{2+} at the surface, initiating the formation of gypsum pre-nucleation clusters⁸¹. Thus, it may be possible to reduce

fouling by inhibiting the formation of pre-nucleation clusters on the membrane surface by implementing a membrane with positive charge. If this were to be the case, fouling could still result to gypsum particles to agglomerate and stick to the membrane surface after formation. At the current degree of gypsum formation during water recovery, no significant fouling was observed. The particulates did not appear to adhere to the membrane surface, instead being carried by the convective cross-flow. Further experiments must be done to determine if indeed gypsum particle formation can be inhibited at the membrane surface and the magnitude fouling is reduced when particles are formed in bulk solution compared to the membrane surface.

4.3.4 Retentate and Overall Permeate Concentration During Water Recovery

The concentration of retentate and permeate during water recovery is shown in Figure 4.4 and Figure 4.5 respectively. Na^+ has been omitted due to low concentration. It was also assumed that precipitation would initially occur at the same product of $[\text{Ca}^{2+}]$ and $[\text{SO}_4^{2-}]$ in the retentate. This was done to account for the effect that the presence of Cl^- and Mg^{2+} had on solubility of gypsum. The formation of gypsum reduces the rate of increase of Ca^{2+} in the retentate. As MgSO_4 is soluble, Mg^{2+} does not precipitate and continues to become concentrated in the permeate. The concentration of Cl^- was determined by charge balance. The concentration of TSS has been plotted on Figure 4.4 to compare the concentration of gypsum crystals to Ca^{2+} and SO_4^{2-} concentrations during water recovery.

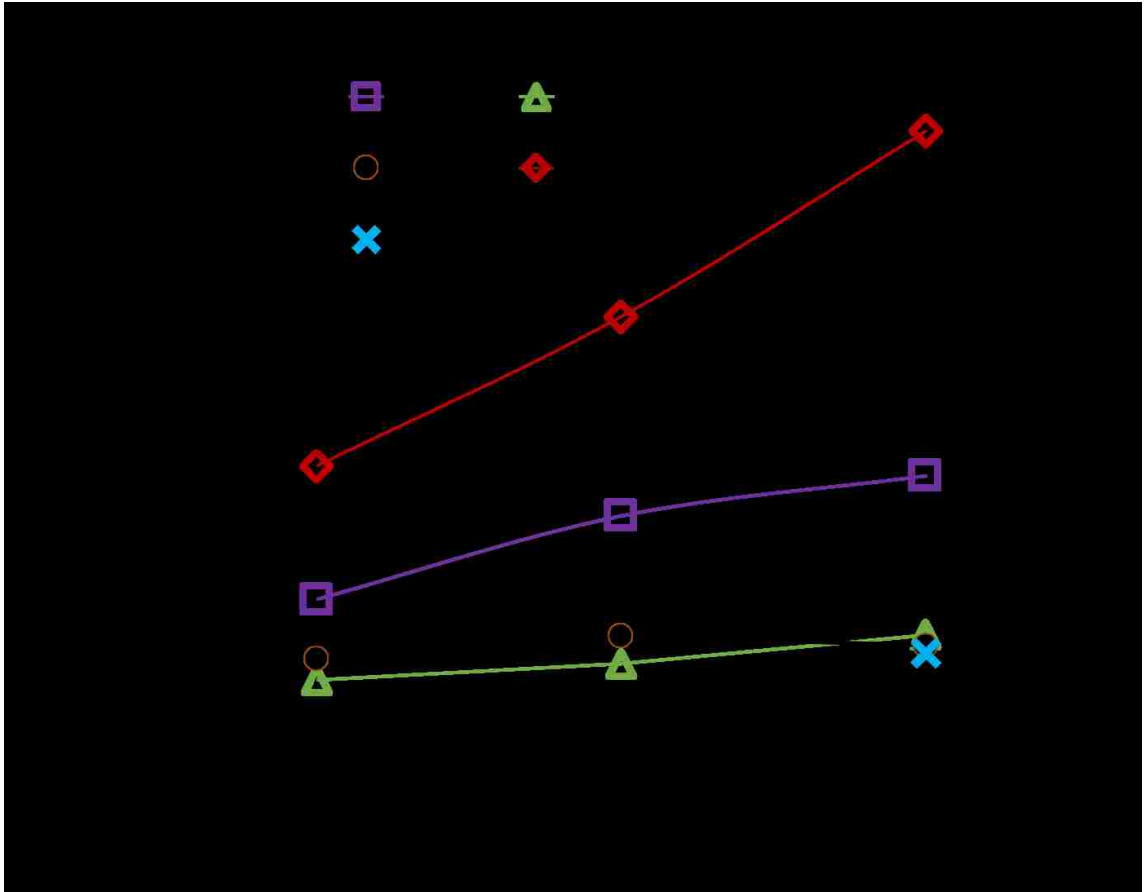


Figure 4.4: Retentate concentration during feed and bleed recovery of Plant Bowen scrubber water... Assume $\Delta P=13.8$ bar and cross flow is maintained at 11.4 L/min. Feed pH =4.5.

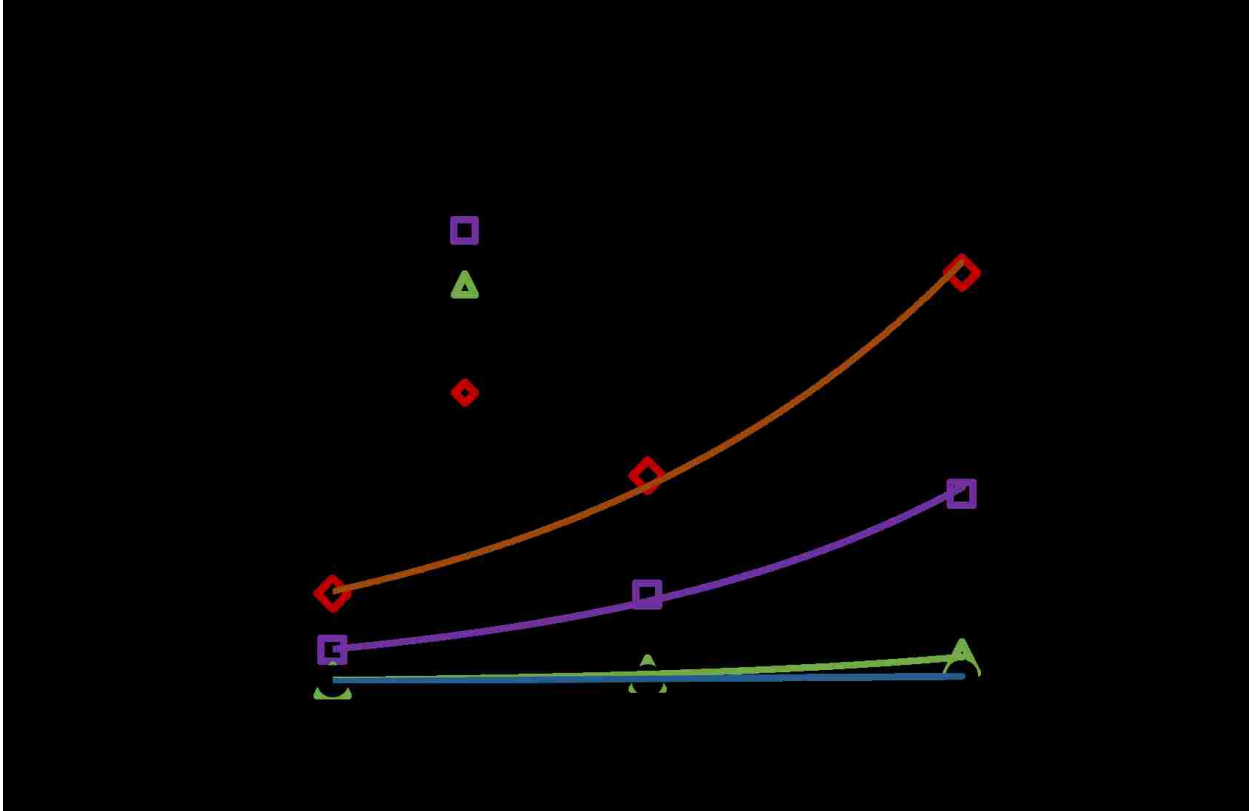


Figure 4.5: Overall permeate concentration during feed and bleed recovery of Plant Bowen scrubber water. Assume $\Delta P=13.8$ bar and cross flow is maintained at 11.4 L/min. Feed pH = 4.5.

4.3.5 Long Term Module Stability

The spiral wound membrane module was tested over the course of 144 days. Figure 4.6 shows the water permeability of the membrane during testing. A wide range of feed concentrations and temperatures were tested, including feed solutions containing over 10,000 mg/L TDS. Water permeability is dependent on the viscosity of water. Viscosity normalized permeability was calculated by the following equation.

$$A_{\mu} = \frac{J_w}{(\Delta P - \Delta \Pi) \left(\frac{\mu}{\mu_{@25^{\circ}C}} \right)} \quad (6)$$

Viscosity of water at a given temperature was interpolated from data from Kestin et al.⁸² As can be seen water permeability of the membrane remained stable over the course of testing, decreasing at most 20% after a time period of 144 days of on and off testing. The flux stability of the spiral wound membrane elements over a long span gives confidence for the comparing membrane behavior over the course of testing. The packaging of the membrane inside the spiral wound element and pressure cell prevented damage from factors outside of the testing, such as the physical damage that can result from mounting or removing flat sheet membranes from testing cells.

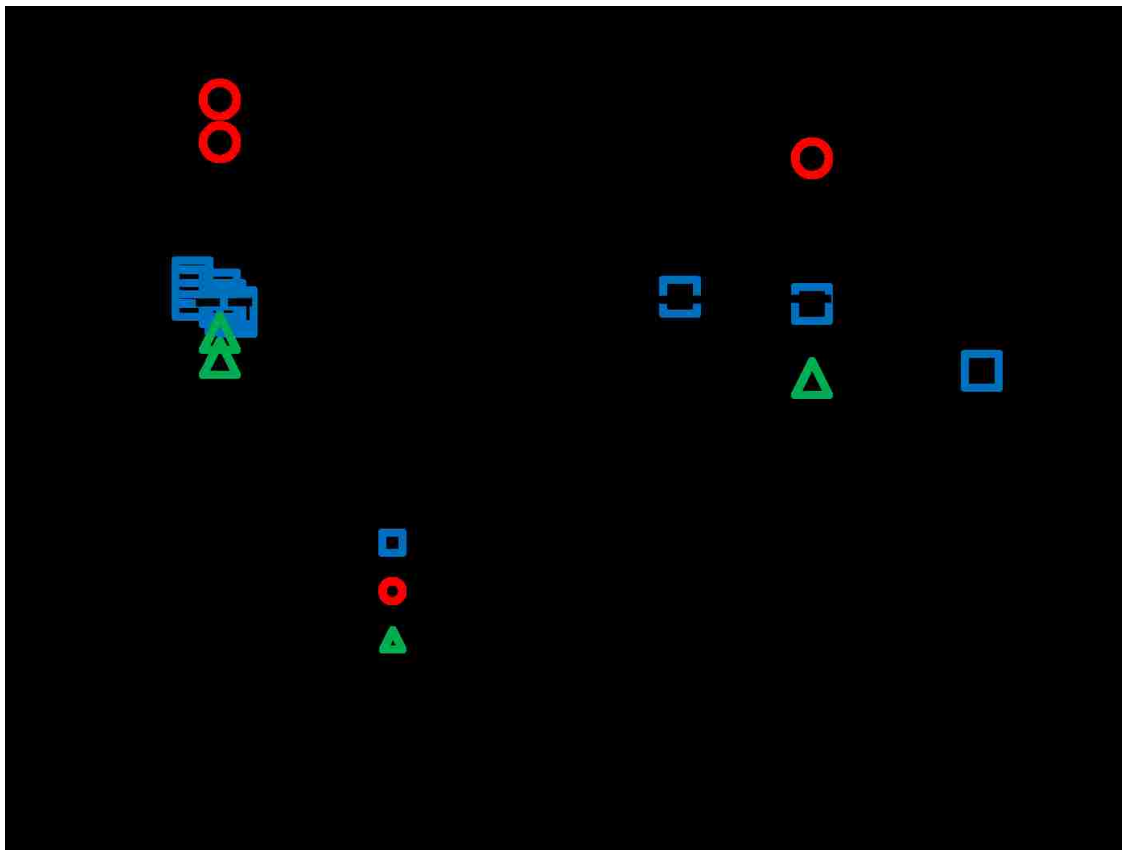


Figure 4.6. PNF2A Stability over the course of testing. Temperature varied throughout testing. Outlying values of high permeability were observed during high temperature runs (~44°C). Viscosity and osmotic pressure used to correct experimental data for comparison.

4.3.6 Heavy Metal Remediation

In addition to the rejection of major ions contributing to TDS in the FGD water, significant rejection of trace heavy metals was achieved, among them selenium being a primary concern. Results for the rejection of trace metals in PNF2A can be seen in Figure 4.7. Speciation of PNF2A permeate revealed presence of both Se (IV) and Se (VI). The pKa2 for H₂SeO₄ is determined to be 2, therefore all selenate is present in the solutions as SeO₄²⁻, a divalent anion. Rejection of SeO₄²⁻ can be predicted to bear similarity to the rejection of SO₄²⁻ ions. H₂SeO₃ has a pKa1 of 2.46 and pKa2 of 7.31 and is present in solution predominantly as HSeO₃⁻ in the slightly acidic scrubber wastewater⁸³. Theoretically SeO₄²⁻ would be rejected at greater amounts as compared to SeO₃⁻ due to the greater negative charge. Experimentally the rejection is also influenced by the ratio of divalent cations to monovalent cations than the composition of Se.

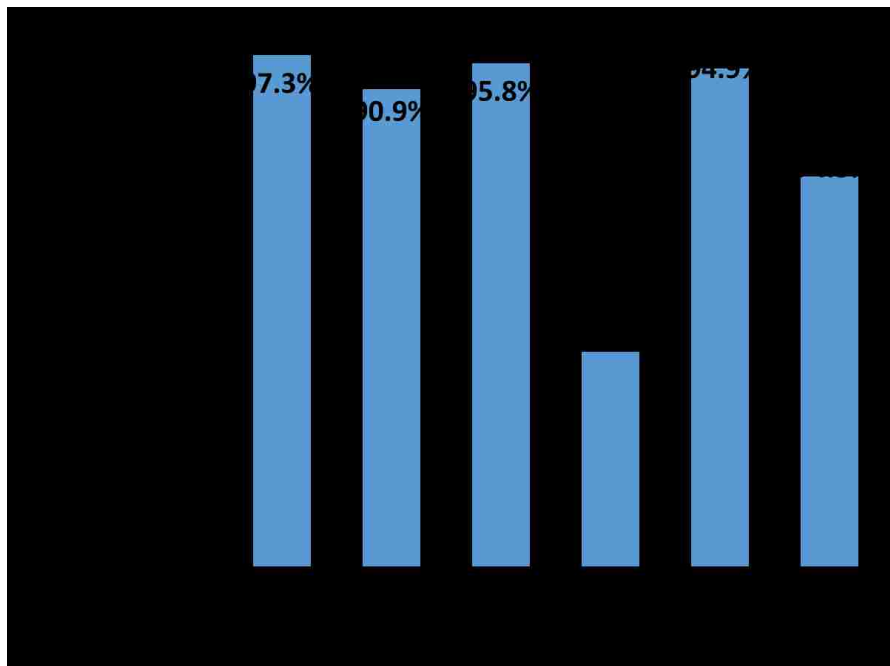


Figure 4.7: PNF2A rejection of various trace metals in FGD process water from Plant Bowen. Water flux for PNF2A was 32.2 LMH. Temperature and operating pressure was maintained at 25°C and 13.45, respectively. Feed pH =4.5.

Permeate can be further polished utilizing iron/iron oxide functionalized membrane to reduce Se concentration below 10 ppb. Nanofiltration has been shown to improve capture of Se in functionalized membrane processes by removing SO_4^{2-} ions that compete with SeO_4^{2-} and SeO_3^{2-} at the active sites of iron nanoparticles⁸⁴. This behavior is shown in Figure 4.8 Se conversion in NF permeate is like that of DI water, while conversion suffers due to SO_4^{2-} presence in scrubber wastewater. Nanofiltration allows for the concentration of Se into the smaller retentate volume, while SO_4^{2-} does not significantly increase during water recovery due to precipitation of gypsum. The precipitation of gypsum is advantageous in this scenario, as further concentration of sulfate ions would further hinder Se capture. The most optimal combination of NF membranes and iron functionalized membranes can be seen in Figure 4.9. Permeate is recycled back into the FGD unit, while SO_4^{2-} in the retentate is crystallized as CaSO_4 before the retentate is passed through the iron functionalized membrane for Se capture.

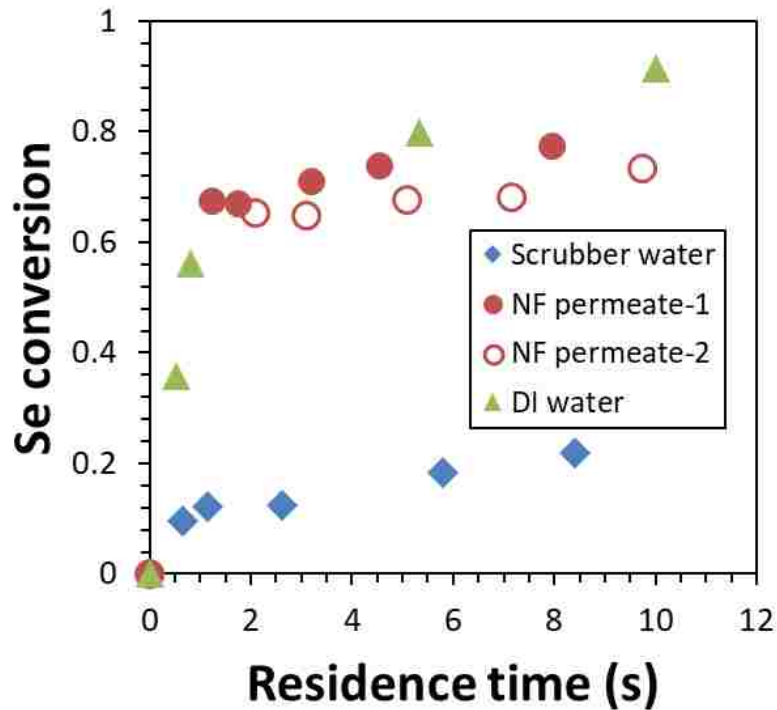


Figure 4.8. Selenium removal with iron functionalized membranes in different water matrix under convective flow condition. $[Se]_0=1.3\pm 0.1$ mg/L in scrubber water, $[Fe]_0=8.4$ mg (20.7 % weight gain), $[TDS]_0=12$ g/L ($[SO_4^{2-}]_0=11.7$ mM or 1120 mg/L); $[Se]_0=52.3$ μ g/L in NF permeate-1 (positively charged NF membrane), $[Fe]_0=9.9$ mg (23 % weight gain), $[TDS]_0=2.4$ g/L ($[SO_4^{2-}]_0=292$ μ M or 28 mg/L); $[Se]_0=11.0$ μ g/L in NF permeate-2 (negatively charged NF membrane), $[Fe]_0=9.2$ mg (23 % weight gain), $[TDS]_0=0.92$ g/L ($[SO_4^{2-}]_0=0.094$ μ M or 9 mg/L); $[Se]_0=2\pm 0.2$ mg/L in DI water, $[Fe]_0=4.0$ mg (12.5 % weight gain). pH of feed solution: 4.5-5.5.

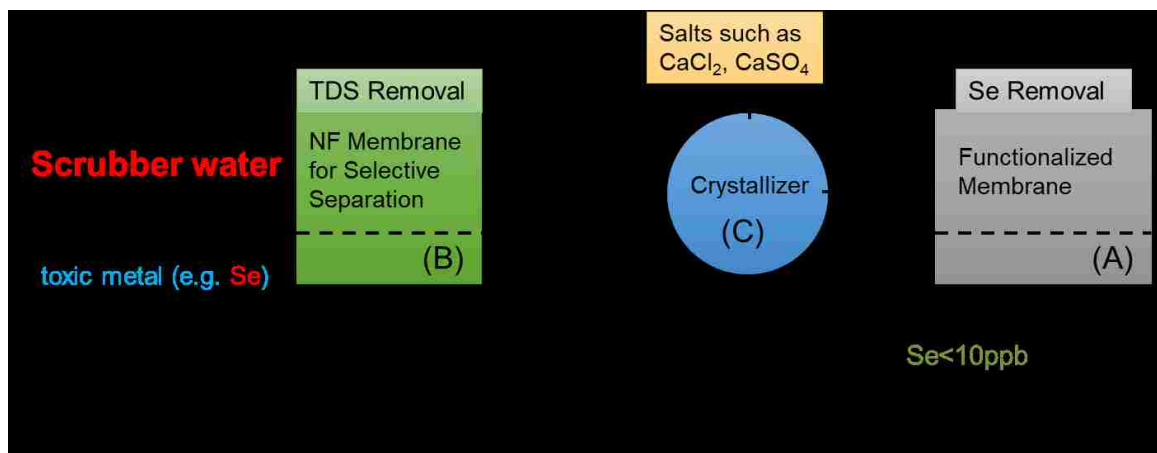


Figure 4.9. Process for combine TDS removal and Se capture for FGD scrubber water reuse and remediation.

4.3.7 Naphthenic Acid Removal from Produced Wastewater

Oil sands produced water containing naphthenic acid was investigated as another potential water source for membrane treatment. Produced water samples had high concentrations of monovalent ions (Na^+ and Cl^-). Lower activity of ions has been observed for high ionic strengths in several studies. For the ionic strength of 3 mole Kg^{-1} (ionic strength of produced water), Bates et.al.⁸⁵ observed an activity coefficient of 0.71 and 0.50 for NaCl and CaCl_2 , respectively. Using these activity coefficients, we estimated an osmotic pressure of approximately 120 bar for the produced water. Nanofiltration membranes have a low rejection for monovalent ions at such high ionic strengths. Two commercially available NF membranes, NF8 (Nanostone water co.) and NF270 (DOW-FLIMTEC) were investigated for separation of NA from aqueous solutions. Both membranes are polyamide membranes with negative surface potential at neutral pH. The observed pure water permeabilities for the two membranes were 13.4 LMH/bar and 16.7 LMH/bar, respectively.

The selective properties and permeability allow for NF membranes to be considered for concentration of naphthenic acid in produced wastewater. Ideally the majority of process water is recovered as NF permeate of suitable quality for discharge (≤ 10 mg/L naphthenic acid), while the remaining process water present in the retentate can be treated using functionalized membranes or other oxidative methods of degradation⁸⁶. The effective volume of process water to be oxidatively treated is decreased allowing for higher membrane loading and longer residence times to be more attainable to enhance conversion of naphthenic acids. A schematic showing the best utilization of NF membranes alongside iron functionalized membranes can be seen in Figure 4.10.



Figure 4.10. Schematic of suggested use of NF and Iron Functionalized Membranes for naphthenic acid concentration and degradation from high-TDS produced water.

Separation of NA by NF was carried out with NA (Sigma-Aldrich) in DI water, synthetic solution and produced water samples (prefiltered by 0.22 μm filter). High rejection of NA was observed for both DOW270 and Solecta NF8, as shown in Figure 4.11. Rejection studies carried out with the synthetic solution further validated rejection of NA from the produced water. NA molecules contain negatively charged carboxylate group at neutral pH, and therefore, the exclusion of NA by NF membrane is governed by both size and charge exclusion principles⁸⁷. The lower observed rejection of NA (from Sigma-Aldrich) in the produced water matrix is due to the screening of surface charge. Produced water samples have high TDS content, and surface charge of the membrane is shielded by the presence of high concentration of monovalent and divalent ions.

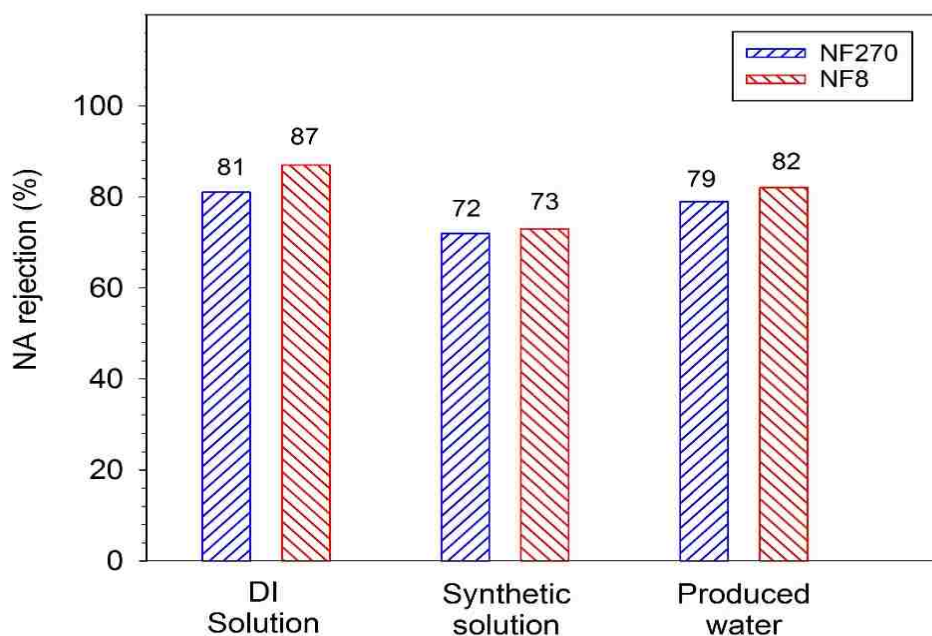


Figure 4.11: Naphthenic acid (NA) rejection by nanofiltration membranes from different water matrices. Synthetic solution: NA concentrations: synthetic solution (mixture from Sigma-Aldrich dissolved in produced water): 38 mg/L, DI solution: 48 mg/L, Produced water: 34 mg/L.

Rejection of salt and water flux was monitored in the cross-flow cell over 20 h, as shown in Figure 4.12. The rejection of various salts is summarized in Table 4.4. Filtration process was operated at near 0% recovery to avoid any significant change in the composition of the feed water over the course of the experiment. Lower ion rejection was observed for produced water samples as compared to the studies with single salt solutions in DI water, which is mainly due to the screening of membrane charge⁸⁸. Despite the low rejection of NaCl of 6.8% and 5% for NF8 and NF270 membranes, the estimated osmotic pressure difference due to NaCl rejection were 4.2 and 2.8 bar, respectively. The major fraction of the applied pressure gradient (6.8 bar) was, therefore consumed to overcome

the osmotic pressure gradient. A decline in flux was also observed over the course of experiment with the produced water (80.4 % and 90% of the initial flux for NF8 and NF270, respectively). After the course of operation, the membrane was washed with DI water, and a flux recovery of 90% and 94% was observed for NF8 and NF270 membrane, respectively. Flux behavior of the produced water with increasing water recovery was also studied for both the membranes in stirred filtration cell operated in dead-end mode.

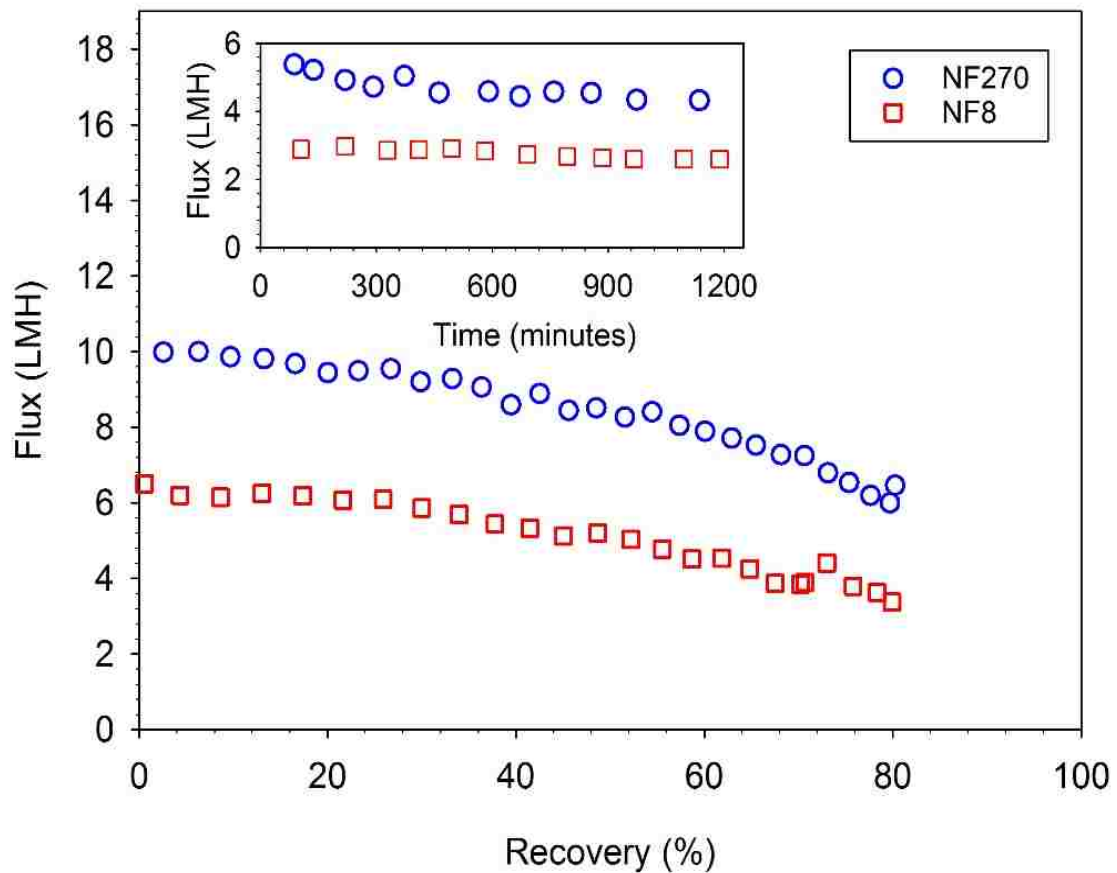
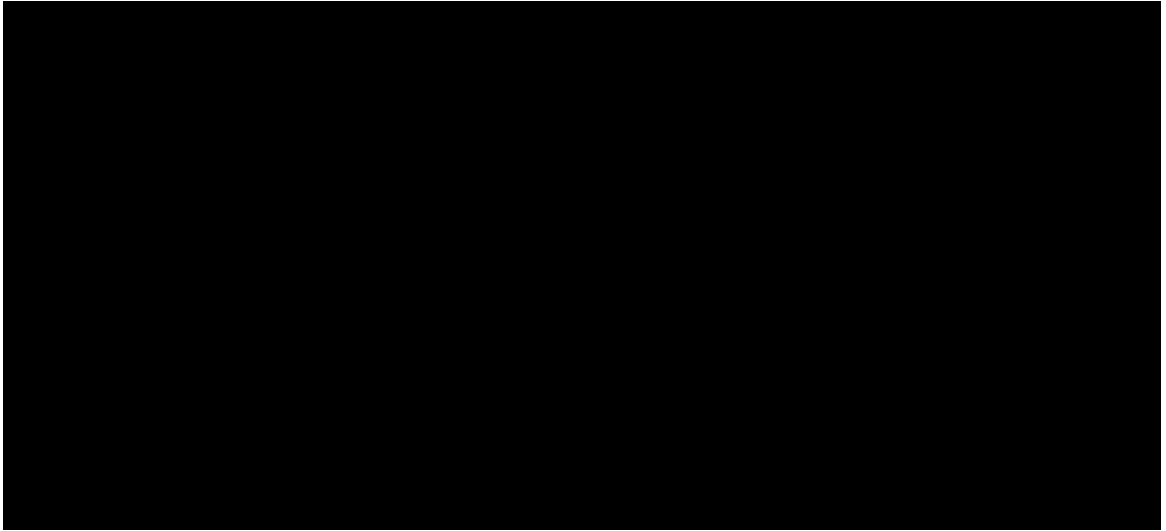


Figure 4.12: Flux of produced water through nanofiltration membrane with increasing water recovery (filtration cell operated at dead end mode, pressure: 10.3 bar, temperature: 22°C). Insert: Flux of produced water through nanofiltration membranes for 20 hours at 0% recovery (filtration cell operated at crossflow mode, Pressure: 6.8 bar, temperature: 22°C)

Table 4.4 NF Rejection of Naphthenic acid and major ionic species in oil sands produced water



4.4 Conclusions

Rejection phenomenon for complex mixed salt solutions has been studied at multiple concentrations and mixtures using charged thin film composite nanofiltration membranes. For single salt solutions, rejection of divalent ions was greater than rejection of monovalent ions, thus consistent with literature. For mixed salt solutions present in equal concentrations by mass, the presence of monovalent ions did not affect the rejection of divalent ions. It was also shown that the effects of charge shielding causes the loss of rejection for monovalent ions to be significantly less than for divalent ions. The selective rejections observed are consistent with literature. Effective desalination of scrubber wastewater contained various ions exceeding 10,000 mg/L TDS was performed using the PNF2A membrane, resulting in high rejections of divalent ions and **trace** metals. Selectivity of NF membranes was critical for maintaining performance in both scrubber and oil sands wastewater.

During water recover operation, 80% of the original feed was recovered as permeate with over 60% reduction in all major ion species. High recovery was also observed for oil sands produced water while naphthenic acid concentration was reduced to acceptable levels. Gypsum formation was found to occur beyond the predicted saturation point due to the presence of Mg^{2+} and Cl^- as counter ions. The gypsum precipitation helped maintain high SO_4^{2-} rejection even at high water recovery. Over the course of several different tests over a 144 day span the spiral wound membrane module appeared to remain flux-stable.

NF membranes were shown to maintain NF desalination was successful for recovering the scrubber water, as water did not to be highly pure to be reused in the process. Gypsum precipitation was shown to aid rejection and decrease the rate of osmotic pressure increase with recovery after the onset of precipitation. No fouling was observed at the concentrations of gypsum present during water recovery, but further tests incorporating higher gypsum concentrations are necessary to more conclusively test fouling. Further study needs to be done on eliminating the residual rejection of monovalent species during water recovery. Even if nominal in terms of percent rejection, osmotic pressure caused by removal of monovalent ions impedes membrane performance and must be eliminated for future process optimization.

CHAPTER 5. CELLULOSE GRAPHENE QUANTUM DOT COMPOSITE MEMBRANES FOR SELECTIVE SEPARATIONS

5.1 Introduction

It has been increasingly demanded for membranes to separate small organic molecules such as pharmaceuticals and dyes^{89,90}. It is a great challenge to separate out molecules smaller than 3 nm. Achieving selective separation as well as a good permeability is the most critical requirement for the future of membrane separations. Besides selectivity, much effort has been made to modify the surface of membrane to increase lifespan or provide additional functions. For example, nanoparticles have been introduced into membranes via a mixed matrix approach to improve selectivity and surface properties⁹¹.

Mixed matrix membranes are typically fabricated by dispersing nanoparticles in the polymer/solvent casting solution to improve the selectivity or to protect the membrane surface against fouling⁹²⁻⁹⁵. In the dispersion, the interaction between nanoparticles and polymers is usually poor, leading to the formation of defects in the membrane. Alternatively nanoparticles are encapsulated by polymer making them inaccessible to solution passing through the membrane⁹⁶. The weak interaction between nanoparticles and polymer matrix can also result in leaching of nanoparticles out of the membrane⁹⁷. In order to evenly distribute nanoparticles throughout the membrane, therefore, it is desirable to have nanoparticles uniformly dispersed in solvent and strongly interact with polymer. This distribution of nanoparticles over the entire membrane further allows the particles to contribute to surface properties and pore formation.

Graphene oxide (GO) has been used as a source material for membrane for both water and gas phase separations⁹⁸⁻¹⁰¹, but the size of GO is too large to modify pore structure when dispersed in polymer-based membranes. GO derived nanostructures have

been successfully integrated into mat materials to provide antibacterial properties¹⁰². However, graphene oxide quantum dots (GQDs) are smaller in size (around 5 nm) while retaining similar functional groups to GO. GQDs can be synthesized in several ways. One common approach is the chemical oxidation of bulk carbon materials. The oxidative cutting of bulk carbon materials generates nanographene sheets terminated with oxygen-rich functional groups such as hydroxyl, carboxyl, and carbonyls¹⁰³. The small size of GQDs results in higher edge area, thus high functionality per the mass of particle. GQDs have a size-dependent band gap due to strong quantum confinement and edge effects, excellent thermal and chemical stabilities, and visible-light-induced photocatalytic activities. Furthermore, GQDs are biocompatible and environmentally friendly^{104, 105}. It has been demonstrated that GQDs may improve membrane performance by unique capabilities such as photo-activity and sensing. For example, a recent article reported that GQDs covalently attached to the surface of a polyvinylidene fluoride (PVDF) membrane displayed antimicrobial properties¹⁰⁶. Incorporation of GQDs onto the surface of nanofiltration membranes was also shown to improve hydrophilicity and reduce fouling¹⁰⁰. GQDs added to an electrospun polyvinyl alcohol (PVA) membrane demonstrated the ability to detect hydrogen peroxide and glucose¹⁰⁷.

The incorporation of GQDs into PVA membrane suggests that a strong hydrogen bonding can be formed between GQDs and hydrophilic polymers containing hydroxyl groups. However, PVA is a not suitable polymer for water-separation membrane as it is water soluble. On the other hand, cellulose based materials have a long history of being used for membranes and are stable in water. Cellulose is a well-known biopolymer rich of hydroxyl groups^{108, 109}. These hydroxyl groups in cellulose form strong hydrogen bonds

with neighboring cellulose chains that are difficult to break. The inability of many commercial solvents to disrupt these hydrogen bonds has limited the utility of cellulose as a membrane material. Although N-methylmorpholine-N-oxide (NMMO) has been used as a solvent to produce regenerated cellulose membranes, this process requires additional chemicals added to the gelation bath ^{110, 111}. Ionic liquids, most notably 1-ethyl-3-methylimidazolium, have been found to be effective at dissolving cellulose by disrupting hydrogen bonding with applied heat ¹¹²⁻¹¹⁴. Cellulose membranes for use in water separations have been prepared via phase inversion using an ionic liquid as a solvent and water as a non-solvent ^{115, 116}. These cellulose membranes have been studied for nanofiltration of organic solvent solutions ¹¹⁷. It was shown that the addition of acetone into the casting solution was shown to have a profound effect on the permeance of ethanol and rejection of organic dyes in solution as well as the surface chemistry of the membrane.

In this work, we seek to integrate GQDs with cellulose membranes to modify membrane selectivity, permeability, and surface characteristics. Unlike conventional approaches to forming mixed matrix membranes where particles are only dispersed through physical blending, this work investigates the use of an ionic liquid which acts as a common solvent for both cellulose and GQDs while creating unique membrane properties. GQDs are bound into the cellulose domain through hydrogen bond networks and stable under convective flow and shear stress. The hydrophilicity of GQDs drives them to the interface between water and cellulose during phase inversion process. This rearrangement allows GQDs to be utilized for enhanced hydrophilicity. A strong hydrogen bonding between GQDs and cellulose was supported by increased viscosity of the casting solution. Furthermore, the incorporation of GQD into the membrane was determined by UV-Vis

absorption measurements. Surface characterizations showed enhanced negative surface charge and hydrophilicity which suggest GQDs are present at the membrane surface. GQD presence within the composite membranes was confirmed through confocal fluorescence microscopy. The addition of GQDs led to notable increase in water permeability from the control cellulose membranes and stability for various temperatures during water gelation. While membranes made exclusively of GO have been shown to remove small organics, they partially reject salt when the full permeation of salt may be desired. The GQD cellulose membranes were shown to perform in the region between UF and NF, selectively separating model dyes between 300 and 10,000 Da while allowing salt to completely permeate through. Flux and dye rejection was shown to be stable during extended testing. Furthermore, GQDs are shown to be retained within the membrane after convective flow of water through the membrane.

5.2 Experimental Methods

5.2.1 5.2.1 Materials

1-ethyl-3-methylimidazolium acetate (EMIMAc, HPLC grade) was purchased from Sigma Aldrich. Avicel® PH-101 microcrystalline cellulose (50µm, cotton linter source) was purchased from Sigma Aldrich. Nonwoven polyester backing material from Nanostone was used as a support for membrane formation. Blue dextran (MW: 5000 Da; 10,000 Da; 500,000 Da) were purchased from Sigma Aldrich for use in membrane pore size characterization. Methylene Blue and Polyethylene Glycol 1000 Da from Sigma Aldrich were used as model dyes to determine the correlation of membrane rejection with molecular weight. Thionine Acetate(90%) was purchased from Sigma-Aldrich for dyeing the membranes for confocal fluorescence microscopy.

5.2.2 5.2.2 GQD Synthesis

Graphene quantum dots (GQDs) were prepared with carbon black (CB) precursor (acetylene carbon black (STREM CHEMICALS)). First, 200 mg of CB were placed in a three-neck round bottom flask. Then, 67 ml of conc: H₂SO₄ (Sigma-Aldrich, ACS reagent 95-98%) and 33 ml of HNO₃ (Fisher Scientific, Assay-69.5%) solutions were added (2:1 volume ratio) to a round bottom flask containing CB. A thermometer was used to monitor the temperature of the solution. After attaching a reflux condenser, the round bottom flask was heated using a silicone oil bath at 105 °C for 5 hours to produce GQDs. Next, the GQDs solution was cooled down to room temperature, and 300 ml of deionized (DI) water was added. The solution was then placed in an ice bath and neutralized using KOH (VWR analytical) pellets. The precipitated salts during the neutralization process were removed by vacuum filtration using a filter paper (VWR,454). The remaining salts in the filtrate containing GQDs were removed by dialysis (1 kD MWCO dialysis bag (Spectrum Labs)) for one week in DI water. Finally, solid GQDs were obtained by drying the solution at low humid environment at 50 °C under vacuum.

5.2.3 Cellulose membrane preparation

10 wt.% Avicel PH-101 microcrystalline cellulose was dissolved in 1-ethyl-3-methylimidazolium using physical mixing for 5 minutes followed by 8 to 24 hours in a sonication bath at 60 °C. The polyester support material was affixed to a glass plate using tape. The casting solution of ionic liquid and cellulose was cast directly onto the polyester backing using a doctor blade set to 150 μm. The polyester backing was then submerged in a water or isopropanol gelation bath for 10 minutes to allow time for membrane formation. The resulting membrane was stored in DI water at a temperature of 4°C until use. A schematic of the process can be seen in Figure 5.1.

5.2.4 GQD cellulose acetate membrane

Cellulose Acetate (CA) from Sigma Aldrich ($M_n \sim 50,000$) was dissolved (17 wt%) in a 6:1 acetone to water mixture to create a membrane casting solution. GQD were dispersed (0.01 wt%) in a casting solution of the same composition.

5.2.5 GQD Cellulose membrane preparation

GQD cellulose composite membranes were prepared in the same manner as cellulose membranes with one major difference. Graphene quantum dots are dissolved in the ionic liquid prior to the dissolution of cellulose. The concentration of GQD used in the casting solution used is 0.05 wt% unless otherwise stated. Membrane thickness, backing material, and coagulation time were all the same as that of the unmodified cellulose membrane preparation.

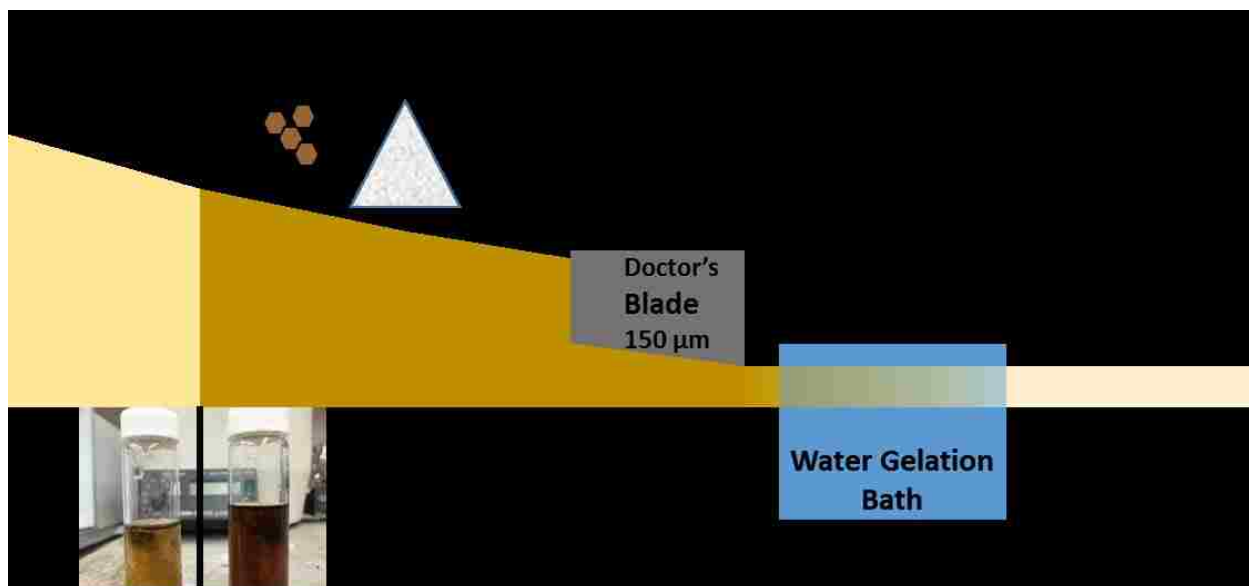


Figure 5.1. Schematic of dissolution of GQD and Cellulose in ionic liquid and subsequent casting of GQD cellulose membrane.

5.2.6 Casting Solution Viscosity

The viscosity of ionic liquid solutions of cellulose and GQD were measured using a TA Instruments Discovery HR-3. Viscosity was measured at 25°C for shear rates between 0 to 100 s⁻¹ to discover how viscosity changes during the shear forces applied when the membrane is cast. A cone and plate geometry was used, and care was taken to remove any air bubbles from the viscous ionic liquid/cellulose solution.

5.2.7 Quantification of GQD loaded on the membrane

GQDs have a broad UV-Visible absorption ranging from 200 nm to 650 nm. The amount of GQDs loaded into the membrane was determined by conducting UV-Visible absorption measurements on a controlled volume of water nonsolvent bath used for the phase inversion process. Equal ionic liquid concentrations were maintained in the casting solutions to remove the interference from the background. Membranes were prepared using 130 mg of casting solution (10 wt% cellulose) in a 20 ml coagulation bath. Membrane thickness (300 µm) was controlled by spin coating in a planetary mixer. Mass of GQDs in the casting solution is 0.1042 mg. Membranes were left overnight in the coagulation bath to complete the phase inversion process. Calibration standards for GQDs were prepared using the solution obtained in coagulation bath after phase inversion of blank cellulose membrane. Absorbance at 425 nm was used to determine the remaining amount of GQDs.

5.2.8 Zeta potential characterization

Zeta potential of cellulose and GQD cellulose membranes was measured by an Anton Paar Surpass 1 electrokinetic analyzer. The adjustable gap cell was used with a 100µm gap and 0.01 M KCl electrolyte solution. Acid titration was done with 0.01 M HCl. 400 mBar pressure difference was used for all measurements.

5.2.9 Contact angle characterization

The contact angle for deionized ultrafiltered water was measured using the Kruss DSA 100. At least 5 spots per membrane sample were analyzed to correct for any variance in surface morphology. Each membrane was rinsed in isopropyl alcohol (IPA), then submerged in IPA for 30 minutes and allowed to air dry to prevent adhesion forces caused by residual water at the membrane surface to reduce the contact angle.

5.2.10 Confocal Fluorescence Microscopy

In order to further quantify the presence of GQD, membranes were analyzed in the Olympus FV1200. Before microscopy 50 mL of 10 mg/L thionin acetate dye solution was passed through the membranes. After dye passage, 200 mL of Phosphate Buffer Solution (pH ~ 7.4) was permeated through each membrane to remove any excess dye. This procedure was performed for an unmodified cellulose membrane, for use as a blank, as well as GQD Cellulose membranes prepared with both water and IPA. The surface of each membrane was analyzed at 4x zoom to obtain an overall map of fluorescence on the membrane surface. The excitation wavelength used was 488 nm. Two areas of the emission spectra were analyzed: 525-535 nm which corresponds to GQD fluorescence and 580-590 nm, which corresponds to any adsorbed thionin acetate dye.

5.2.11 Determination of Membrane Morphology

For SEM characterization, a sample was prepared by freeze-drying and cryo-cracking for both the cellulose-only and GQD-cellulose composite membrane. SEM images were acquired using the Hitachi 4300 SEM. To further investigate the cross-section of the membrane, ion beam of the FEI Helios Nanolab Dual beam was used to cut out a small piece of the membrane. A small deposit of platinum (~60 nm thick) was first deposited over the area to protect the underlying surface while the ion beam is cutting a

cross section. A small cross section was cut out and lifted away from the rest of the sample by welding a small bead of platinum to the platinum layer. This sample was then thinned out with a low power ion beam until the morphology of the mesoporous layer was visible using STEM mode in the Dual Beam. This sample was transferred into the JEOL 2010F for TEM imaging of the cross-section. Further analysis using XRD was performed to determine crystalline structure of the membrane after phase inversion.

5.2.12 Membrane Performance

Membrane performance was characterized by using the Sterlitech HP4750 stirred cell to perform convective studies. Water permeability was determined for each membrane by measuring the volumetric flux of DIUF at 1.4, 2.76, and 4.14 bar respectively. Methylene blue (5 mg/L), as well as various molecular weights (5kDa, 10kDa, and 50kDa at concentrations of 100 mg/L) of Blue Dextran, were filtered through the membrane. The permeate was collected and dye concentration for the feed, permeate, and remaining retentate was analyzed using the VWR UV-6300PC Spectrophotometer. Long term separation studies were conducted using the Sterlitech HP4750 cell by allowing convective flow for 1-hour intervals @1.4 bar, analyzing the permeate and retentate , then returning both solutions to the feed in the stirred membrane cell.

5.2.13 GQD Leaching in GQD cellulose membranes

GQD leaching in membranes was studied by collection DIUF water permeate in 5mL intervals immediately after membrane formation and washing. UV-Vis was utilized to determined absorbance characteristic for both ionic liquid and GQD in the permeate.

5.2.14 XRD characterization of microcrystalline cellulose and composite membranes

Powder XRD measurements were performed to obtain information regarding changes in crystallinity during the formation of the membrane. Before the XRD analysis, blank cellulose membrane and GQD-cellulose membranes were freeze dried and ground to a fine powder. Avicel PH-101 Microcrystalline cellulose powder was used as the standard.

5.3 Results and Discussion

5.3.1 GQD Characterization

The chemical structure of GQD will strongly influence the nature and functionality of the product. A hypothetical structure of a GQD is shown in Figure 5.2. The abundance of oxygenated chemical groups in GQDs comes from the chemical oxidation process used for the synthesis of GQDs. The abundant oxygenated functional groups and their electrostatic charges make GQDs readily soluble in both water and ionic liquid, as can be seen in Figure 5.3.

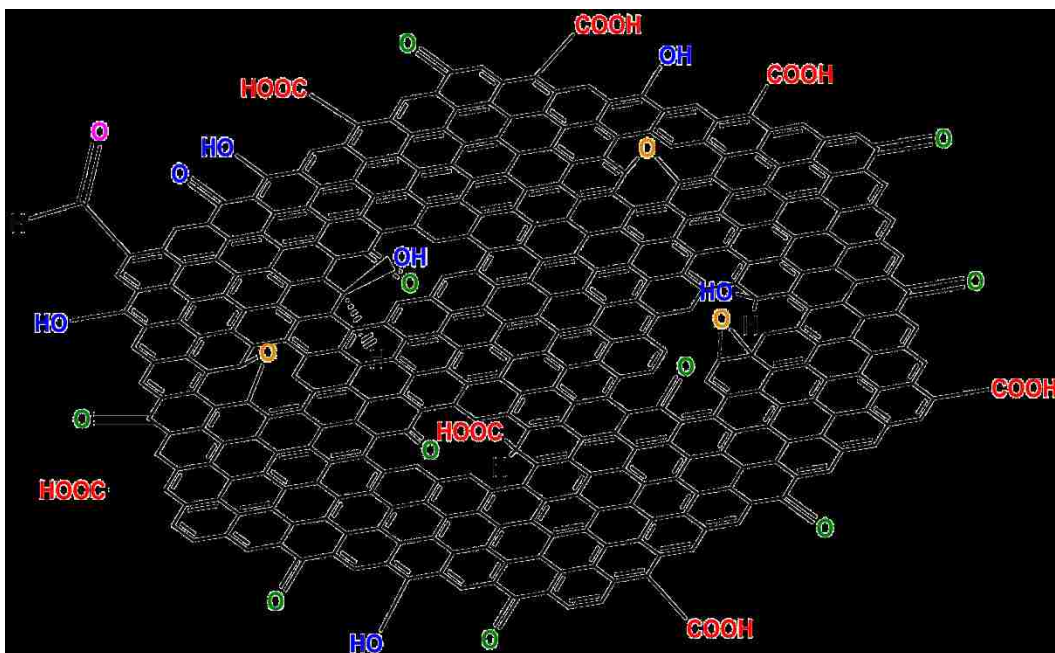


Figure 5.2. Typical Structure and Functional Groups of GQDs.

The UV-Visible absorption spectrum of a GQD suspension is shown in Figure 5.4. High energy absorbance of GQD can be assigned to the $\pi \rightarrow \pi^*$ transition in the sp^2 domains. The nonbonding electrons present in the GQDs correspond to oxygen functional groups such as C=O or C-O yield $n \rightarrow \pi^*$ transitions.¹¹⁸

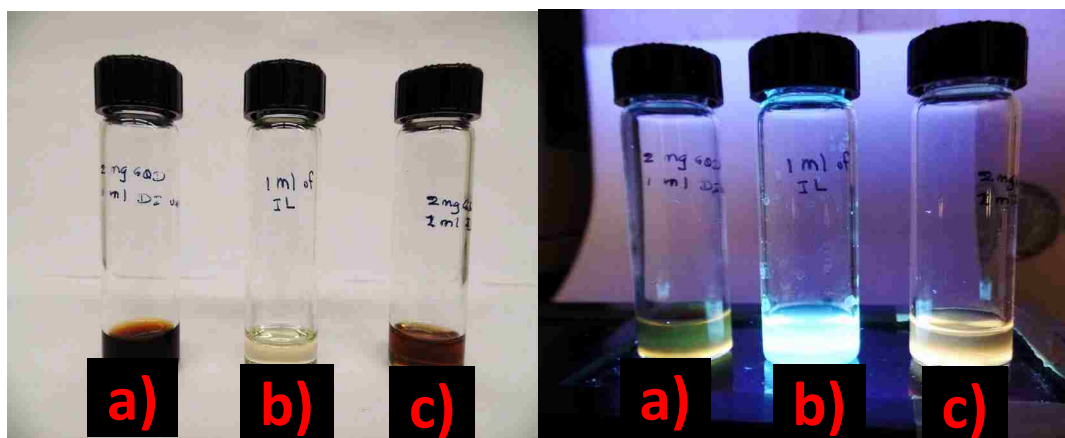


Figure 5.3. Solutions a) 2 mg/ml GQD, b) 1-Ethyl-3-Methylimidazolium Acetate c) 2 mg/ml GQD in 1-Ethyl-3-Methylimidazolium Acetate under visible and short-wave UV light. As can be seen the GQD are readily soluble in water and ionic liquid, fluorescing under excitation with UV light.

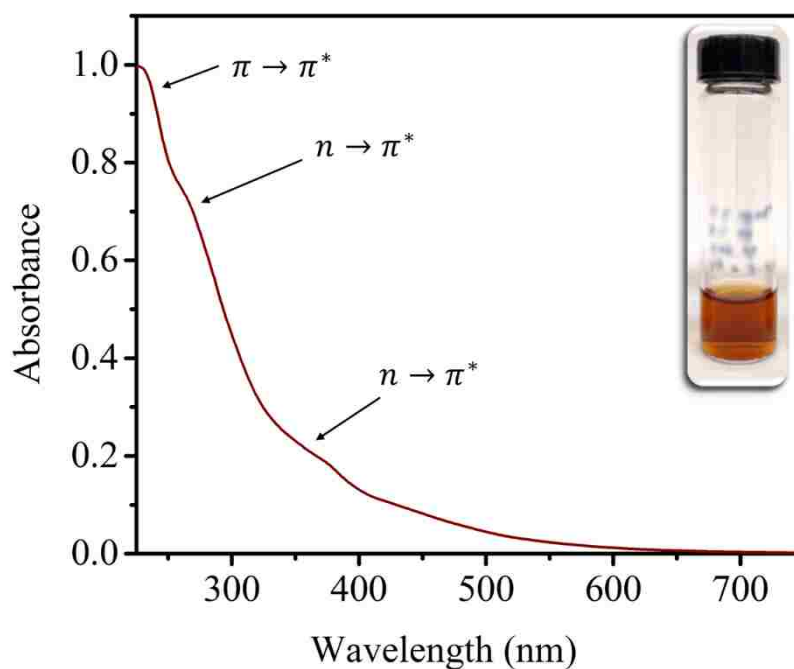


Figure 5.4: UV-Visible absorption spectrum of a GQD suspension

Figure 5.4 shows high-resolution TEM images and FT-IR spectrum of GQDs. As shown in the size distribution histogram of GQDs (right-inset of the figure), the average diameter

of GQD is about 4.8nm. Inset on the left side of the image shows a TEM image of GQDs and reveals the lattice fringes with the spacing of 0.23 nm. This lattice fringe is consistent with graphene oxide. The size of GQDs ranges from 3-7 nm with the average size of 4.8 nm.

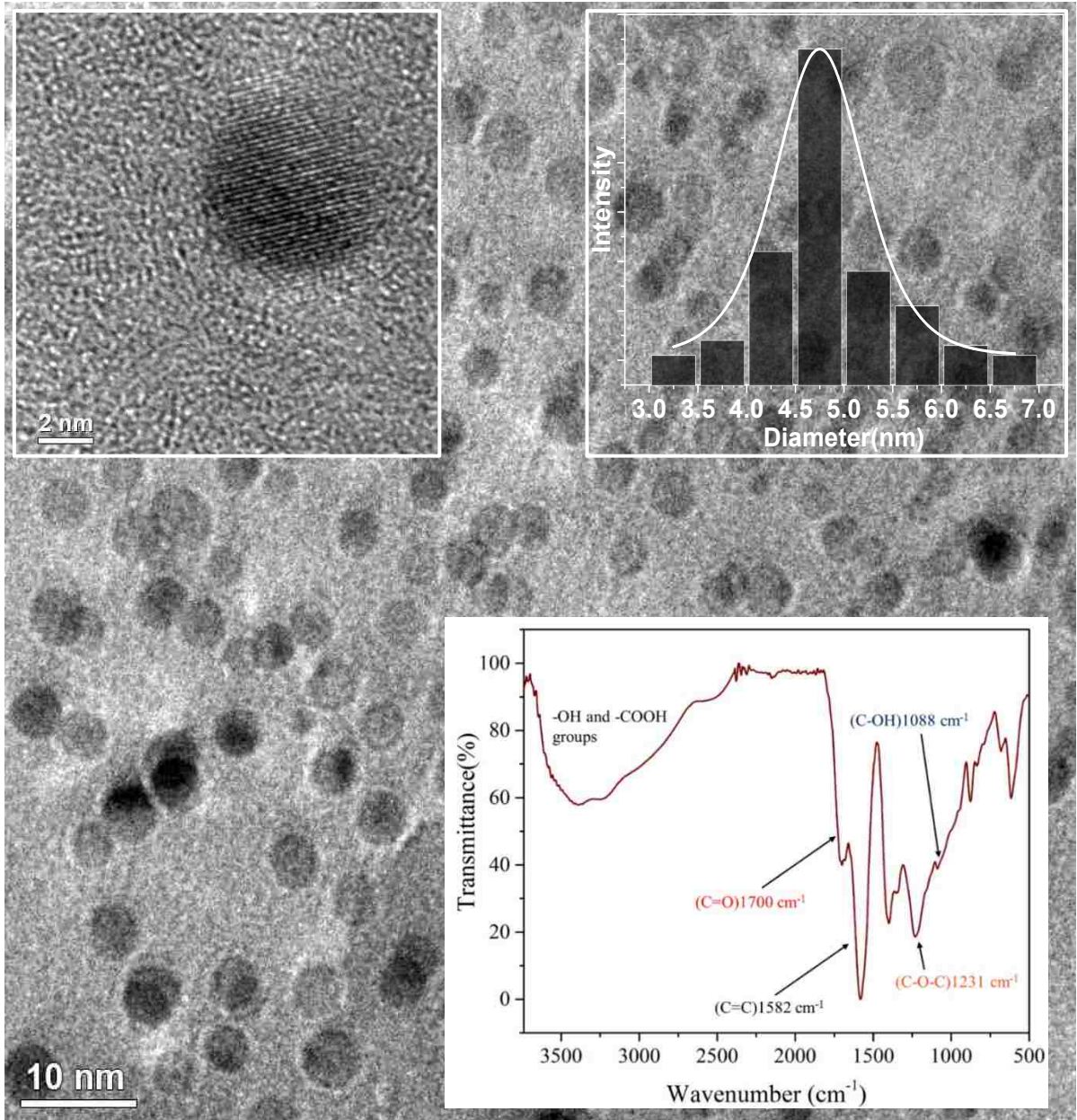


Figure 5.5 TEM image of GQDs, HRTEM of a GQD (top left and bottom), GQD size distribution histogram (top right), and IR (bottom inset).

FT-IR spectrum showed the presence of surface functional groups of GQDs. Figure 5.5 shows the characteristic band of C=O/O–C=O stretching around 1700 cm^{-1} , the vibration band of benzene C=C ring skeletal around 1582 cm^{-1} and the broad peak of O-H vibrations from alcohols and carboxylic acid groups around 2500 cm^{-1} to 3500 cm^{-1} . The results of TEM, UV-Vis, XPS and FT-IR characterizations indicate that GQD consists of a sp^2 basal plane with various oxygenated functional groups. T XPS was performed to analyze the elemental composition and functional groups of GQD, seen in Figure 5.6. Due to chemical oxidation, GQDs contain several oxygen species. High-resolution C1s spectrum indicates that GQDs mainly consist of -COOH, -C=O and C-OH functional groups.

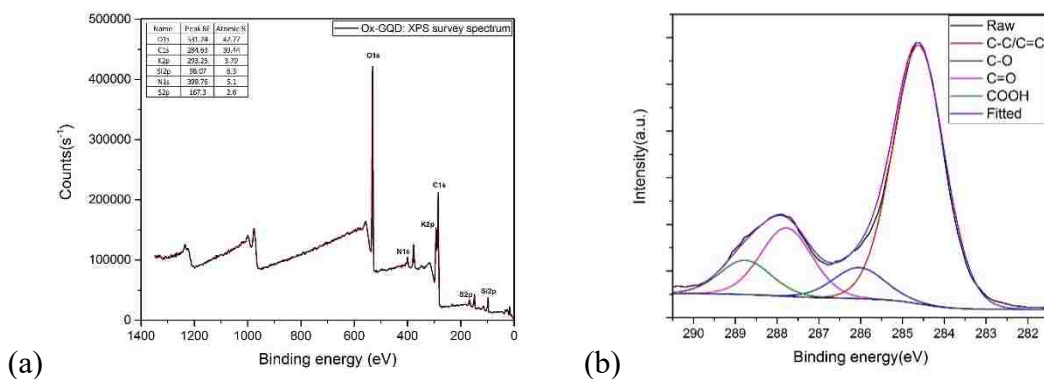


Figure 5.6: XPS spectrum of GQD (a) Survey spectrum. (b) C1s spectrum.

5.3.2 Interaction between Cellulose and GQD in Ionic Liquid

The viscosity of the casting solution is an important factor in the successful casting of phase inversion membranes. The viscosity of the ionic liquid increases from 0.1 Pa*s (the ionic liquid viscosity) to 20 Pa*s, after the dissolution of 10 wt% cellulose. The hydrogen bonding network of the cellulose is rearranged when the casting solution is heated to dissolve the cellulose. The hydrogen bonding domain of the cellulose is penetrated by the

ionic liquid. The viscosity observed for 10 wt. % Avicel PH101 in EMIMAc was comparable to that reported in literature¹¹⁹. As observed by Sescousse et al. the co-presence of the ionic liquid in the hydrogen bonding network of cellulose may increase the distance between cellulose chains, reducing the interaction between chains due to hydrogen bonds. The increased distance between cellulose chains results in lower hydrogen bonding force and reduced viscosity of the cellulose-ionic liquid solution¹²⁰.

The viscosity of 10 wt% cellulose in ionic liquid with different concentrations of GQD can be seen in Figure 5.7. The addition of only 0.05 wt% GQD into the ionic liquid prior to the dissolution of cellulose resulted in much higher casting solution viscosity. The volume occupied by GQDs had a negligible impact on the casting solution viscosity. The higher viscosity was mainly attributed to intermolecular forces between GQD and cellulose. It is presumed that GQDs are located between the chains of cellulose in the casting solution. Cellulose chains are tethered with hydroxyl and carboxyl groups of GQDs through hydrogen bonding interactions. As expected, the viscosity decreased significantly when a lower concentration of GQD was added to solution.

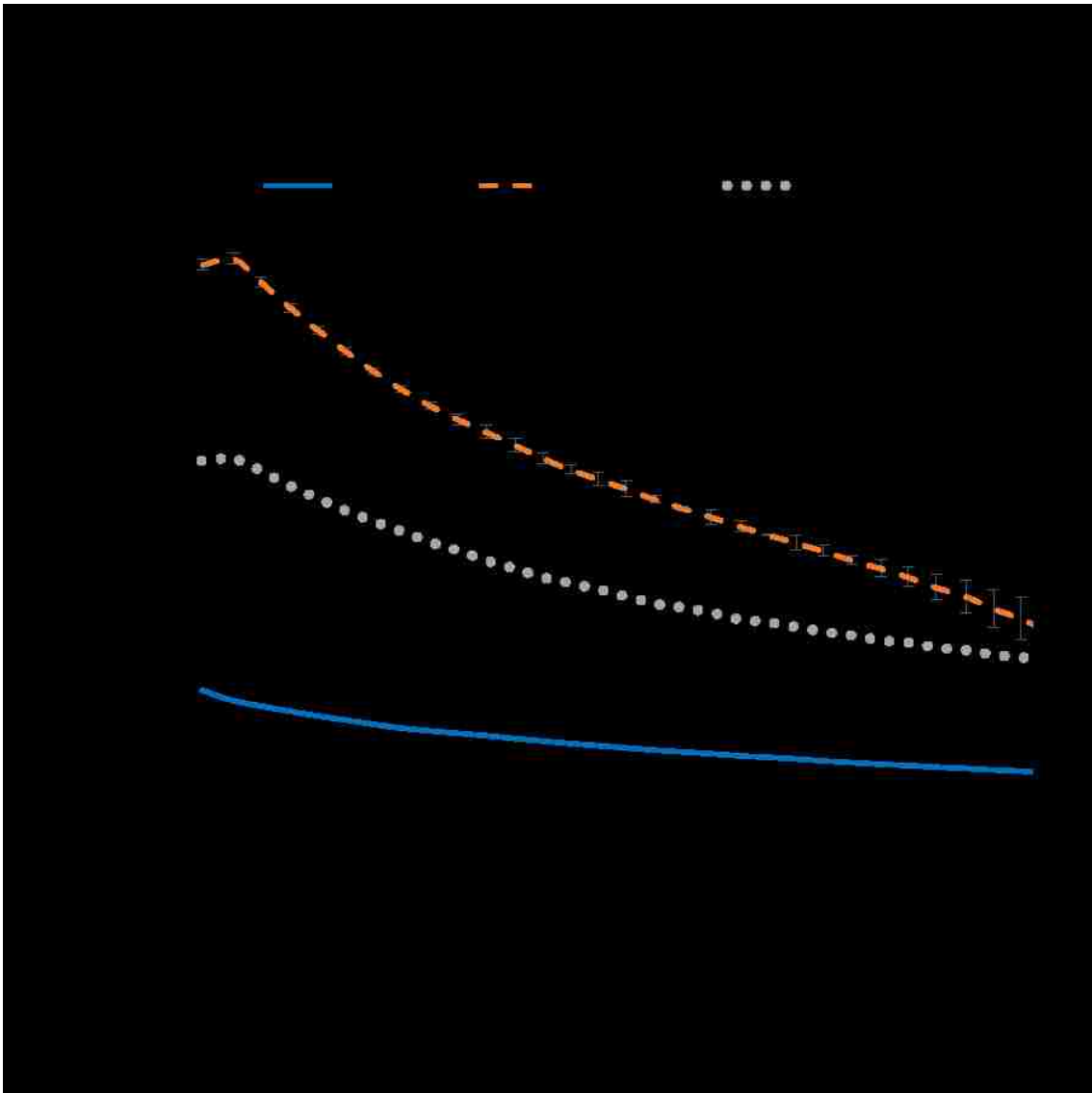


Figure 5.7 Viscosity vs Shear Rate (1/s) for dope solutions (10 wt% Avicel PH-101 in 1-ethyl-3-methylimidazoliumacetate) with 0, 0.025, and 0.05 wt% of GQD added. Known viscosity denoted by dotted line. Average viscosity of 1-ethyl-3-methylimidazoliumacetate solvent was 0.098 Pa s.

The viscosity of the GQD-cellulose-ionic liquid solutions decreased substantially as a function of shear rate. The aspect ratio of graphene quantum dots and the functional groups capable of hydrogen bonding around the edge of the GQDs may allow for hydrogen bond network to reconfigure itself under shear stress, resulting in less tethering of cellulose chains as more stress is applied.

To avoid the aggregation of GQD, a common solvent between the polymer and GQD must be used. Certainly, CA or other hydrophilic polymers could be used. Thus 1-ethyl-3-methylimidazoliumacetate was used as a common solvent. Membranes have been successfully created by phase inversion of a casting solution containing cellulose acetate dissolved in ionic liquid¹²¹. Cellulose is also soluble in the ionic liquid and has many favorable properties including additional hydroxyl groups and solvent resistant properties. As GQDs integrate into the polymer domain via hydrogen bonding and are also solvent resistant, GQDs and cellulose are complementary materials as both have the extensive capability for hydrogen bonding and are solvent resistant.

5.3.3 Leaching of GQD during Phase Inversion

The strong hydrogen bonding network between cellulose is reformed as the casting solution is submerged in the water gelation bath. A trace amount of ionic liquid was present in the membrane after phase inversion. Significantly, more ionic liquid was detected in the membrane when IPA was used as the nonsolvent in the gelation bath. Thus, ionic liquid concentration correlated to the rate of diffusion into the nonsolvent. The rate of diffusion of phase inversion of a similar ionic liquid, [EMIM]SCN, was shown to be significantly slower in an IPA gelation bath as compared to water¹²². Most importantly, the amount of trace ionic liquid in the GQD cellulose membrane was comparable to that seen in the blank cellulose membrane. Therefore, any differences in membrane surface properties should not be caused by ionic liquid concentration.

The loss of GQD from diffusion into the water gelation bath during phase inversion is a reasonable assumption, as GQDs are readily water-soluble. Phase inversion was done in a series of 20 mL scintillation vials, to quantify the loss of GQD from diffusion, and

determine the concentration of GQDs in the membrane. The absorbance at a wavelength of 425 nm was observed to be linear with GQD concentration in the water nonsolvent and unchanged by the presence of ionic liquid. The calibration curve of absorbance vs. GQD concentration can be seen in Figure 5.8. It was determined from a mass balance that 55% of the GQDs dispersed in the casting solution diffuse into the nonsolvent. Thus, it is reasoned that 45% of the GQDs remain, making up 0.2 wt% of the membrane, excluding the mass of the absorbed water in the membrane.

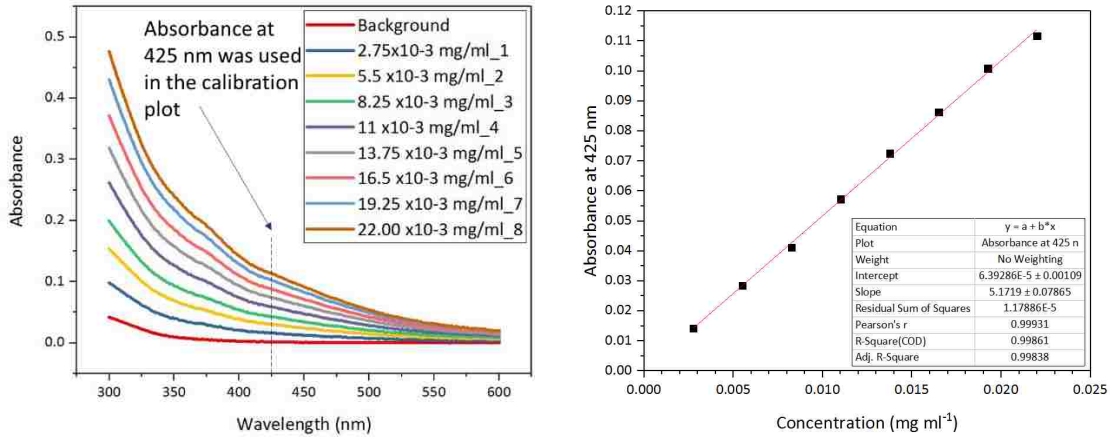


Figure 5.8 : (Left) Absorbance vs. Wavelength for GQD calibration solutions with ionic liquid background. (Right) Calibration curve of absorbance vs. concentration verifying linear behavior.

The concentration of GQD in the gelation bath after controlled phase inversion. Using a mass balance and the initial concentration of GQDs in the casting solution, about 45% of GQDs in the casting solution are incorporated in to the cellulose membrane during the phase inversion process. The determined concentration of GQD in the dry membrane is 0.2 wt%.

The GQDs remaining in the membrane were assumed to be in the hydrogen bond network of the cellulose membrane. Disruption of the hydrogen bonding structure of the microcrystalline cellulose was observed when the XRD pattern of the membrane after phase inversion was compared to the original Avicel PH-101 powder. Figure 5.9 shows the XRD patterns obtained for standard, blank membrane and GQD incorporated membrane. After formation of the membrane, the intensity of the characteristic peak ((200) plane) is significantly reduced and became wider, demonstrating the formation of amorphous regions. No significant differences were noted between blank cellulose membrane and GQD-cellulose membrane. This result indicates incorporation of GQDs does not induce crystallization in cellulose membrane. However, slight high XRD intensity of GQD-Cellulose membrane over blank cellulose membrane is between 20° - 30° may be due to the presence of GQDs because GQDs have a characteristic XRD peak at $2\theta = 25^{\circ}$ due to (002) carbon-to-carbon spacing.¹²³

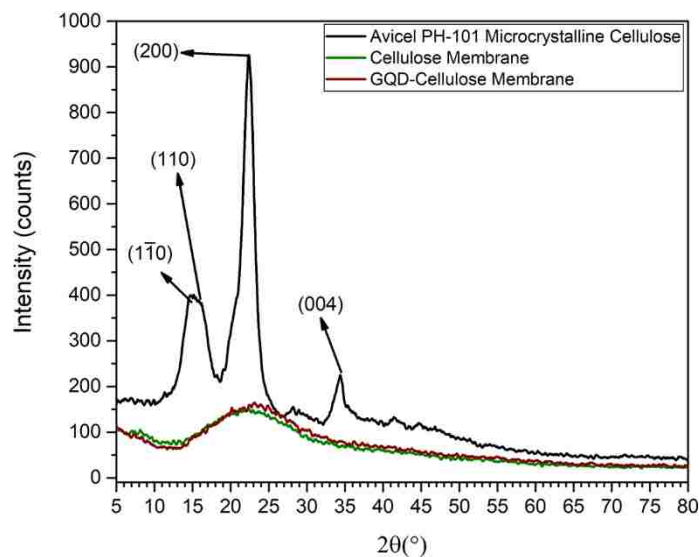


Figure 5.9. XRD analysis of the Cellulose and GQD Cellulose Membrane as compared to the Avicel – PH 101 powder.

5.3.4 Morphology of GQD-Cellulose Composite Membrane

The morphologies of cellulose-based membrane and GQD-cellulose composite membrane were characterized by scanning electron microscopy (SEM) and transmission electron microscopy (TEM). The resultant images are shown in Figure 5.10. The presence of GQD appeared to create a more open structure compared to the dense structure of the unmodified cellulose membranes. The GQD cellulose membrane has an asymmetric structure. Note that the topmost layer was platinum deposited on the membrane surface to protect the morphology during ion beam milling. The dense selective layer appears to only make up the top ~120 nm of the membrane the membrane surface. The top 2 microns were composed of a mesoporous region with voids between 7-40 nm in diameter. The remainder of the membrane material appears to be very open with an apparent shelf-like structure that is not expected to contribute any significant resistance to fluid flow. The unmodified cellulose membrane was observed dense throughout the entire cross-section. Furthermore, TEM image of the selective and mesoporous layer of the GQD cellulose membrane can be seen in Figure 5.11

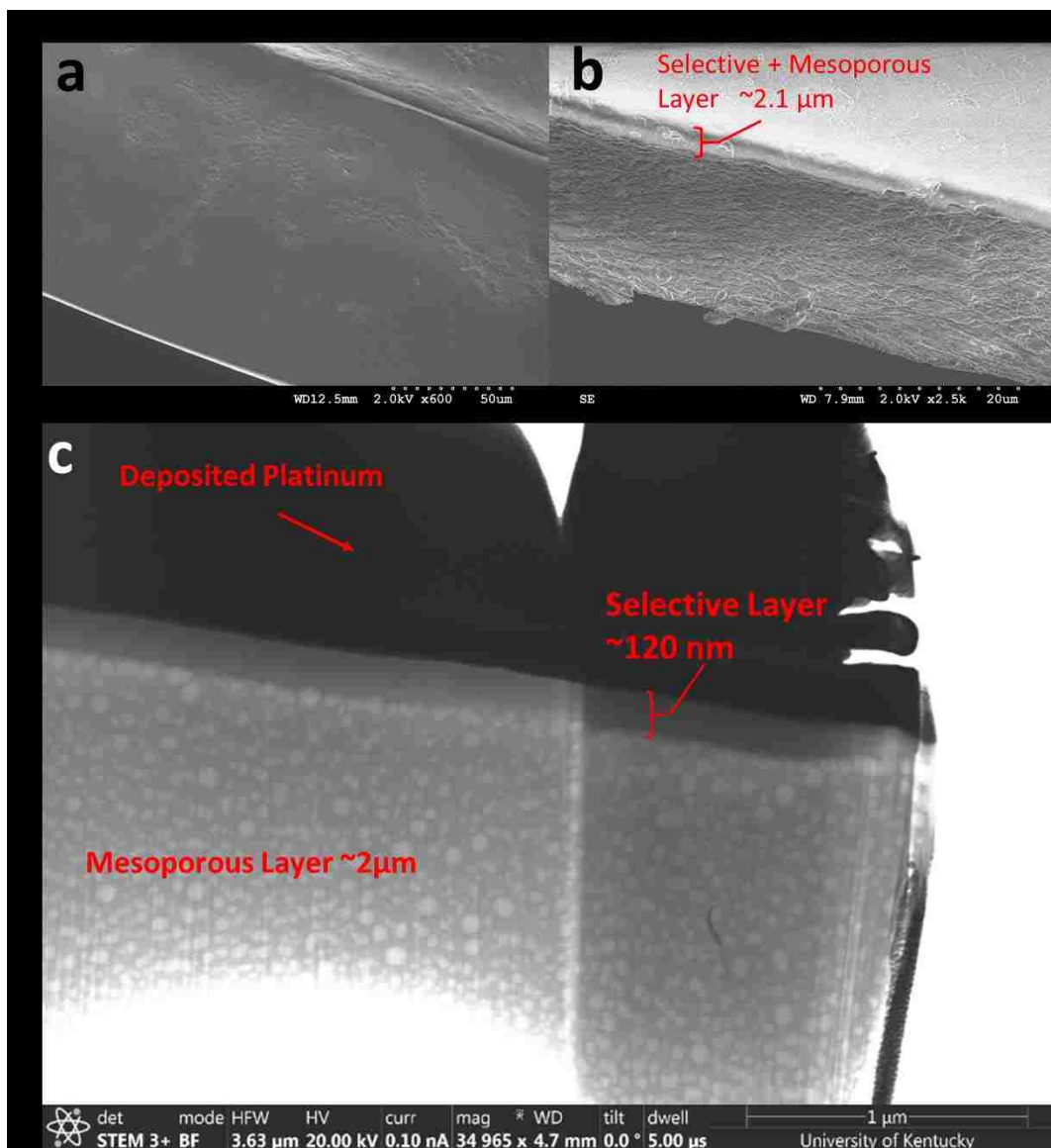


Figure 5.10 a) SEM cross-section of unmodified cellulose membrane. b) SEM cross-section of GQD cellulose membrane. c) STEM cross-section of GQD cellulose membrane.

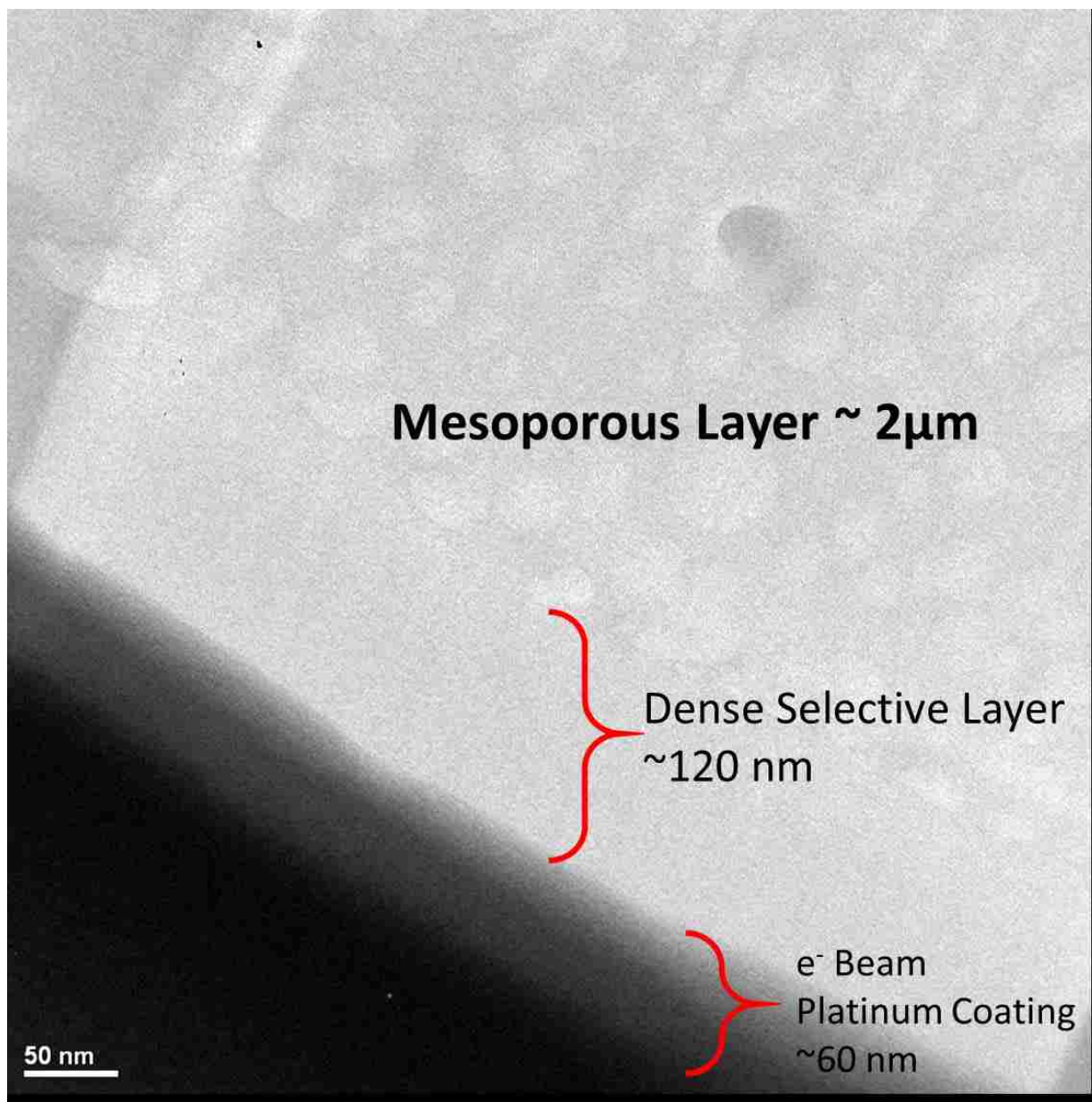


Figure 5.11 TEM Cross-section of GQD/Cellulose with the relevant regions marked.

GQDs were detected during characterization and it is beyond the resolution of SEM top-view and cross-sectional images because of the small size of GQDs and the similar contrast between GQD and cellulose. Large aggregations of GQD should not be present, as they are well dispersed by hydrogen bonding network between GQD and cellulose.

5.3.5 ATR-FTIR characterization of membrane post phase inversion

ATR-FTIR Spectroscopy was performed on the unmodified and GQD cellulose membranes. For the GQD Cellulose membrane the membrane was analyzed after gelation in both IPA and water to determine the role gelation solution plays in GQD concentration. Due to the low concentrations throughout the bulk, no peaks specific to GQD were able to be seen. However the $-C=N$ stretch of the ionic liquid can be seen clearly in all membranes after phase inversion to various degrees. This indicates that some residual ionic liquid remains in the membranes after phase inversion. The membrane cast using IPA has a higher concentration of residual ionic liquid. Furthermore, it can be reasoned dissolution in the ionic liquid did not break down or otherwise alter the cellulose structure as significant $C=O$ carboxyl groups are not evident in the amorphous cellulose membranes. These results can be seen in Figure 5.12.

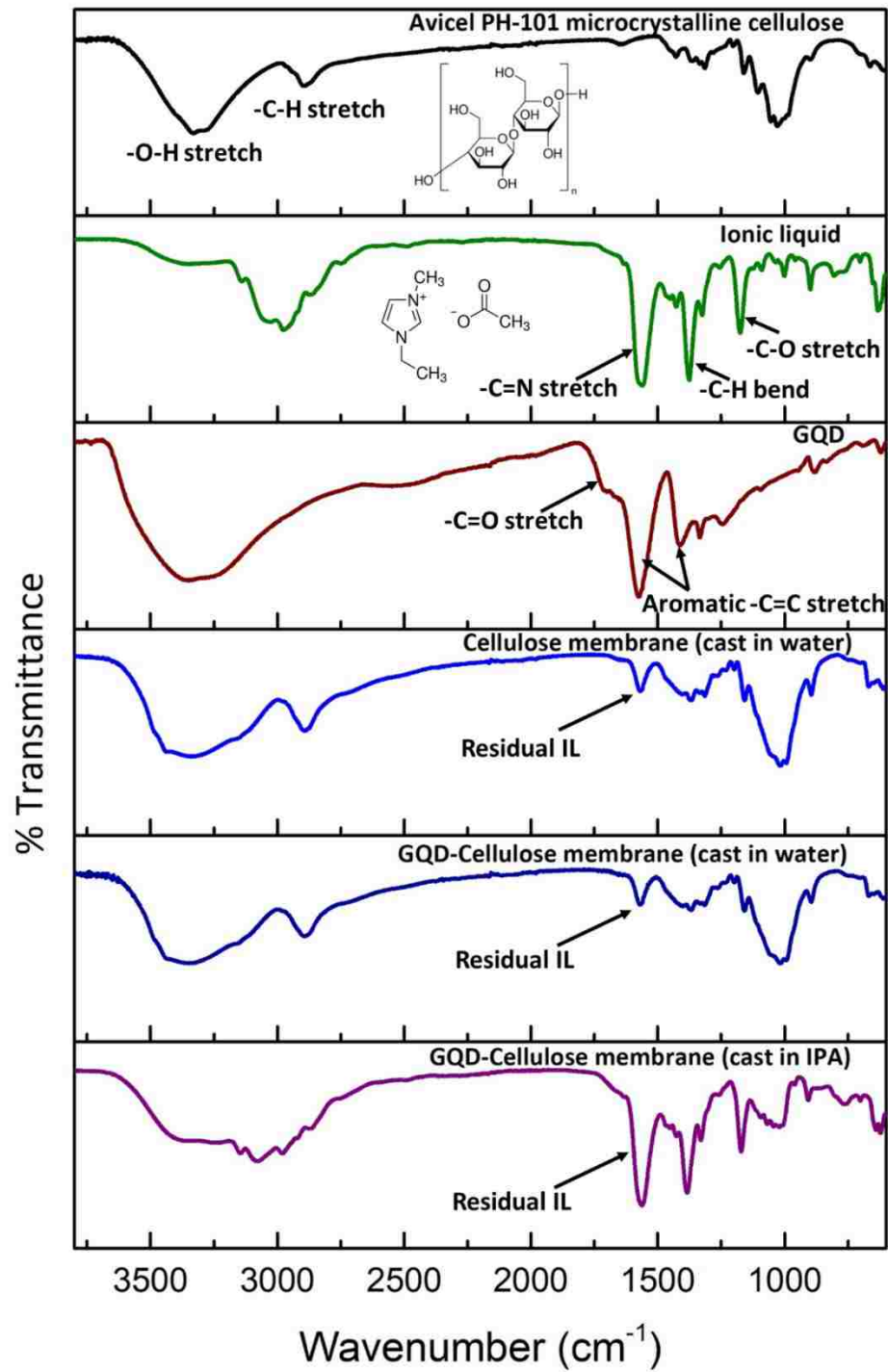


Figure 5.12: FT-IR analysis of membranes and precursor materials

5.3.6 Membrane Surface Properties

Surface characterizations were carried out to probe the presence of GQDs on the surface property of membrane and to explore the impact of GQDs. By measuring zeta potential, surface properties of the GQD-cellulose composite membrane were compared with that of cellulose membrane. The Helmholtz-Smoluchowski equation can be used to determine zeta potential of a membrane by measuring streaming current over a range of pressure drop across a thin channel made by two samples of membrane¹²⁴.

Zeta potential of the cellulose and GQD-cellulose membranes at pH of 3-7 is shown in Figure 5.13. Unmodified cellulose membrane revealed slightly acidic behavior. Literature shows cellulosic materials, and cotton materials such as cloth or medical gauze to have a slightly negative surface charge¹²⁵⁻¹²⁷. Therefore, the negative charge of the unmodified cellulose membrane is expected throughout this pH range. Adsorption of hydrogen ions at low pH might be responsible for the linear change in surface charge as pH is changed. Residual acetate ions from the ionic liquid may also contribute to the negative surface charge. However, the surface charge of the GQD-cellulose membrane was found to be significantly more negative than the unmodified membrane above the pH of 4. This increase in negative surface charge originates from the carboxyl groups present in GQDs other than residual acetate from the presence of any residual ionic liquid, which is shown to be the same for both membranes. The additional charge shift occurs within the pKa range of carboxylic groups^{128, 129}. Therefore, it is reasonable that the GQDs are present at the membrane surface and contribute to the negative charge of surface. Each pH value was tested after at least 3 minutes of rinsing at the experimental shear rate with the electrolyte solution. Since zeta potential only became more positive with the lowering of

pH, it can be reasoned that GQDs on the surface are stable when the membrane is exposed to high shear conditions.

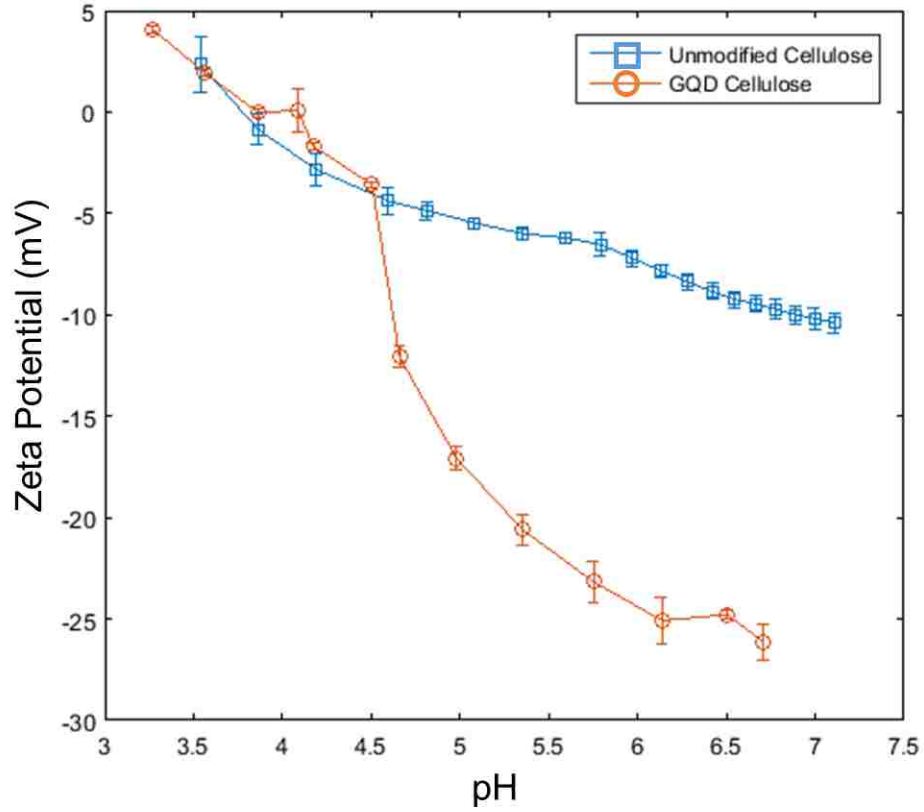


Figure 5.13 Zeta Potential of Unmodified Cellulose and GQD Cellulose membranes. [KCl]=.01M. Flow channel thickness 100 μ m. Pressure range 0-400 mbar.

The zeta potential analysis strongly suggests that GQDs are present on the membrane surface. It is possible that charge from GQD within the membrane could also affect the zeta potential value¹³⁰. The GQD cellulose membrane was shown to have an open structure which could be accessible to electrolyte during streaming potential analysis. Thus, water contact angle was measured to further verify the presence of GQD on the

membrane surface. The contact angle of water was studied for both the unmodified cellulose membrane and the GQD cellulose membrane. A third GQD cellulose membrane was prepared with IPA as the nonsolvent for use as a control case, as GQDs are not soluble in IPA and must remain in the membrane during phase inversion. . It is expected that the difference in hydrophilicity observed for GQD cellulose membranes prepared using an IPA coagulation bath is primarily due to the increased GQD concentration within the membrane. Excess ionic liquid observed in IR (IR penetrates a few micrometers into the membrane) should not be present at the surface after washing the membrane unless imidazolium is adsorbed to GQD on the membrane surface (in which case this is directly dependent on increased GQD concentration). The contact angle and weight fraction within the membrane are shown in Figure 5.14.

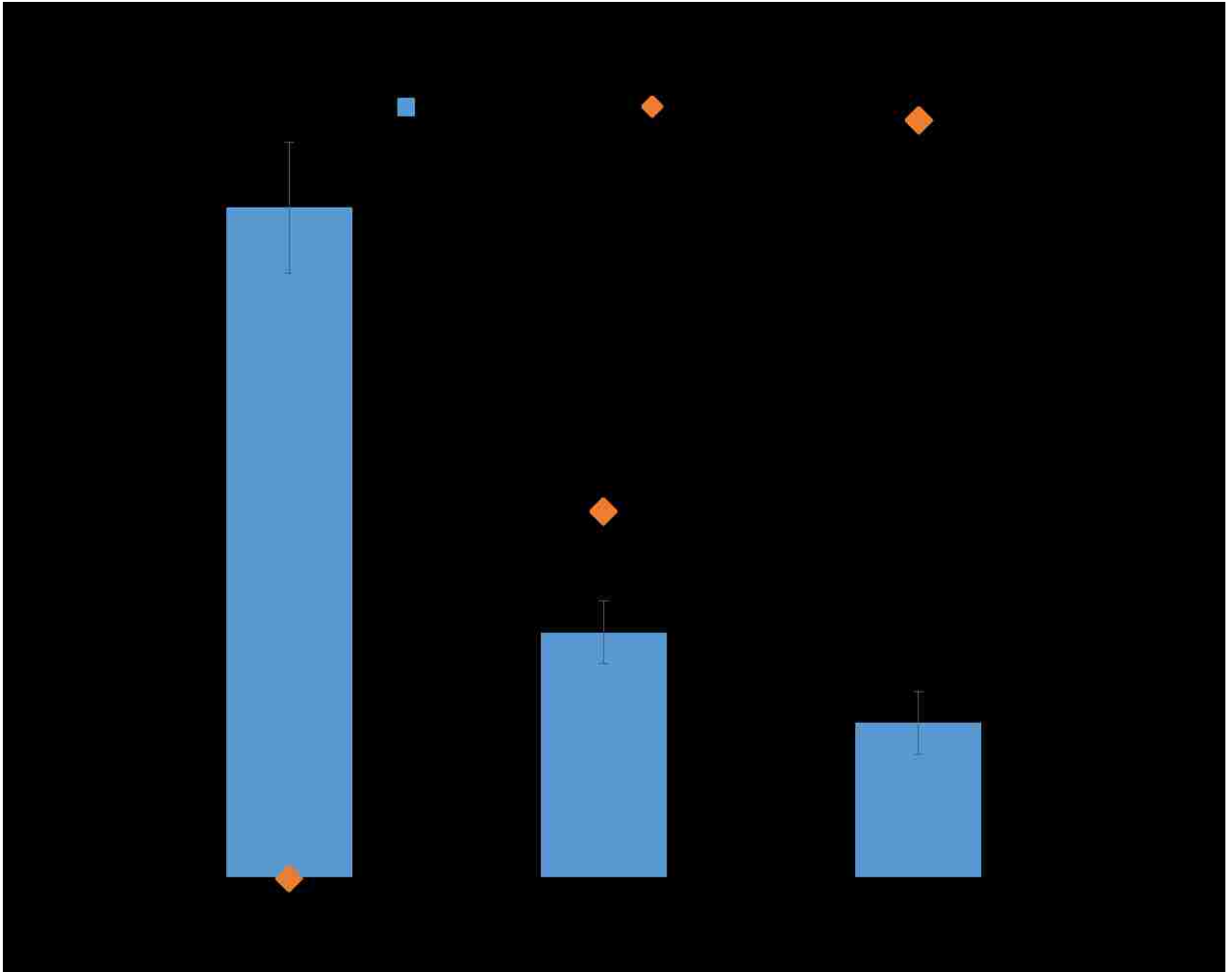


Figure 5.14. Contact angle of water (bars, left axis) and wt % GQD (diamonds, right axis) for the unmodified cellulose membrane and GQD cellulose hybrid membranes prepared using water and IPA gelation bath, respectively. All membranes soaked in IPA and air dried before testing.

The water contact angle of the cellulose membrane was significantly reduced by modification with GQD ¹⁰⁰. The contact angle that was experimentally observed for unmodified cellulose membrane corresponds to the contact angle reported for Avicel PH-101 microcrystalline cellulose ^{131,132}. The contact angle of water was observed to decrease with increasing dose of GQD within the membrane. This is attributable to the functional groups present in GQD such as carboxylic and hydroxyl. The addition of GQD makes

membrane more hydrophilic. Overall, the results of zeta potential and contact angle measurements provide compelling evidences that GQD are present on the membrane surface. Therefore, it is shown that the integration of GQD into the cellulose domain results in membranes with modified surface properties.

Confocal fluorescence microscopy was also used to determine presence of GQD at the surface of the GQD cellulose membranes. GQDs are highly fluorescent in nature, but this fluorescence can potentially be quenched in a constrained domain ¹³³. Therefore, thionin acetate, a positively charged dye, was convectively passed through to adsorb to carboxyl groups of GQDs, which should only be present in GQD within the membrane. This procedure was performed for GQD cellulose membranes made using water and IPA coagulation baths. An unmodified cellulose membrane was also prepared using a water coagulation bath as the control. These membranes were rinsed of any excess dye through passage of PBS buffer (pH~ 7.4). Both presence of GQD and thionin acetate were able to be probed at the membrane surface.

The confocal images in Figure 5.15, confirm that GQD are indeed present in GQD cellulose membranes as indicated by the higher color intensity. It can be seen that there is no dye present in the unmodified cellulose membrane and only background fluorescence between 525-535 nm. Furthermore, GQD cellulose membranes prepared with an IPA coagulation bath were observed to have higher fluorescence at the emission wavelengths associated with GQD. This data agrees with the contact angle data and the fact that all GQD must remain in the membrane when using an IPA coagulation bath. Furthermore, the

presence of GQD and adsorbed thionin acetate dye suggests leaching during the passage of PBS buffer to be minimal. GQD solubility within the EMIMAc solvent and hydrogen bonding with cellulose seems to play a critical role in maintaining dispersion and retention of GQDs in the membrane. As seen in Figure 5.16, GQDs were able to be dispersed into a 6:1:1.4 mass ratio of acetone, water, and cellulose acetate, but aggregation was observed in the CA membrane. Cellulose acetate contains less carboxyl groups than what is found in cellulose, but more importantly lack of interaction between acetone and GQDs leads to aggregation within the casting solution and thus inevitably in the membrane. Dark spots beneath the surface may correspond to GQD further below the surface that are unable to be excited.

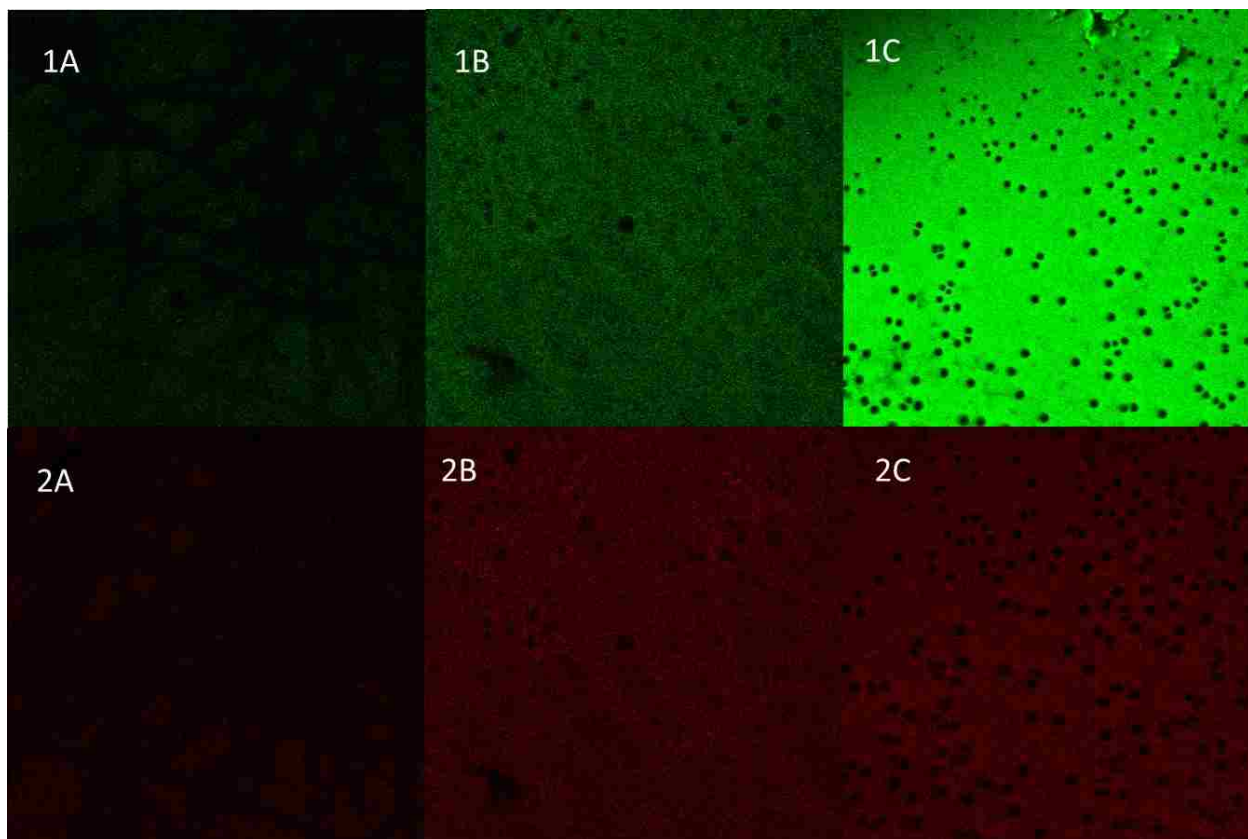


Figure 5.15. Confocal Microscopy of Membranes: A) Unmodified Cellulose. B) GQD Cellulose Water C) GQD Cellulose IPA at an excitation wavelength of 488 nm. Two regions of emission wavelengths were analyzed: 1) GQD fluorescence at 525-535. nm 2) Fluorescence of thionin acetate at 580-590 nm. Images magnified 3x. The dark spots are macrovoids in the membrane structure below the surface. The intensity increase from A to C corresponds to higher GQD loading.



Figure 5.16. *Top left insert.* a) 17 wt% Cellulose Acetate, 12 wt% water, 71 wt% acetone casting solution. b) Casting solution a) with .01 wt% GQD added. *Bottom left insert.* Resulting membranes made with solution a) and b). *Right figure.* Fluorescence microscopy (100x) of GQD cellulose membrane using 440nm light source.

5.3.7 Water Permeability

The morphology of the GQD Cellulose membrane cross-section suggests an open structure with a thin selective layer of just around 100 nm. An open structure throughout the bulk of the membrane should allow the membrane to be more permeable to water, as there is less resistance to flow throughout the depth of the membrane. Therefore, it is expected that the GQD cellulose membranes will maintain higher water permeability than the unmodified cellulose membrane at the tested pressures. The volumetric water flux as a function of pressure is shown in Figure 5.17. The flux behavior can generally be approximated as linear as pressure. However, with these cellulose based membranes compression at higher

operating pressures may cause the deviation in linear behavior. The membrane relaxes after pressure is reduced and the membrane is not permanently compressed.

ΔP is the pressure applied across the membrane and $\Delta \Pi$ is the osmotic pressure difference between feed and permeate. The, water permeability, A , is simply the slope of the volumetric flux vs. pressure in this scenario as osmotic pressure is negligible in the case of DIUF water. The nonlinear behavior of the flux at higher pressures is a result of the membrane compacting further as pressure is increased, creating a less permeable structure.

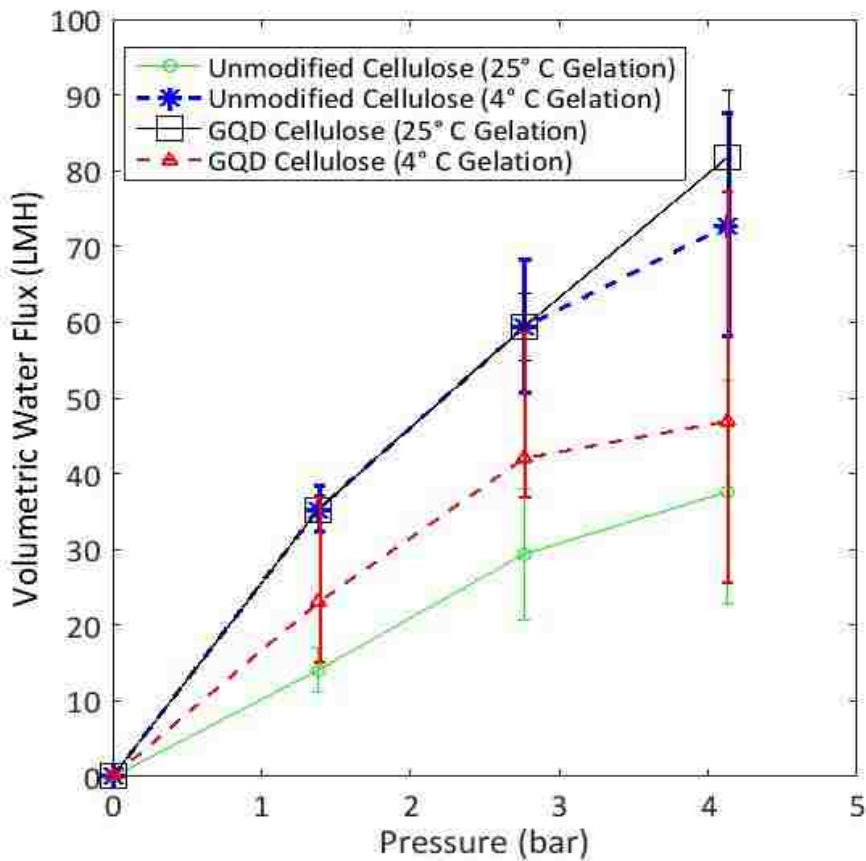


Figure 5.17. Volumetric Water Flux vs Pressure for GQD cellulose membrane as compared to unmodified cellulose membrane.

Water permeability of the GQD-cellulose membrane was nearly double the unmodified cellulose membrane using the same gelation bath temperature. The temperature of the gelation bath can be lowered to decrease pore size and create a tighter membrane. The volumetric water flux of the GQD-cellulose membrane prepared in a 4°C bath was slightly above that of unmodified cellulose membrane at 25°C. It is interesting to note that the permeability of the unmodified membrane prepared in a 4°C bath was higher than the same membrane produced in a 25°C bath. This result is opposite of what might be expected due to defects from early crystallization of cellulose at the lower temperature. The water permeability of 12.8 LMH/bar, was comparable to that previously observed for various commercial NF membranes, including DOW NF270 membrane, a membrane commonly used to remove dyes and divalent ions⁸⁸. Variations in thickness between membranes can result in different permeability. This variation appears to be greater at higher pressure, where greater compaction of the membrane happens.

GQD cellulose membrane permeability showed only 7% average variation over 4 hours of permeation of DIUF water and dye solution at 1.4 bar. This long-term flux behavior can be seen in Figure 5.22. No fouling was observed to occur from the 5kDa blue dextran being permeated through the membrane.

5.3.8 Rejection of Model Dye

Model dye solutions were passed through the membrane to determine pore size of the selective layer of the membrane, and demonstrate the membrane ability to selectively reject small molecules between 300 to 5000 Da. The rejection of model dye was measured using UV Vis. Larger dyes, namely 10,000 Da and 500,000 Da blue dextran, were tested to determine if there were any larger pores or defects in the membrane. DIUF water was

passed through the membranes before testing rejection, therefore if any GQD leaching were to occur, it would have occurred before rejection was tested. The rejection behavior can be seen in Figure 5.18. Rejection of NaSO_4 (100 mg/L solution) for all membranes was tested and determined to be insignificant. The difference in rejection of 5000 Da blue dextran between the GQD cellulose and unmodified cellulose membranes cast at 25°C is within the margin of error for the experiment. The GQD cellulose membrane was far more permeable than the unmodified membrane, but the rejection of blue dextran was observed to level off at MW of 5000 Da. Thus at 25°C presence of GQD contributed to more open membrane structure with greater pore size and presence of pores large enough to enable some passage of 500 kDa blue dextran. The rejection of methylene blue was 0% as compared to 33.4% for the unmodified membrane. The significance of the larger pore size depends on what molecules are to be targeted for rejection, and what other molecules are present in the feed water to be passed through the membrane. The membrane is highly selective for rejecting larger molecules around 5000 Da over smaller molecules and salts. However, the separation of molecules of MW larger than 5000 is less efficient due to the plateauing of rejection. GQD Cellulose membrane rejection was observed to remain stable even after 3 hours of permeation, as seen in Figure 5.23.

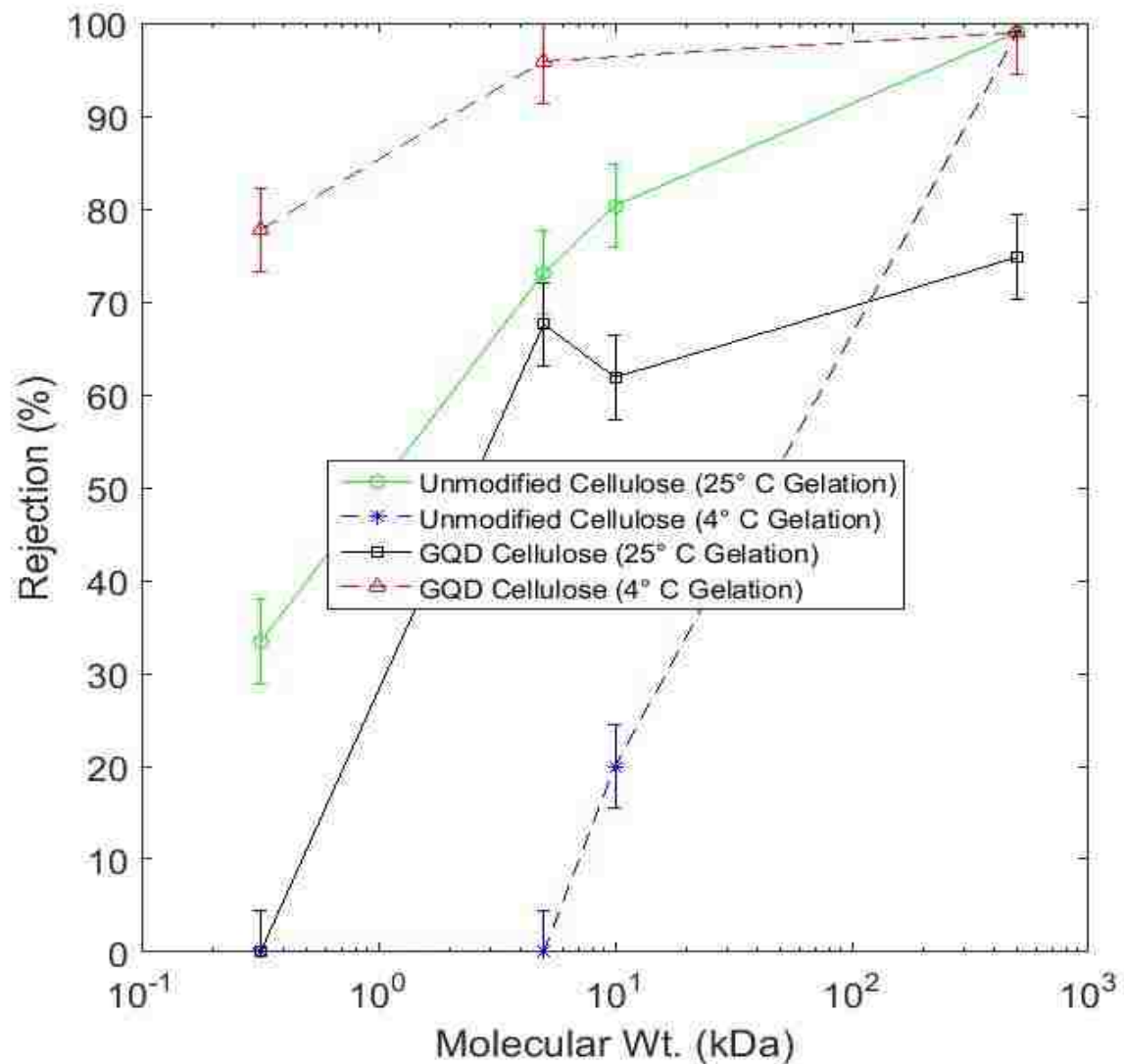


Figure 5.18. Rejection of model solute through selected membranes. Experiments performed @ 1.37 bar using Blue Dextran (1000 ppm) and Methylene Blue

While there are many parameters that effect membrane pore size, adjusting membrane temperature during phase inversion can result in a tighter membrane structure¹³⁴. Reducing temperature in the unmodified cellulose casting solution repeatedly resulted in a defects in the membrane surface. These defects were observed by abnormally high volumetric flux, as mentioned previously, and retention of any of the model dye solution was negligible. GQD presence was observed to prevent these defects. Lowering phase

inversion temperature to 4°C when GQDs were present in the casting solution resulted in a successful membrane, and better rejection of smaller molecules. Rejection of methylene blue increased to 80%, and rejection of 5000 Da blue dextran is 95.9% for the GQD cellulose membrane cast at lower temperatures. Dye sorption did not play a major role in methylene blue rejection. More details regarding dye sorption are found in Figure 5.21. As the rejection of 500,000 Da blue dextran was over 99%, defects in the selective layer were also reduced. The presence of GQD should serve to tether the cellulose and prevent premature gel formation that may cause defects seen in a cold gelation bath for the cellulose-ionic liquid solution. The GQD cellulose membrane made using a cold gelation bath is an excellent candidate for selectively removing high-value molecules from smaller byproducts such as salts, which were observed to pass through the membrane.

Table 5.1 summarizes the performances of the membranes tested in this work in comparison with other cellulose membranes in literature made using an ionic liquid casting solution.

Table 5.1- Cellulose Ionic Liquid Membrane Performance

Membrane	Wt% Cellulose	Wt% GQD	Wt% EMIMA c	Gelation Temp (°C)	Membrane Thickness (µm)	Pure Water Permeability (LMH/bar)	MWC O (kDa)
Unmodified Cellulose	10	0	90	25	150	9.6	500*
GQD Cellulose	10	0.05	90	25	150	20	>500*
GQD Cellulose Cold	10	0.05	90	4	150	12.8	5*
Livazovic 5% ^{115**}	5	0	95	23	3.5	11.4	46
Livazovic 10% [27]**	10	0	90	23	6.8	1.2	5
Durmaz 1 ^{135**}	8	0	92	25	250	~20	20*

* MWCO obtained by taking lowest MW compound rejected above 90%

** Membranes from other authors' work cited in brackets.

This information seen in Table 5.1 seems to indicate that permeability of cellulose membranes is not dependent on membrane thickness. Furthermore, MWCO seems to vary, but higher wt% of cellulose is expected to reduce the MWCO of the membrane.

5.3.8 GQD Retention Post-Coagulation

Previously discussed experiments provide evidence against significant long-term leaching of GQD from the membrane. GQD cellulose membrane charge was not observed to diminish over time during zeta potential measurement in the electrokinetic analyzer. Therefor no GQDs were observed to leach after continuous exposure to high shear flow across the membrane surface and through the membrane cross-section. Additionally, GQDs were still found to be present in confocal fluorescence imaging in GQD cellulose membranes after convective passage of 50 mL of dye solution and over 200 mL of PBS buffer solution. Short term leaching was studied by permeating a small volume water through a newly cast membrane following 30 min of coagulation in a water bath. Observing the UV absorbance of the first 10mL permeated out of the membrane, can be seen in Figure 5.19.

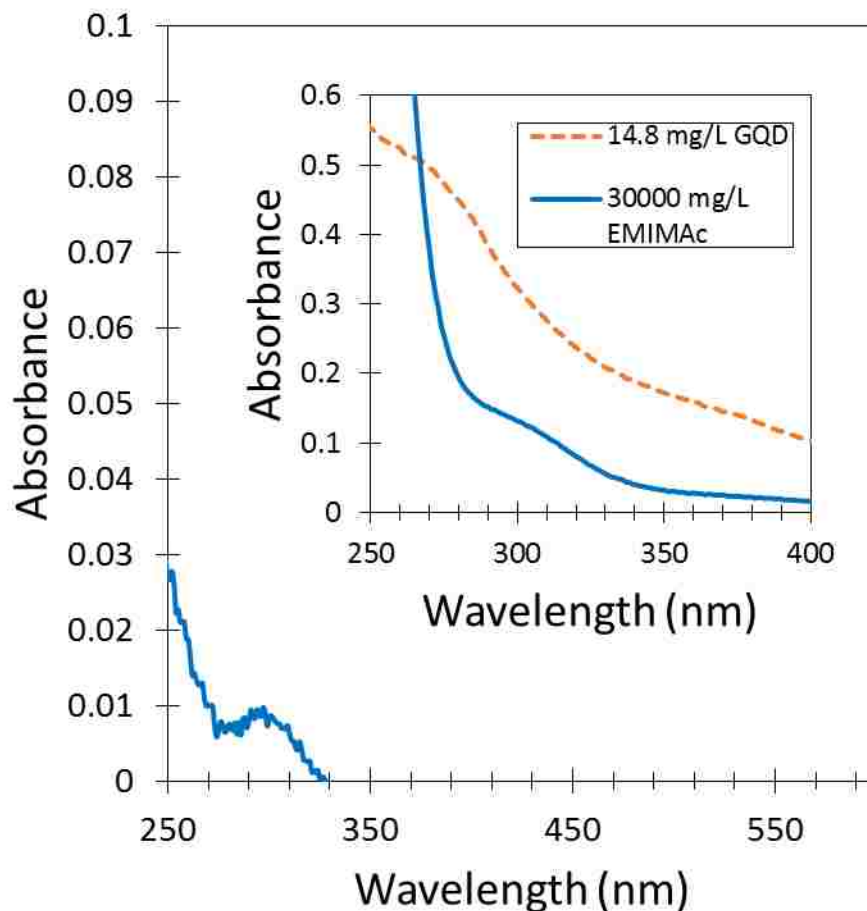


Figure 5.19 UV-Vis absorbance of permeate solution through the GQD cellulose membrane (25°C water gelation) 10mL of DIUF permeated through the membrane at 1.4 bar. *Figure insert:* UV-Vis absorbance of known concentrations of GQD in DIUF and EMIMAc in DIUF respectively.

The UV absorbance around 300 nm was only seen to be 3.3% of the GQD standard solution. The standard solution concentration for GQD was carefully chosen to represent complete leaching of all GQD in the first 5mL of DIUF water permeated. The peak in absorbance of the permeate at 300nm seems to indicate the presence of EMIMAc presence rather than GQD as seen by the peak in absorbance for the ionic liquid standard in the figure insert. Figure 5.20 shows that initial permeation results in passage of ionic liquid retained in the membrane during coagulation, which quickly stabilized toward an average

baseline absorbance of 0.01. Therefore, no significant leaching of GQD is expected in both short-term and long-term membrane use.

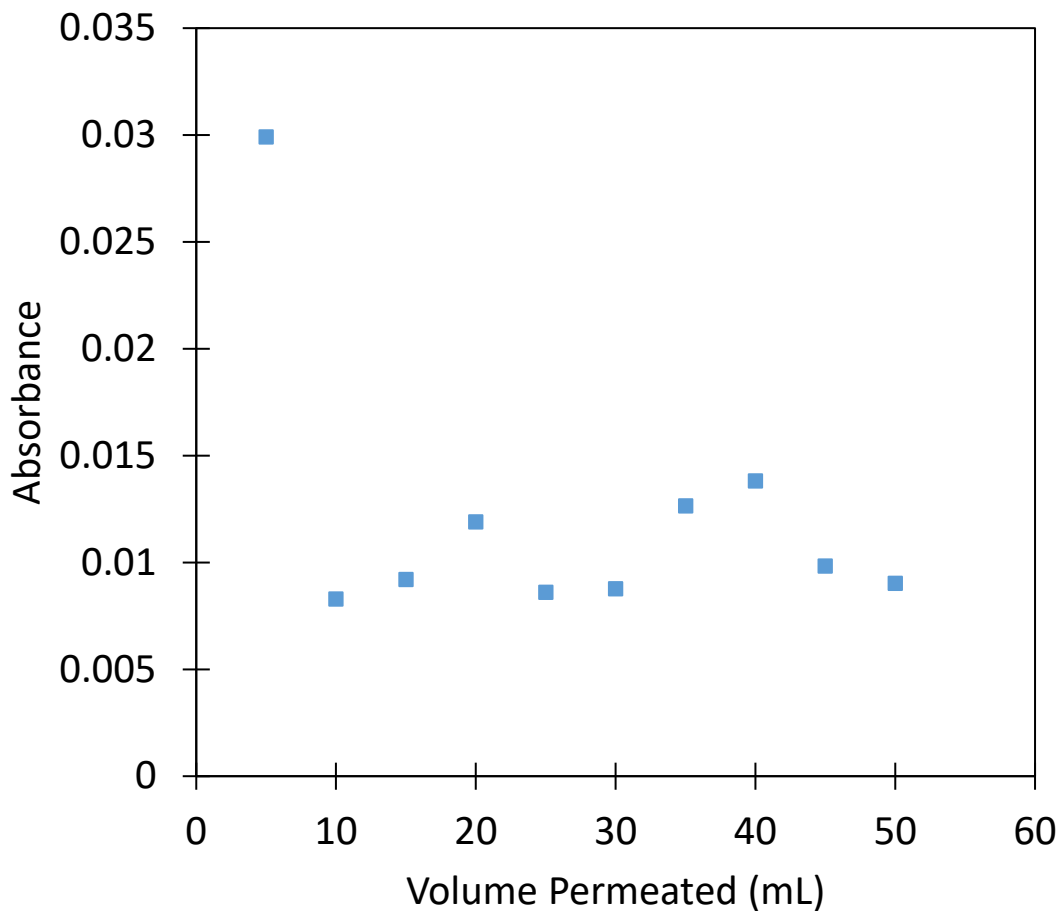


Figure 5.20 Measurement of ionic liquid absorbance at 300 nm vs. volume permeated through GQD cellulose membrane (25°C water gelation). Pressure 1.4 bar.

5.3.9 Methylene Sorption in Membranes

In convective flow experiments, the volume collected was relatively small compared to the 300 mL loaded into the pressure cell. Therefore, retentate absorbance was

not found to vary significantly from the feed absorbance for methylene blue. Therefore, a separate sorption study was required. Unmodified cellulose and GQD cellulose membranes (16 cm² of each) were placed into 20mL of 10 mg/L methylene blue solution. The membranes were left on a shaker for 24 hours to allow adequate time for sorption. Though the surface layer is dense, the backside and cross section of the membrane are more open and should be accessible for methylene blue to adsorb to the surface of the cellulose. Analysis of the methylene blue solution before and after sorption suggested some possibility for sorption of methylene blue into the membranes. UV-Vis studies suggest cellulose membrane adsorbed 150 µg of methylene blue and the GQD cellulose adsorbed 160 µg. This can be seen in Table 5.2.

Table 5.2- Methylene Blue Sorption in Membranes

Membrane	Solution Concentration after Sorption (mg/L)	% Absorbed
Unmodified Cellulose	7.65	23.5%
GQD Cellulose	8.30	17.0%

However, after just 30 min of rinsing in water the membranes had lost all blue color, which suggest there is no strong adsorption within the membrane, but perhaps partitioning effects. As shown in Figure 5.21, the only membrane to retain color after rinsing is the GQD cellulose membrane that has had blue dextran convectively passed through it. This effect is also to be expected for methylene blue. This data suggests that accessibility of the membrane pore network is not a major factor in dye sorption, but rather pressure assisted flow of dyes, lead to physical entrapment within the membranes pores and surface adsorption.

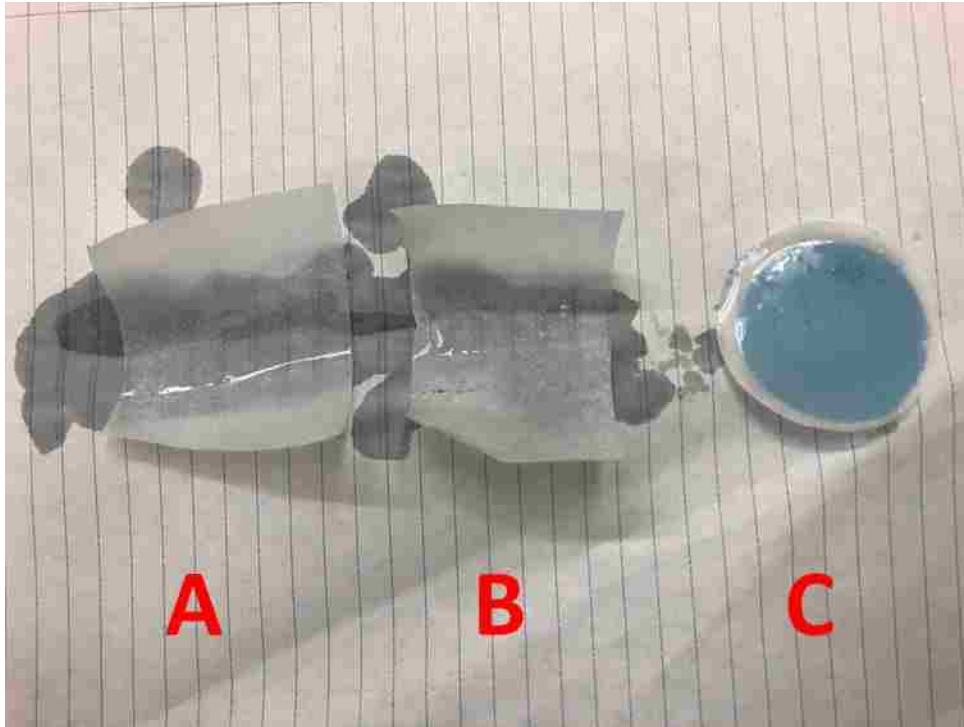


Figure 5.21 Unmodified Cellulose (A) and GQD Cellulose (B) membranes after soaking in 10 mg/L methylene blue solution for 24 hours and being rinsed for 30 min. GQD cellulose membrane (C) after passage of 300 mL of 100 mg/L 5kDa Blue Dextran solution included as reference.

5.3.10 Long Term Study

To test GQD cellulose (25°C water gelation) membrane stability over long term operation a convective flow test of 4 hours was set up. During the first hour DIUF was passed through the membrane to ensure stabilized volumetric flux. Precompaction occurs during this step. After DIUF passage, 1000 mg/L 5 kDa Blue Dextran was passed through the membrane over the course of 4 separate tests. The water flux of the membrane was stable over the course of testing as can be seen in Figure 5.22.

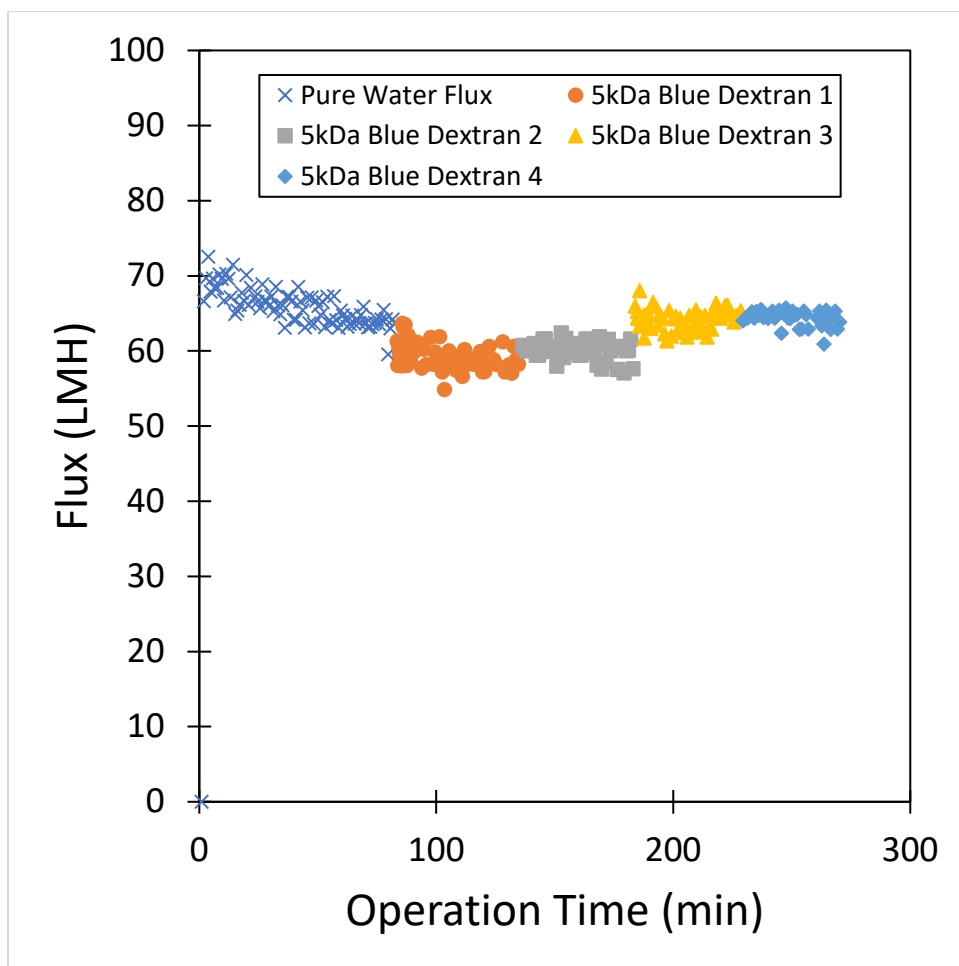


Figure 5.22 Long term study of water flux through GQD cellulose membrane (25°C water gelation) at an operating pressure of 1.38 bar.

The permeate was analyzed at the end of each permeation cycle of blue dextran. Using UV-Vis the rejection could be calculated for each cycle. The stability of Blue Dextran rejection can be seen in Figure 5.23.

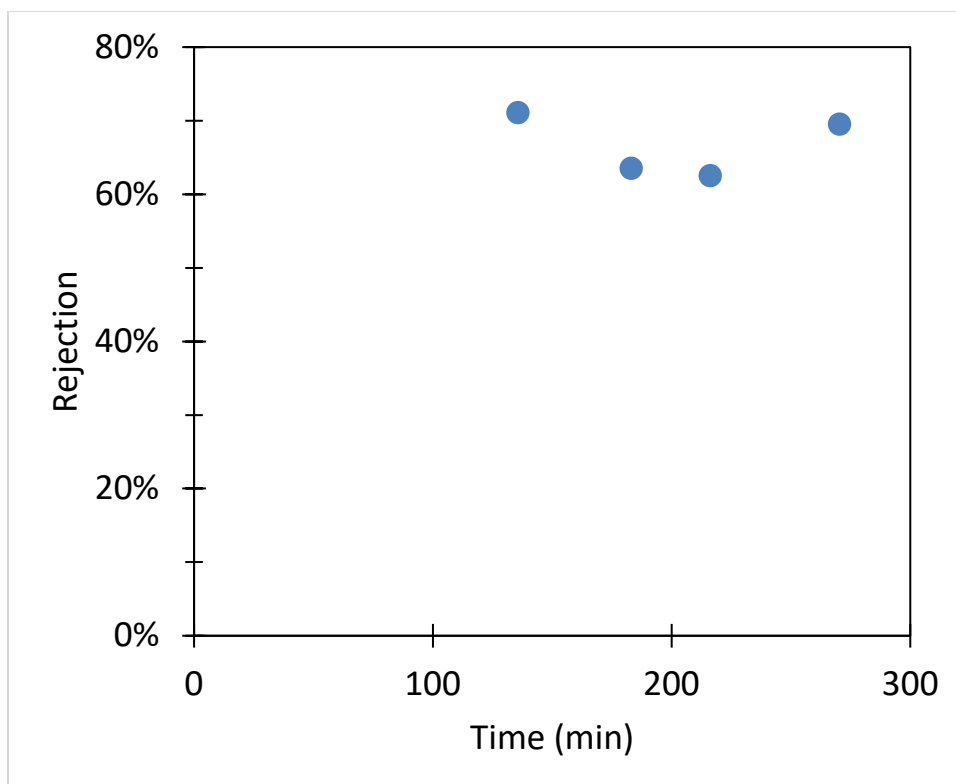


Figure 5.23 Rejection of 5kDa Blue Dextran by GQD cellulose (25°C Water Gelation) during long-term permeation study.

Neither permeability nor rejection significantly degrade during the duration of testing. Therefore, the GQD Cellulose membrane is shown to be stable over longer periods of operation. This behavior should be similar for all membranes studied in this experiment.

5.4 Conclusion

This work demonstrates the fabrication of a composite membrane of GQD and cellulose where GQDs are homogeneously incorporated into a cellulose membrane network through a strong hydrogen bonding using a common ionic liquid. The incorporation of GQDs has a profound impact on the membrane structure and performance. GQDs formed strong interactions with the dissolved cellulose in the membrane casting solutions, as indicated by the greatly increased viscosity. The quantity of GQD concentration in the water nonsolvent

during phase inversion indicated that 45% (0.2 wt% of the membrane) of the GQD remained in the membrane domain after phase inversion. GQDs were determined to be present on the surface while making the membrane negatively charged and more hydrophilic. Thus, it can be inferred that the unique properties of GQD can be used during water separation, as the GQD are accessible to the solution being passed through the membrane. GQDs were shown to act as pore formers, as GQD cellulose membranes were observed to have a much more open structure, indicated by cross-sectional imaging and the higher water permeability. GQDs prevented crystallization of cellulose upon immersion low-temperature gelation baths, which resulted in defects in the control membrane. Therefore, gelation temperature of the GQD cellulose membrane can be modified to tune rejection of small molecules. There was no evidence of GQD leaching during convective flow of water through the membrane. Strong interaction of GQD with cellulose hydroxyl groups ensures membrane stability and consistent performance overextended time.

CHAPTER 6. FURTHER ADVANCEMENTS IN CELLULOSE COMPOSITE MEMBRANES AND LIGNIN FUNCTIONALIZED NANOFILTRATION MEMBRANES

6.1 Introduction

Cellulose is the most abundant biopolymer on the earth. In plants cellulose makes up most of the cell wall, providing structural support. Cellulose within the cell wall of plants arranges itself in a mesoporous structure to sterically prevent enzymatic decomposition¹³⁶. The use as a membrane-like material arguably began when humans first began making textiles out of cotton and flax. Cellulose remains an effective material for physical size-based separations of particulates¹³⁷. Beyond particle separation, the polymer network of cellulose materials has been investigated for separations of smaller organic molecules. Transport of solutes through cellulose membranes has long since been of interest in the scientific community. Dating back to the 1950s high class studies of hindered diffusion of small organic molecules in aqueous solution through cellulose materials such as cellophane and sausage casings were studied⁵⁰. Cellulose derived polymers such as cellulose acetate have been widely used for membrane making, but the modification required to enhance solubility in commercial solvents reduces robustness of membrane for filtration of organic solvents¹³⁸.

The strong hydrogen bonding in cellulose poses challenges for dissolution and materials processing. Regeneration of cellulose with solvents such as N-methylmorpholine-N-oxide or basic conditions is being implemented to create selective membranes^{111, 139, 140}. Ionic liquids are being investigated as a new solvent for regeneration of cellulose for membrane synthesis^{141, 142}. Membranes utilizing ionic liquid as a solvent show performance in the ultrafiltration to nanofiltration. This same ionic liquid approach

was used to spin cellulose hollow fibers¹⁴³. Cellulose membranes prepared using ionic liquid have been shown to be highly selective for particular dyes, rejecting 94% of Bromothymol Blue¹¹⁷.

Addition of composite materials such as graphene into cellulose is one approach to create new materials for energy and separation applications¹⁴⁴⁻¹⁴⁶. By tuning the polymer chemistry in membranes, creation of highly selective membrane structures can be designed. Block copolymers alternate hydrophilic and hydrophobic structures to create finely tuned pores due to polymer chain alignment¹⁴⁷. Instead of using polymer chemistry to create negative space or pores of precise size, composite materials can hydrogen bond within polymer networks, such as that of cellulose to make the polymer layers more selective.

The objective in this work was to further expand on our previous research studying cellulose GOQD membranes into other composite materials to further improve membrane performance and demonstrate flexibility of this technique for membrane development. Iron (III), polyacrylic acid, and lignin sulfonate were all investigated as composite materials for integration within the cellulose membrane domain. Membrane permeability and selectivity was studied for each composite type, along with useful properties unique to each composite material. These properties include antibacterial behavior and solvent dependent tunability of permeability and selectivity.

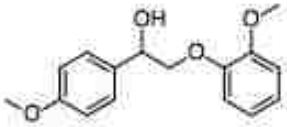

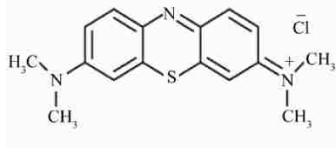
6.2 Experimental

6.2.1 Materials

1-ethyl-3-methylimidazolium acetate (EMIMAc, HPLC grade) was purchased from Sigma Aldrich. Avicel® PH-101 microcrystalline cellulose (50µm, cotton linter source) was purchased from Sigma Aldrich. Nonwoven polyester backing material from

Nanostone was used as a support for membrane formation. Blue dextran (MW: 5000 Da; 10,000 Da) were purchased from Sigma Aldrich for use in membrane pore size characterization. Solutes used in selectivity studies can be seen in Table 6.1. Methylene Blue and Neutral Red (Sigma Aldrich) were used as model dyes to study rejection of molecules <1000 Da. A β -O-4 Model Dimer provided by Dr. Mark Crocker's lab in the Center for Applied Energy Research. Ferric Iron Chloride (Fisher) was used as an Iron (III) source in composite membrane synthesis. Lignosulfonic Acid Sodium Salt was purchased from Beantown Chemical LLC. as a lignin sulfonate source.

Table 6.1 Solute dyes tested for rejection.

Model Solute	Molecular Wt. (Da)	Structure
β -O-4 Model Dimer	282	
Neutral Red	289	
Methylene Blue	320	

6.2.2 Cellulose Composite Membranes

Three types of Cellulose composite membranes were studied: cellulose iron, cellulose PAA, and cellulose lignin sulfonate composite membranes. A summary of the

composition of the various membranes can be seen in Table 6.1. Control membranes of 10 wt% cellulose were also studied. All membranes were created using 1-ethyl-3-methylimidazolium as a solvent. The desired amount of composite material was dispersed into the ionic liquid at 80°C for one hour. This is to ensure full dispersion of the composite material in the ionic liquid before dissolution of cellulose increases the casting solution viscosity. After composite material dispersion, 5-10 wt% cellulose was added into the casting solution and physically mixed in then dissolved at 80°C for 8 to 24 hours until the cellulose was completely dissolved.

. Membranes were cast on nonwoven fiber backing. Polyester support material was affixed to a glass plate using tape. The casting solution was poured directly onto the backing at 80°C and cast directly onto the polyester backing using a doctor blade set to 150 µm. The polyester backing was then submerged in a water or isopropanol gelation bath for 10 minutes to allow time for membrane formation. The resulting membrane was stored in DI water at a temperature of 4°C until use.

6.2.3 Zeta potential characterization

Zeta potential of cellulose and GQD cellulose membranes was measured by an Anton Paar Surpass 1 electrokinetic analyzer. The adjustable gap cell was used with a 100 µm gap and 0.01 M KCl electrolyte solution. Acid titration was done with 0.01 M HCl. 400 mBar pressure difference was used for all measurements.

6.2.4 Contact angle characterization

The contact angle for deionized ultrafiltered water was measured using the Kruss DSA 100. Captive bubble method was used to determine contact angle do to water absorption in the cellulose membranes and to prevent deformation of surface structure

during drying. At least 3 spots per membrane sample were analyzed to correct for any variance in surface morphology.

6.2.5 Membrane Performance

Membrane performance was characterized by using the Sterlitech HP4750 stirred cell to perform convective studies. Water permeability was determined for each membrane by measuring the volumetric flux of DIUF at 1.4, 2.76, and 4.14 bar respectively. Methylene blue (5 mg/L) and neutral red (5 mg/L), as well as various molecular weights (5kDa and 10kD at concentrations of 100 mg/L) of Blue Dextran, were filtered through the membrane. The permeate was collected and dye concentration for the feed, permeate, and remaining retentate was analyzed using the VWR UV-6300PC Spectrophotometer.

6.2.6 Divalent Ion Capture by Cellulose-PAA Membranes

Ca²⁺ capture in cellulose PAA composite membranes was carried out without the usual exchange of Na⁺ for H⁺ as imidazolium was already expected to be exchanged for H⁺. The membrane was added to the filtration cell right away and soaked in about 110 mL of DI water that was kept at a pH of 10. After soaking, about 15 mL of fresh DI water (pH » 4.5-5.5) was passed through the membrane and the pH of the permeate was verified to be 7 or higher. For the Ca²⁺ capture, an aqueous CaCl₂•2H₂O solution (»1.79 mM, pH = 6.5-7) was prepared with non-deoxygenated, DI water and a 10-mL sample of this solution was taken. To capture Ca²⁺, about 200 mL of fresh solution was passed through the membrane in 50-mL increments using pressures mostly in the range of 0.28-0.62 bar. At the end of each increment, a 10-mL sample of the collected permeate was taken and the rest of the permeate was disposed of before continuing the filtration

Ca²⁺ captured was quantified by Inductively Coupled Plasma Optical Emission Spectroscopy (ICP-OES). Ca²⁺ captured within the membrane case measured and located using energy-dispersive X-ray spectroscopy (EDS).

6.2.7 Lignin Sulfonate Functionalized Nanofiltration Membrane

Functionalized membranes were created by utilizing a circular metal holder, an o-ring is typically found on these cells at the base to create a seal. A 10 wt% LS solution in water was poured over 40 cm² area NF-270 nanofiltration membrane. Sufficient LS solution was poured over the surface until the entire membrane was covered. This allowed for ample LS to bond to the membrane and ensured even functionalization. The entire cell block was then placed in an oven at 90°C for approximately 2 hours. After taking the membranes out of the cell, they were rinsed with copious amounts of DI water to remove residual LS that may not have bonded to the membrane. LS presence on the membrane surface can be confirmed by light brown tint on the membrane surface.

A crossflow apparatus allowed for testing the anti-fouling properties of both the functionalized and unfunctionalized membrane. The cross-flow apparatus was run at a flowrate of approximately 1.5 liters/min for both the equilibration stage, fouling stage, and tangential washing stage. Before any anti-fouling testing could be done, the membrane was precompact at 10.4 bar with deionized water to equilibrate the membrane before the fouling agent. After this equilibration period, a bovine albumin serum (BSA) solution was run through the apparatus and volume of permeate measured. After 30 minutes into the fouling stage, the membrane surface was rinsed with deionized water (pH=5.6) for 10 minutes. Na₂SO₄ (1000 mg/L Fisher Scientific) rejection was also determined in the crossflow cell at 10.4 bar.

6.2.8 Bacteria Fouling Studies

R. palustris strain CGA009 (ATCC BAA-98) was purchased from ATCC (American Type Culture Collection). Solid media cultures were isolated on tryptic soy broth agar plates. Liquid cultures were pregrown in tryptic soy broth purchased from Criterion, which contains (g L^{-1}) casein peptone, 17; soy peptone, 3; NaCl, 5; K_2HPO_4 , 2.5; Dextrose, 2.5. Pregrown liquid cultures were concentrated by centrifugation at 2500rp for 5 minutes and washed 3 times with minimal media to use as an inoculant.

R. palustris adhered to membranes were grown using a modified minimal media¹⁴⁸ that contained (g L^{-1}) Na_2HPO_4 , 6.8; KH_2PO_4 , 2.9; NaCl, 1.3; $\text{MgSO}_4 \cdot 7\text{H}_2\text{O}$, 0.4; $\text{CaCl}_2 \cdot 2\text{H}_2\text{O}$, 0.075; Thiamine hydrochloride 0.001. Trace elements were provided by adding 10 mL L^{-1} of a solution containing (g L^{-1}) $\text{FeCl}_3 \cdot 6\text{H}_2\text{O}$, 1.66; ZnCl_2 , 0.17; MnCl_2 , 0.06; $\text{CoCl}_2 \cdot 6\text{H}_2\text{O}$, 0.06; $\text{CuCl}_2 \cdot 2\text{H}_2\text{O}$, 0.04; $\text{CaCl}_2 \cdot 2\text{H}_2\text{O}$, 0.73; and $\text{Na}_2\text{MoO}_4 \cdot 2\text{H}_2\text{O}$, 0.06. Sodium glutamate (3.5-7 mM) and acetate (70 mM) were utilized as primary nitrogen and carbon sources.

Solutions of minimal media were diluted 1:10 with phosphate buffer (pH~7.2) for inoculation on the membrane surface. Inoculation of cellulose membranes was carried out by convectively passing 15 mL of the diluted media through the membrane at 1.4 bar in a stirred membrane cell. After inoculation the membranes were removed from the cell and submerged in minimal growth media in the absence of light for 10 days to allow some time for bacterial growth. The overall goal was to simulate bacteria deposition and growth on the membrane surface over long-term operation.

Bacteria adhered membranes were chemically fixed¹⁴⁹ prior to critical point drying by dosing growth media containing an inoculated membrane with glutaraldehyde (50% from) to bring the solution to 2.5% glutaraldehyde, and left to sit for 2h at 25 °C. The media

was replaced by slowly replaced with ethanol by removing media and adding ethanol to bring the ethanol concentration up to 25%, 50%, 75%, 85%, 96%, leaving the solution to sit for 1 hour between adding ethanol.

6.3 Results and Discussion

6.3.1 Summary of Membranes

A summary of composite membrane compositions and properties is given in 6.2. Permeability of all composite membrane was shown to be improved over unmodified cellulose membranes. Iron was the only composite material demonstrated to improve the selectivity of cellulose membranes for small molecules. There are many factors that impact membrane selectivity, only a few of which this work will address, but casting viscosity and wt% may be one property which can be better optimized to improve membrane performance. The focus on this work is to highlight the possibilities of incorporating composite materials into cellulose membranes and the unique benefits composite materials bring to membrane performance.

Table 6.2 Composite membranes studied with compositions and relevant properties.

Composite	Wt% Composite	Wt% Cellulose	Casting Solution Viscosity (Pa*s)	Water Permeability (pH=7)	Rejection (%) 5kDa Blue Dextran
Iron	4	5	6.8	17.4	>99
PAA	2	5	44	267	44
Lignin	5	10	96	17.5	59
---	0	10	22.8	9.6	75

6.3.2 Iron Cellulose Composite Membranes

Iron was readily incorporated as a composite material into the cellulose membrane domain, as FeCl_3 is highly dispersible in ionic liquids¹⁵⁰. Iron is well known to interact strongly with cellulose and bind to cellulose chains¹⁵¹. This interaction along with steric effects ensure iron is retained within the membrane structure after phase inversion. A clear sign of the presence of iron within the membrane can be seen by the orange color the iron brings to the normally translucent cellulose membrane. This can be seen in Figure 6.1. This effect has also been observed in our prior studies with graphene oxide quantum dots as nanocomposites.



Figure 6.1. Unmodified cellulose, GQD cellulose, and iron cellulose composite membranes.

While uses of iron in composite materials and membrane platforms is well known, the main interest in this work was to understand if iron interaction with cellulose in the membrane effects selectivity behavior of the membrane. Previous study of cellulose composite membranes has suggested that selectivity behavior is largely due to a dense amorphous polymer layer that comprises the top 100-200 nm of the membrane. To better understand how iron and cellulose might be interact in the amorphous selective layer, the

pressure dependent flux behavior of the membrane was studied in water and IPA solvents. Seen in Figure 6.2, water and isopropanol permeability behavior is unique when compared to expected behavior for cellulose based membranes. Water flux plateaued off at higher pressures, as previously observed in our studies of GQD cellulose composite membranes. Permeability of the iron cellulose membranes was within standard deviation of previously studied cellulose membranes, despite the iron cellulose composite membrane having half the amount of cellulose. It is important to note that the 5 mg/L neutral red solution was passed through the membrane after IPA passage, demonstrating that the flux response is reversible with solvent exchange.

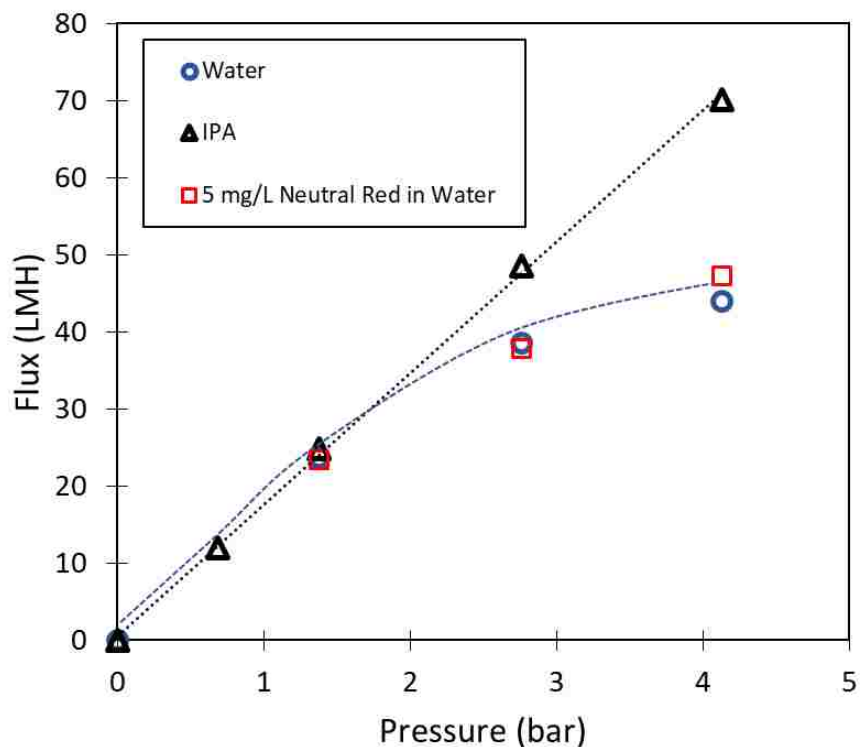


Figure 6.2. Flux (LMH) vs Pressure (bar) behavior for iron cellulose composite membranes in water, isopropanol (IPA), and neutral red in water.

Further investigation of pressure dependent isopropanol flux gave unexpected results. Despite the viscosity of IPA being roughly double that of water, the permeability remains the same. Isopropanol permeability had previously been studied in cellulose membranes as seen in Figure 6.3 to observe the effect of the polar solvent on membrane stability. When corrected for viscosity, isopropanol and water flux behavior line up are aligned. This strongly suggests the membrane surface does not swell when in contact with isopropanol. IPA flux was higher than what would be expected when observing water permeability. This suggests that the membrane becomes more permeable when exposed to isopropanol. This behavior was also found to be reversible, as water flux behavior did not change after IPA passage.

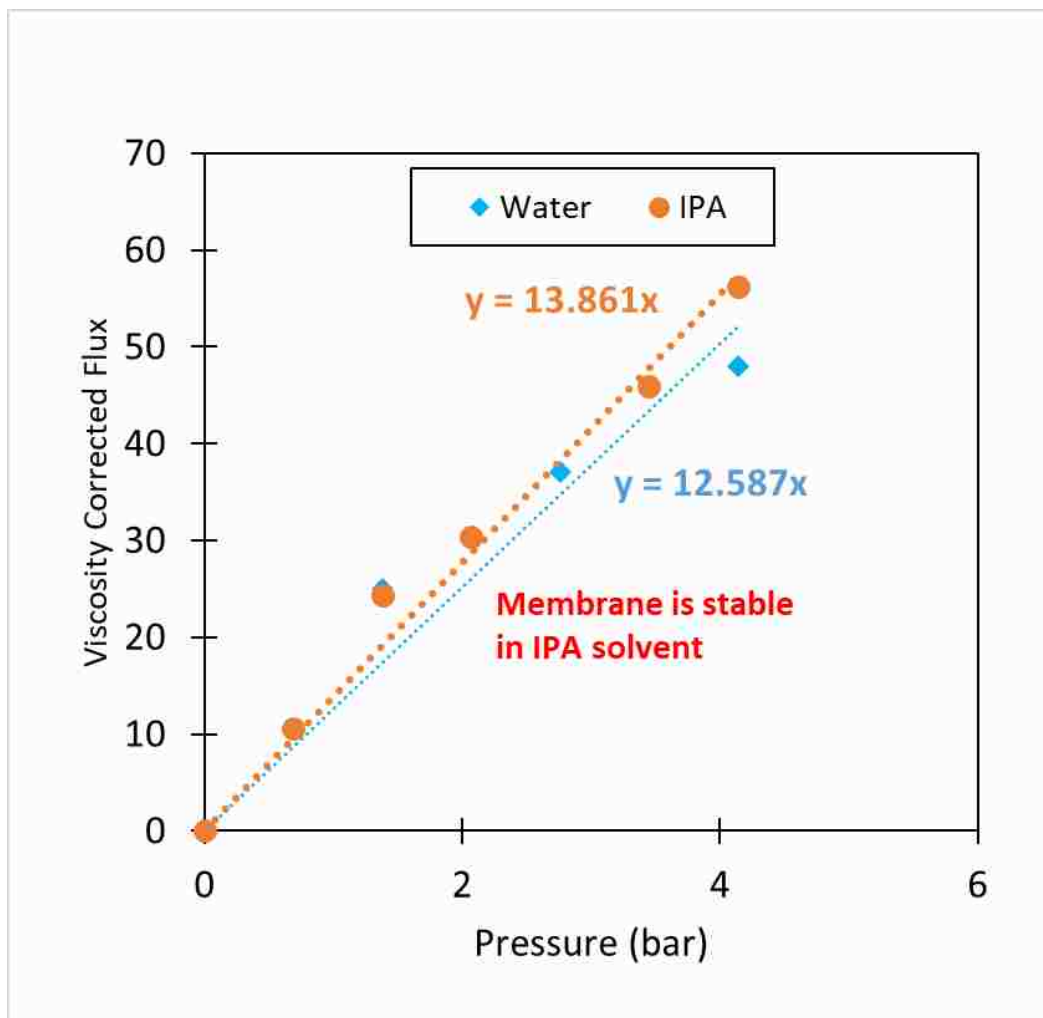


Figure 6.3. Viscosity Corrected Flux vs. Pressure for unmodified cellulose membrane (10 wt. %)

Interestingly water permeability decreased when solvent mixtures of 25:75 and 50:50 isopropanol: water. The permeability at different solvent concentrations can be seen in Figure 6.4. Strong water interaction within the cellulose domain may provide a barrier for isopropanol diffusion into the membrane domain. Mao et al. has observed that flux through cellulose membranes decreases as isopropanol concentration increases during pervaporation operation¹⁴⁰. At 100% isopropanol the inability of iron to be ionized may reduce interaction between iron and cellulose, causing the opening of the selective layer of the membrane. When the membrane is rehydrated, iron becomes ionized again and the

selective layer becomes less open. A pressure driven liquid system can exploit the openness of the selective domain. This behavior could be of great interest for applications of membrane cleaning or desorption of contaminants from the membrane surface.

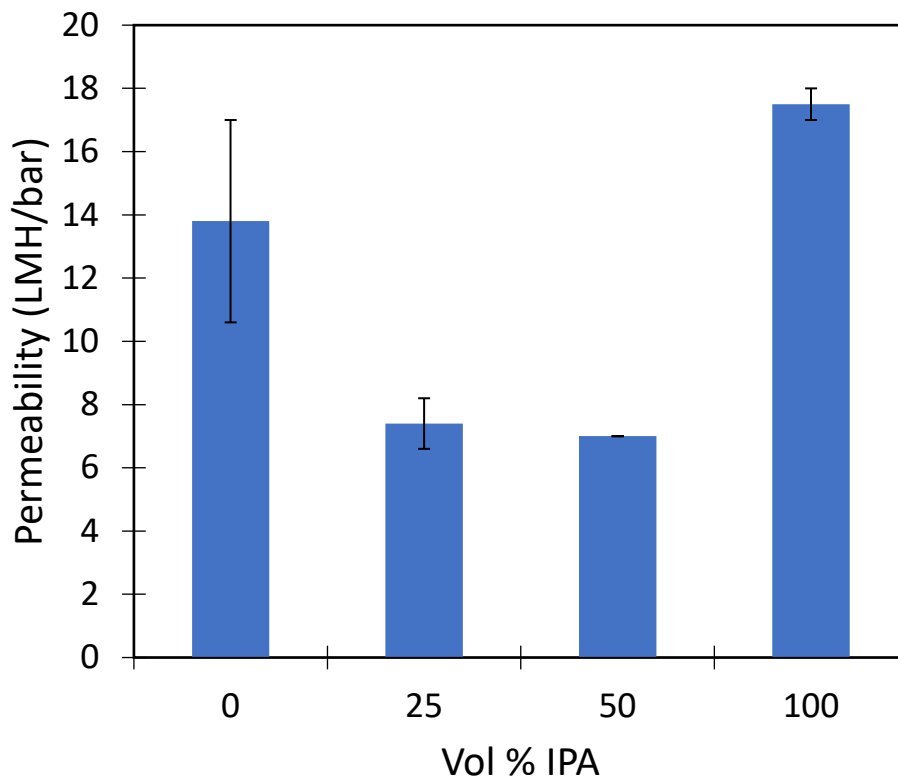


Figure 6.4. Volumetric permeability of total solvent mixture as volume % of isopropanol is varied in iron cellulose composite membranes. Remaining volume % water.

Neutral red (~289 Da) and methylene blue (~320 Da) were completely rejected (>99%) during filtration through the membrane using DI water as a solvent. As seen in Figure 6.5 rejection decreased in isopropanol which is to be expected due as hydrophilic interaction decreases in isopropanol. The increase of membrane permeability suggests the dense selective layer becomes more permeable.

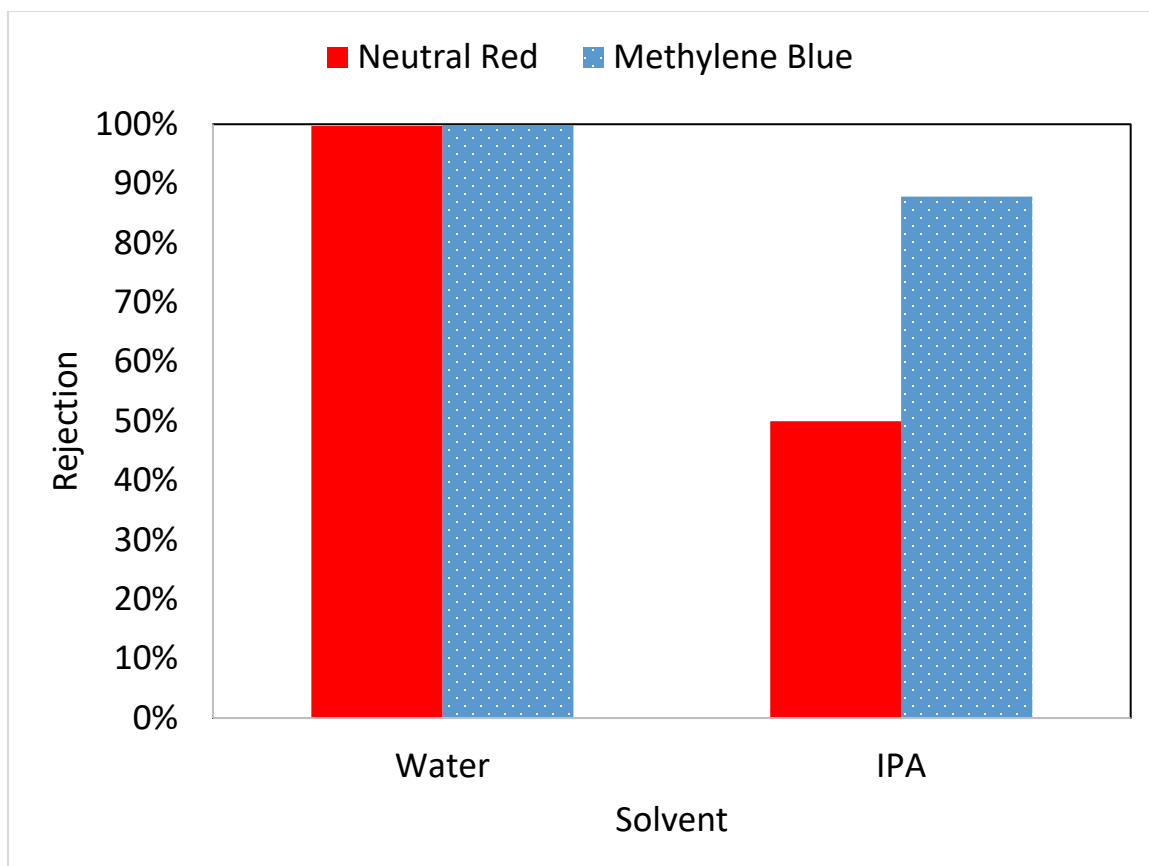


Figure 6.5. Dye rejection in iron cellulose composite membrane in water and isopropanol solvent.

Rejection studies with model dyes also suggests other factors contribute to solute selectivity other than size exclusion. Selectivity vs. molecular weight for small model molecules is show in Figure 6.6. Rejection of β -O-4 Model Dimer was only 10% despite the MW only being 7 Da less than neutral red. The disparity in rejection can be attributed to interaction among the hydrophilic functional groups. The positive dipoles of the amine groups in the dyes interacts more strongly with negative dipoles of hydroxy groups in cellulose reducing rate of diffusion of the dyes through the membrane. Carboxyl groups in the model dimer do not react as strongly. Rotation freedom in the model dimer may also allow for the dimer to change confirmation as it moves through the membrane, thus increasing diffusion rate. Ring structures in the model dyes prevent rotation within dyes as

the move into the membrane domain. Interaction among functional groups and molecular structure must be considered when evaluating possible application of nanofiltration for small molecule separation.

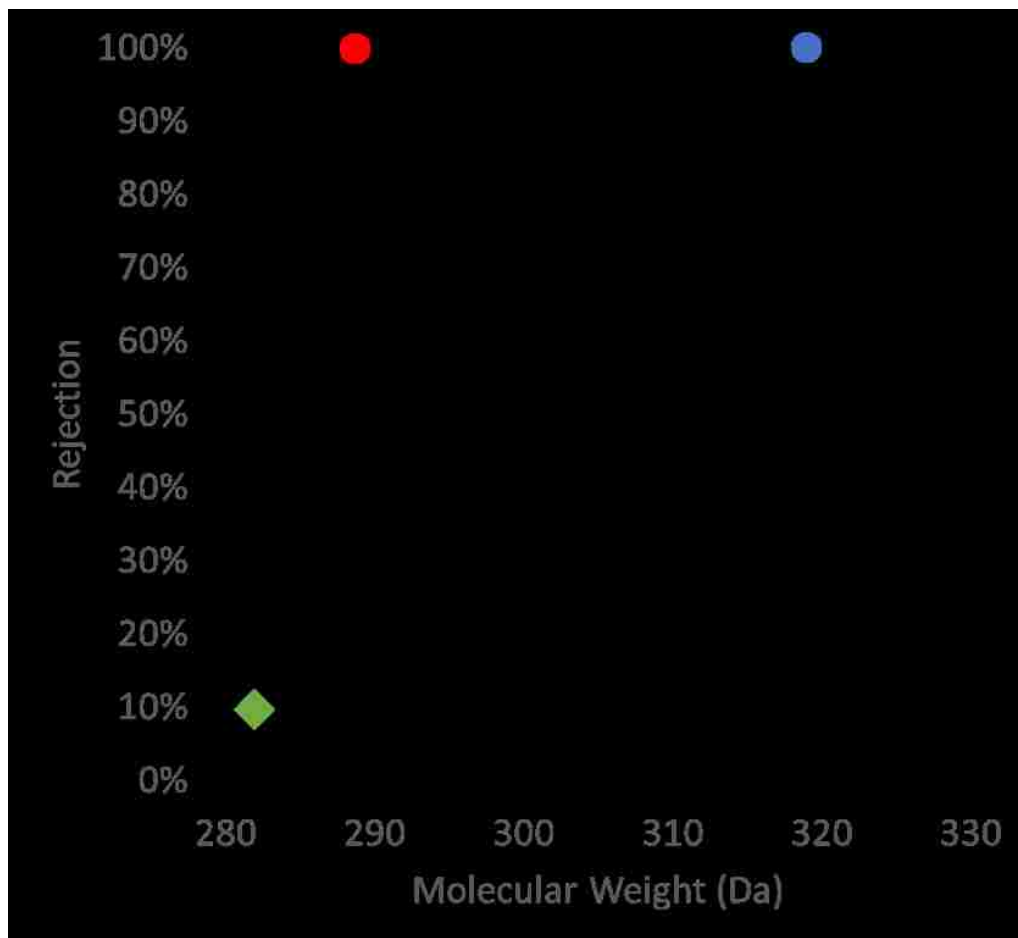


Figure 6.6. Rejection of model dyes and molecules in Iron Cellulose composite membranes.

6.3.3 Poly Acrylic Acid Cellulose Composite Membranes

Polyacrylic acid (PAA) has many negatively charged carboxyl groups which can be utilized for pH responsive behavior, metal capture, and rejection of negatively charged ions. PAA disperses fully in the ionic liquid solvent allowing even mixing with cellulose. Entanglement with cellulose chains and hydrogen bonding with cellulose allow for the retention of PAA after phase inversion. The pKa of carboxyl groups was useful in

confirming its presence of PAA at the surface of the PAA cellulose composite membranes. Zeta potential analysis (Figure 6.7) clearly shows that incorporating PAA into cellulose membranes results in a greater magnitude of negative surface charge which drastically shifts between pH 3-5, as expected of carboxyl groups. This behavior has been seen in PAA functionalized PVDF membranes as previously studied in our group. Due to the dissolution of PAA and PVDF together in ionic liquid, it is hypothesized that PAA was also integrated through the depth of the membrane.

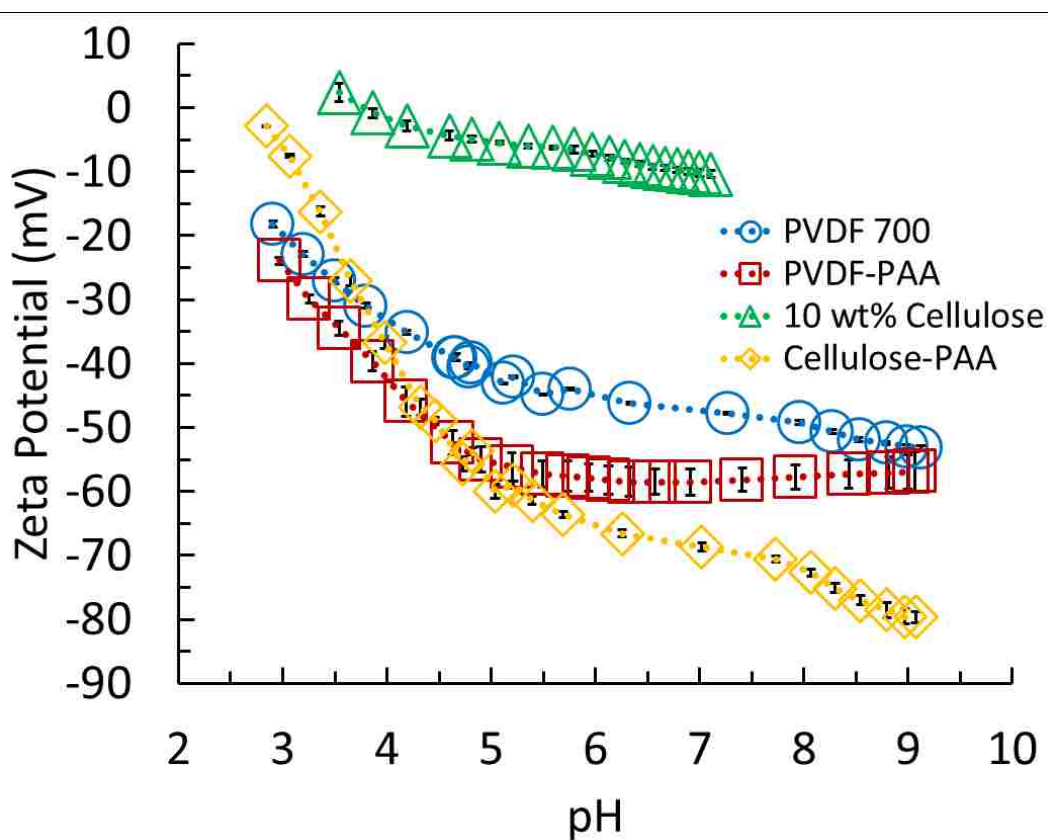


Fig. 6.7. Zeta potential of PVDF 700, PVDF-PAA (weight gain of 7.28% with functionalization), cellulose (10 wt% cellulose in casting solution)¹, and cellulose-PAA membranes in the pH range of 3-9.

Further confirmation of PAA in the membrane was necessary to confirm presence beyond the surface. Pressure dependent flux of PAA cellulose membranes were studied at

below and above the pKa of PAA. As observed in other PAA functionalized membranes, swelling should occur as carboxyl groups are charged when pH increases above 3. Figure 6.8 shows the pH responsive behavior of the functionalized membrane. The four-fold decrease in flux when transitioning to pH 7 from pH 3 strongly suggests presence of PAA throughout the entire selective layer of the composite membrane. At high pH the swollen PAA creates a selective layer capable of rejecting 44% of 5kDa blue dextran, while at low pH the PAA collapses, opening the membrane pores.

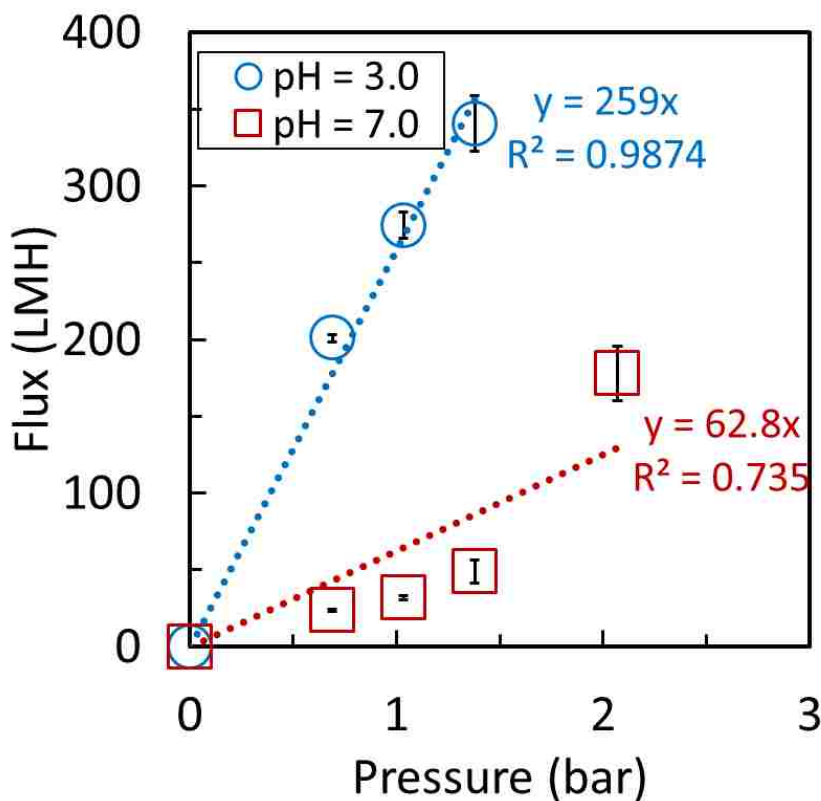


Figure 6.8. Permeability of cellulose-PAA membrane at pH 3 and 7. Membrane surface is 13.2 cm²

PAA has been utilized for metal capture of metals due to the ion exchange capacity of the vast network of carboxylic groups. Ion exchange capacity studied for this membrane using Ca²⁺ to better understand the quantity of PAA in the membrane and the accessibility

of PAA to ions transporting through. Previous functionalized membrane platforms have not completely answered the question of whether the entirety of the hydrogel is available for ion exchange, or whether channeling occurs within the hydrogel domain. Unlike a functionalized pore approach, there are no larger pores through which channeling can occur. In this scenario PAA is entangled along with the cellulose composite membrane which should theoretically prevent channeling. Ca^{2+} adsorption is shown in Figure 6.9. After ion exchange with Ca^{2+} , the ratio of $\text{Ca}^{2+}:\text{COO}^-$ was determined to be 0.347 which was less than the theoretical value of 0.5 in the case of every carboxylic group participating in ion exchange. Previous work in our group with spongy PVDF-PAS membranes exceeds the theoretical value due to counter ion condensation within the membrane. This was not observed in cellulose membranes. likely due to the constrained environment in which the PAA is present.

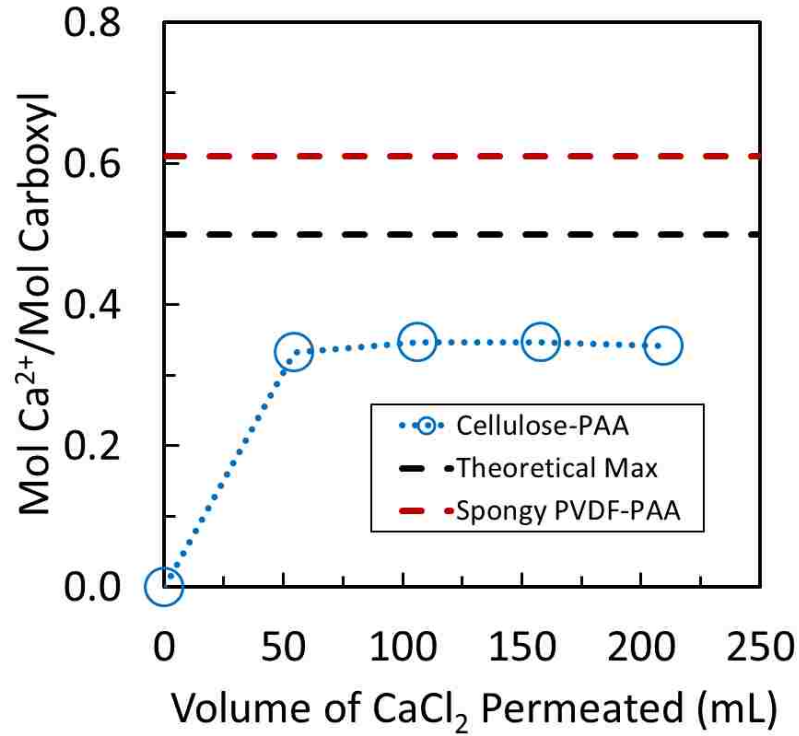


Figure 6.9. Total Ca²⁺ capture of a 13.2-cm² cellulose-PAA membrane during convective flow of CaCl₂ (overall flux = 89 LMH and average pressure of 50-mL increments = 0.72 bar) and of a PVDF-PAA membrane from literature after convective flow of CaCl₂¹⁵².

Electrodispersive x-ray spectroscopy of the PAA cellulose composite membrane was conducted to determine where ion capture was occurring within the membrane. The EDS mapping reveals that PAA cellulose membranes show even dispersion of divalent ions adsorbed throughout the membrane, while PAA functionalized PVDF membranes show divalent ion adsorption only toward the surface of the membrane. The EDS map (Figure 6.10) serves as further confirmation that PAA is evenly dispersed throughout the membrane.

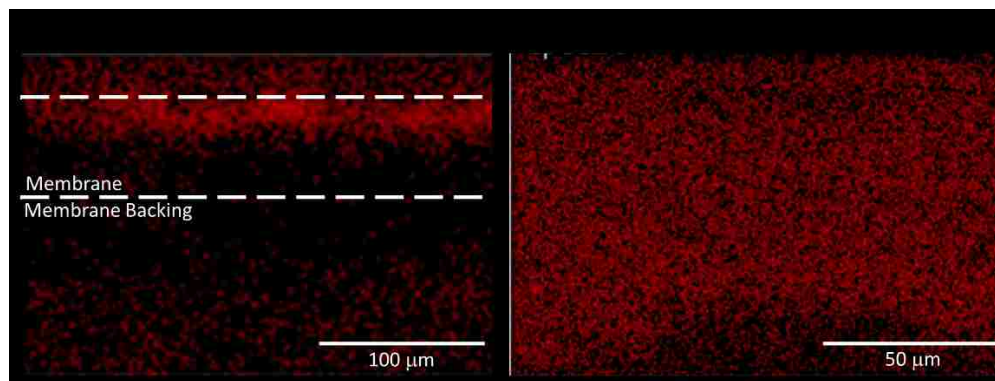


Fig. 6.10 (a) Iron EDS map of the cross section of a PVDF-PAA-Fe sample and (b) Calcium EDS map of most of the cross section of a cellulose-PAA-Ca²⁺ sample.

6.3.4 Lignin Cellulose Composite Membranes

Lignin and cellulose are major constituents of woody plants and interact to create a robust structure that is resistant to decomposition from bacteria and fungi even after the plants death. Lignin contains many hydrophilic groups, including phenols which give antibacterial properties. Houtman et al. have determined through molecular simulation that hydrophilic groups allow for lignin to adsorb to cellulose microfibrils¹⁵³. Lignin sulfonate, a byproduct of chemical paper pulping industry, is an inexpensive and commercially available source of lignin. The sulfonation process adds hydrophilicity and allows for easy dissolution in 1-ethyl-3-methylimidazolium acetate. Therefore, we sought to use it as a composite material for cellulose membrane creation. The primary objectives were to determine the effectiveness of the lignin composite membrane and probe antibacterial behavior.

Water permeability of the lignin cellulose membrane was shown to be roughly double that of the unmodified cellulose membrane (Figure 6.11). Likely hydrophobic regions of lignin sulfonate cause opening of the selective layer due to poor interaction with cellulose after phase inversion. The viscosity of the dope solutions was particularly high

when lignin sulfonate was added as a composite, which may further effect demixing during phase inversion. The rejection of 5000 Da blue dextran was 59%, 16% lower than unmodified cellulose. Neutral red was shown to absorb strongly in within the membrane, which indicates the potential of strong interaction with sulfonate groups within the membrane.

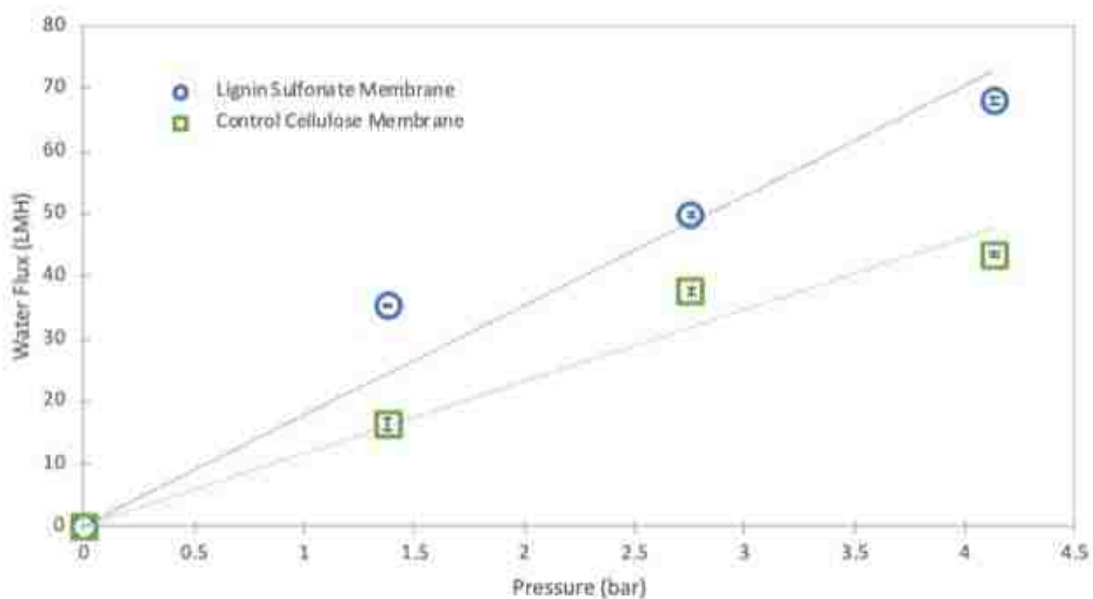


Figure 6.11. Pressure dependent flux of lignin sulfonate membranes as compared to cellulose membranes.

Lignin has been demonstrated to have antibacterial properties¹⁵⁴. Biofouling is a major issue for long term membrane performance, as biofilms of bacteria and extracellular matrix cause tremendous resistance to flow through the membrane¹⁵⁵. Lignin cellulose membranes were inoculated with *Rhodospseudomonas palustris* bacteria by filtering a dilute solution of bacteria through the membrane. *R. palustris* was chosen due to its ability to generate extracellular matrix and also switch metabolism to survive in many different environments¹⁵⁴. The bacteria were then given dilute amounts of nutrients and allowed to

grow. Bacteria colonies were analyzed after fixation to qualitatively determine the rate of production of extracellular matrix. The SEM images of the membrane surface after bacteria growth can be seen in Figure 6.12.

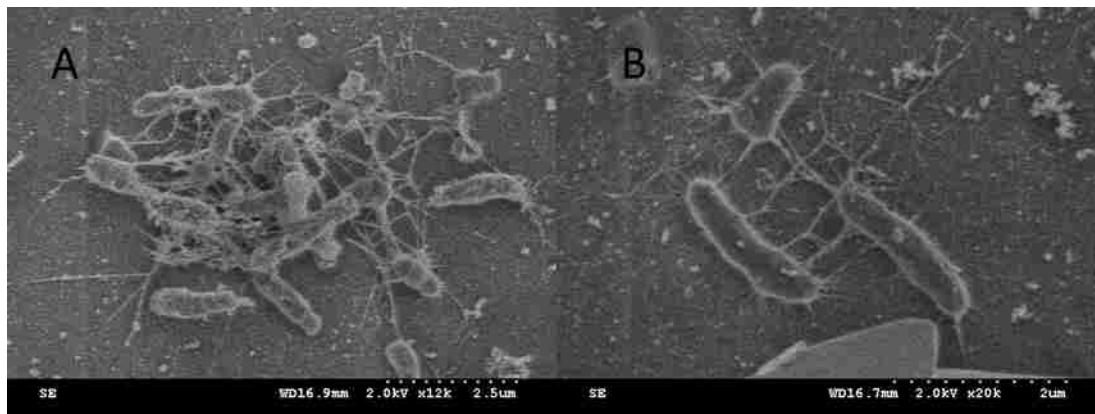


Figure 6.12. Bacteria growth on A) unmodified cellulose membrane and B) lignin cellulose membrane.

6.3.5 Lignin Functionalized Nanofiltration Membrane

Lignin sulfonate can also be directly functionalized onto the surface of commercial nanofiltration membranes. Craft lignin has shown potential antifouling properties when deposited onto the surface of thin film composite membranes¹⁵⁶. This study looked to use heat to esterify lignin to the surface of NF membranes. Details on membrane synthesis is given in Figure 6.13. A LiS slurry was deposited on the membrane surface at pH 3. Heating at 80°C causes esterification of lignin to the unreacted COOH groups at surface of the NF270 membrane.

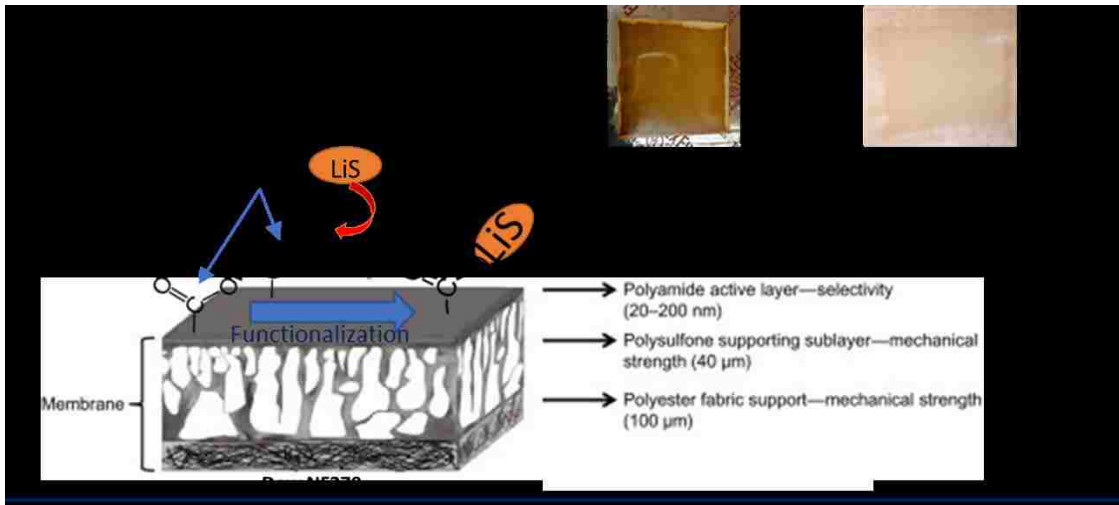
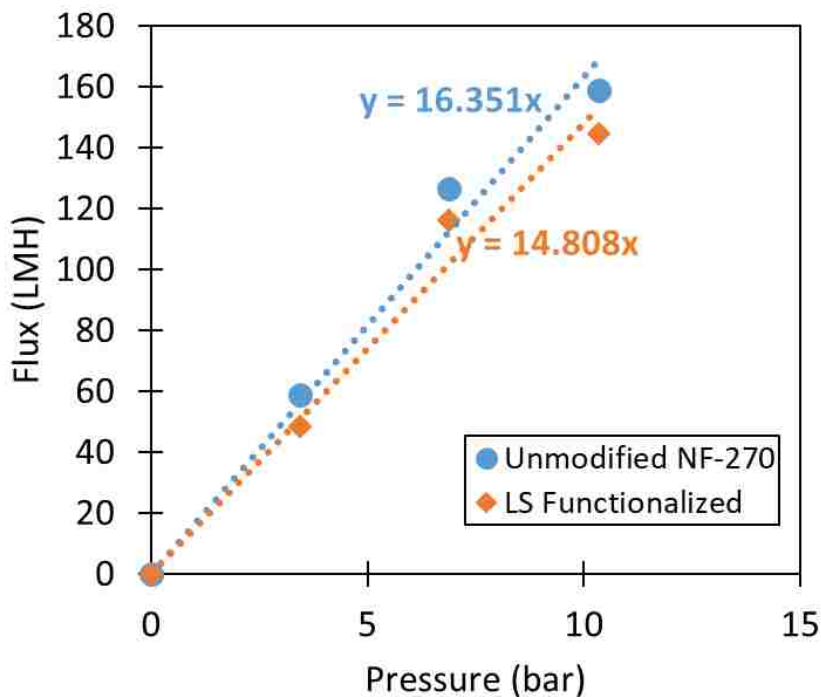


Figure 6.13. Functionalization of commercial DowFilmtec NF270 membrane using heat to esterify lignin sulfonate to unreacted carboxyl groups.

Membrane water permeability was shown to decrease slightly after functionalization (Figure 6.14), but flux decline was less than 10 wt%. This decline in flux was likely due to the surface functionalized layer adding resistance to flow through the

membrane. Lignin has a bulky branching structure that could cause additional resistance to



flow.

Figure 6.14 Pressure dependent water flux of unmodified NF270 and LS Functionalized membrane.

Rejection of Na_2SO_4 also decreased slightly as shown in Table 6.3. This was likely due to esterification of unreacted carboxyl groups on the NF270 surface. This reduced the negative charge of the membrane. Zeta potential data also suggests reduction in the number of carboxyl groups on the surface of the NF membrane (Figure 6.15).

Table 6.3. Rejection of Na_2SO_4 in unmodified NF 270 and lignin sulfonate functionalized NF 270.

(1000 mg/L Na_2SO_4)	Rejection of Na_2SO_4
Unmodified NF-270	98.0%
Lignin Sulfonate Functionalized	97.30%

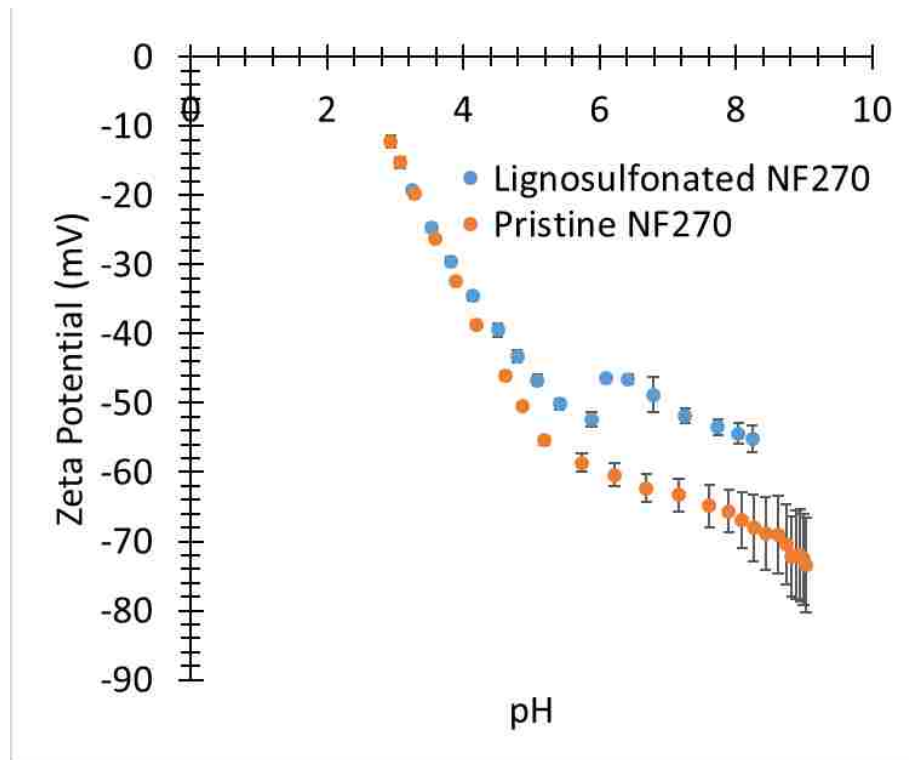


Figure 6.15. Zeta potential vs. pH for lignin functionalized and pristine NF270 membrane. 100 mg/L KCl used as an electrolyte.

Most excitingly, lignin sulfonate functionalized membranes show promise for use as an antifouling surface. BSA was used as a model foulant and passed through the membrane in cross flow operation. BSA fouling during filtration can be seen in Figure 6.16. While lignin sulfonate appears to have negligible impact on reversible fouling, irreversible fouling was shown to be far less prevalent after functionalization with lignin sulfonate. Functionalized NF270 membranes showed almost complete recovery of volumetric water flux after just 10 minutes of tangential rinsing with DI water while the unmodified membrane flux only recovered to 40% of the initial value after rinsing. Lignin functionalized NF270 membranes were shown to maintain 90% of the initial flux after the second rinse cycle.

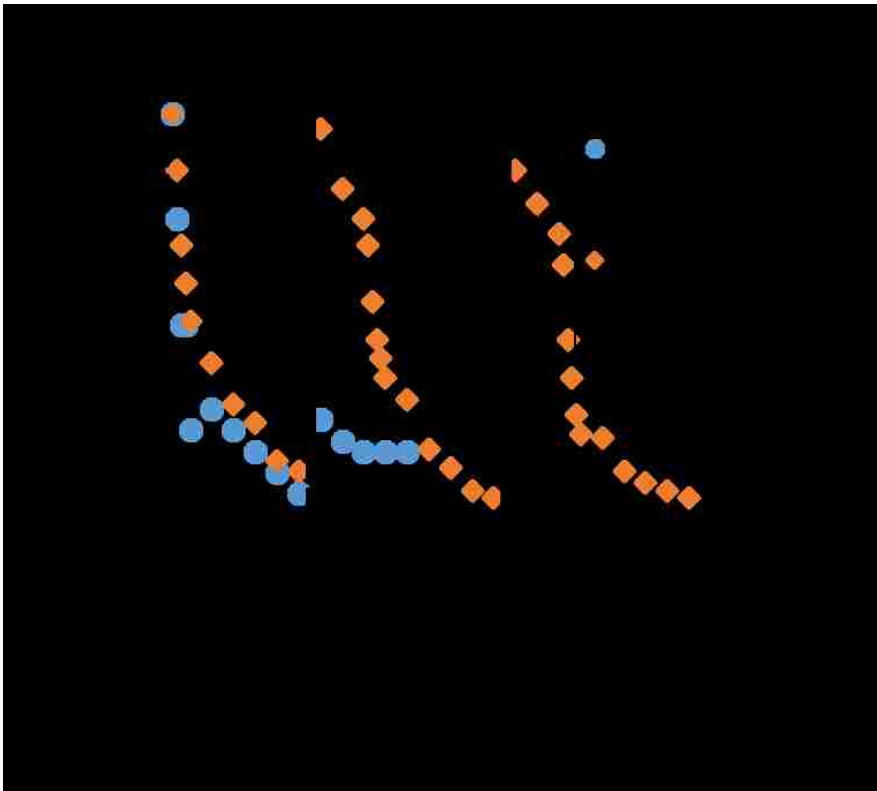


Figure 6.16 . Normalized water flux of lignin sulfonate functionalized and unmodified NF270 during filtration of 100 mg/L BSA. Dotted lines indicate 10 minutes of tangential rinsing with deionized water (pH=5.6)

6.4 Conclusion

This study has built upon our previous work with cellulose composite membranes by showing the same techniques can also be applied with iron, polyacrylic acid, and sulfonated lignin. Composite materials were found to add unique properties such as pH responsive flux and antibacterial behavior. Particularly in iron cellulose membranes suggests composite materials impact transport of solvent and solute through the membrane in ways that could be utilized in applications for cleaning the membrane. Ultimately, as ionic liquids continue to be studied as solvents for membrane synthesis, composite material should be strongly considered as means to add value or otherwise optimize membranes. Even common materials such as iron or sulfonated lignin have shown potential as composite materials, and impart little additional costs compared to the price of ionic liquid. Further development of composite materials, including metalorganics, could advance development cellulose-based membranes for separations and reactions.

\

CHAPTER 7. CONCLUSIONS

The research comprising this dissertation advanced the field of membranes in both selective desalination of industrial wastewater and selective UF/NF separation of small molecules. Ion transport phenomenon have been used to apply membrane technologies to treat and reuse high TDS water from both coal-fired power plants and oil sands tailings. The integration of composite materials into cellulose materials using ionic liquid was a new achievement for membrane applications. This technique has created potential for modifying membrane selectivity and surface properties, as well as adding other functionalities such as pH response or capacity for metal capture

7.1 Key Advancements to Science and Engineering

- Impact of divalent ions on transport behavior of mixed salt solutions was studied for nanofiltration of several complex mixtures of salts in aqueous solution. Ion transport behavior was modeled for single salt solutions as well as mixed salt solutions.
- Selective deionization using polyamide NF membranes was applied for recovery and reuse of industrial wastewater. Process design combining nanofiltration with reactive membranes was implemented to improve heavy metal capture and degradation of organic pollutants in industrial wastewater.
- Cellulose composite membranes were developed using a common ionic liquid solvent. Composite materials, such as GQD, iron, and lignin, are shown to modify membrane selectivity and add unique properties including antifouling behavior.

7.2 Specific Accomplishments

7.2.1 Nanofiltration of mixed salt solutions

- NF membrane ion rejection investigated for single salt solutions of NaCl, Na₂SO₄, CaCl₂, and MgSO₄ as well as NaCl/CaCl₂ mixtures and NaCl/Na₂SO₄ mixtures.
- Presence of divalent ion in mixed salt solutions was demonstrated to reduce rejection of monovalent ions.
- Impact of ionic strength on ion rejection investigated for both divalent and monovalent cations for ionic strengths between (0-350 mM). Significant reduction of rejection was observed for monovalent cations, while steric partitioning causes cation rejection to remain high at high ionic strength.
- Extended Nernst Planck equation was applied with steric partitioning to successfully model ion transfer through nanofiltration membranes in mixed ion solutions using properties optimized from single salt data.

7.2.2 Selective Desalination for Industrial Wastewater Treatment

- Nanofiltration applied to recover up to 80% of FGD wastewater from Plant Bowen, GA for reuse within the wet scrubber.
- Prevalence of divalent cations in FGD Wastewater allows for high rejection (>90%) of TDS at 0% recovery. TDS rejection remains around (85%) at 80% water recovery.
- Heavy metal ions including Se and as were shown to be effectively be rejected (>90%) by nanofiltration of FGD wastewater, allowing for concentration for subsequent removal using functionalized membranes.

- Removal of TDS via NF membranes shown to have beneficial behavior on Se capture in functionalized membrane systems by removing ion (particularly SO_4^{2-}) that compete with Se at the iron nanoparticle active sites.
- Membranes were shown to withstand operation at temperatures between 25-44 °C and presence of suspended solids for over 140 days of operation (non-continuous)
- NF membranes demonstrated effective at removing Naphthenic acid from produced water at over 80% water recovery. Naphthenic acid concentration in NF permeate is suitably low for discharge, while the reduced volume of retentate has concentrated naphthenic acid for more efficient degradation functionalized membranes.

7.2.3 Cellulose composite membranes

- Graphene oxide quantum dots (GQD) (.025 wt%) were integrated into cellulose membranes using a common solvent 1-ethyl-3-methylimidazolium acetate.
- GQD proven to be integrated within the cellulose polymer network after phase inversion using surface property observations and probing GQDs fluorescence using confocal laser microscopy.
- Presence of GQD composite material shown to alter transport behavior for water and ions through the membrane, changing membrane molecular weight cut off and water permeability.
- The same technique for Cellulose GOQD composite membranes can also be used for other composite materials such as polyacrylic acid, iron (III), and lignin sulfonate. Composite materials bring unique properties such as antifouling and allow for tuning of membrane performance.

7.3 Future Work

This work has given new insights into the role of divalent ions in selective desalination of mixed ion solutions via nanofiltration. Transport behavior seen in lab-prepared solutions has been applied to multiple types of industrial wastewater. These studies only seek to explain simple interactions between monovalent and divalent ions during membrane transport. Further complications such as pH sensitivity, precipitation of salts during water recovery, chelation, and interactions with non-ionic solutes require further study. While other studies have addressed these issues independently, industrial wastewater is composed of several different ions, including heavy metals and sparingly soluble ions, along with organic solutes and thus require consideration of many different factors when studying ion transport. Furthermore, while the thermodynamic limits on energy costs for membrane desalination are well understood, further economic analysis on nanofiltration systems for selective desalination must incorporate costs for other unit operations such as pretreatment and elimination of pollutants through capture or reactive degradation.

The initial concept of using cellulose composite materials for membrane synthesis has been proven effective in this study, but challenges remain. Costs of 1-ethyl-3-methylimidazolium acetate are currently prohibitive for large scale cellulose composite membrane production. The issues of cost need to be addressed via two approaches: 1) Incorporation of water into the casting solution at ratios of up to 1:4 water: ionic liquid. 2) Development of energetically efficient processes for ionic liquid recovery after nonsolvent induced phase inversion.

Reducing the amount of solvent used during membrane casting will naturally reduce cost, but the impact on membrane morphology and incorporation of composite

materials into the membrane domain must be further studied. Allowing for water presence in the casting solution will also significantly reduce the thermodynamically required energy for recovery of ionic liquid. Ionic liquid recovery may involve membrane processes for recovery such as the use of ceramic membranes but may also require absorption/extraction or thermal separation to reconstitute ionic liquid to the desired purity. Ultimately the goal must be to allow for as much water presence as possible without compromising membrane selectivity and permeability.

Additional considerations for using other nonsolvent such as isopropanol or liquid CO₂ could be used as a nonsolvent for membrane formation to significantly reduce the energy required for ionic liquid recovery. Changing the nonsolvent requires further investigation into three phase equilibrium behavior and the resulting membrane properties. New nonsolvent might also provide a solution to long term membrane storage, a key area for the scale up of cellulose base membranes. Collapse of pore structures during membrane drying currently require cellulose membranes be stored in water or other polar solvent. Furthermore curling, even after solvent exchange poses a challenge for large scale roll to roll manufacture. Once cellulose based membranes have been optimized for long term storage, module design must be considered before any large-scale application.

NOMENCLATURE

Chapter 1:

TFC Thin Film C

Chapter 2:

A	Membrane water permeability
$C_{0,i}$	Instantaneous permeate concentration of component i
$C_{B,i}$	Bulk concentration of component i
$C_{p,i}$	Overall permeate concentration of component i
J_w	Volumetric flux
Q	Permeate flowrate
R_g	Gas Constant
R_i	Rejection of component i
r	Water recovery (%)
r_p	Rate of formation of precipitate
SA	Surface area of membrane
t	Time
T	Temperature
V	Volume of the feed tank
V_0	Initial volume of the feed tank
W_p	Mass of precipitate formed
ΔP	Applied Pressure
$\Delta \Pi$	Osmotic Pressure

Chapter 3:

J_i	Flux of Solute i
K_d	Hindered Coefficient of Diffusion
D_i	Hindered Diffusivity of Solute i (m^2/s)
c_i	Concentration of solute i within membrane
x	Dimensionless length of membrane channel
z_i	valence of solute i
F	Faraday constant (C/mol)
K_{ic}	Convective transport coefficient (m^2/s) (coupling)
Φ	Electric potential in axial direction inside the membrane(V)
λ	Ratio of ionic or solute radius to pore radius
C_i	Permeate concentration
J_v	Volumetric flux
R	Gas Constant
T	Temperature
r_i	Radius of solute
r_p	Radius of pore
X_d	Membrane charge density (coulombs/ m^2)
ϕ	Steric partitioning coefficient

NOMENCLATURE (cont.)

Chapter 4:

FGD	Flue Gas Desulfurization (Wet Scrubber Process)
TDS	Total Dissolved Solids
TSS	Total Suspended Solids

Chapter 5 &6 :

GQD	Graphene Quantum Dot
PAA	Polyacrylic Acid
LiS	Lignin Sulfonated (regarding functionalized)

APPENDIX

M-file Nernst Planck Model

Working file

```
clc
clear all

global a_part jv xd as rp diff l T z kc kd R F phi cfeed cmem q_cf

xd=-13;

z=[1,-2];

l=8*10^(-6);

cfeed=[10,5];

rp=1.2/2*10^(-9);

as=[0.184,0.231].*10^(-9);

diff=[1.33,1.06].*10^(-9);

T=298;

q_cf=1; %gpm crossflow velocity

for i=1:50
    jv=0.3+(i-0.9)*3.5/5;
    x_axis(i)=jv;
    y=solnpeq(jv);
    y_axis(i)=y;
end

plot(x_axis,y_axis)
hold on

clc
clear all
global a_part jv xd as rp diff l T z kc kd R F phi cfeed cmem
q_cf=1; %gpm crossflow velocity
cfeed=[50,25];
jv=10;
jv=jv/3.6*10^(-6);
xd=-10;
as=[0.1840,0.2309].*10^(-9);
rp=0.5*10^(-9);
diff=[1.33,1.062].*10^(-9);
l=30*10^(-6);
T=298;
z=[1,-2];
```

```

amp1=hinder(as(1));
amp2=hinder(as(2));
kc=[amp1(2),amp2(2)];
kd=[amp1(1),amp2(1)];
R=8.3142;
F=96450;
%steric partitioning
phi=(1-as./rp).^2;
% phi=[0.2,0.6];% very sensitive to partitioning term
y=cpol(jv,q_cf);
rej=0;
amd=rej;
count2=0;
count3=10;
count4=1;
while count4<5
count1=1;
while count1<12
rej(count1)=count2+(count1-1)*count3;
cp=cfeed.*(rej(count1)/100);
ktrans=cpol(jv,q_cf);
% cmem=(jv.*cp+ktrans.*cfeed)./ktrans;
cmem=cp+(cfeed-cp)*exp(jv/ktrans);
%a_part
x0=[1,1,1];
fun=@partitioning;
a_part=fsolve(fun,x0);
x0=[1,1,1,1,1,1];
fun=@np;
out_prof=fsolve(fun,x0);
clc
y_rej(count1)=(cfeed(1)-out_prof(3))/cfeed(1)*100;
count1=count1+1;
end
count1=1;
err=y_rej-rej;
while count1<12
if err(count1)<0
amd=(count1-2)*count3;
count1=12;
end
count1=count1+1;
end
count2=count2+amd;
count3=count3/10;
count4=count4+1;
end
rej=count2

function y=solnpeq(jv)

global a_part jv xd as rp diff l T z kc kd R F phi cfeed cmem q_cf

jv=jv/3.6*10^(-6);

amp1=hinder(as(1));

```

```

amp2=hinder(as(2));
kc=[amp1(2),amp2(2)];
kd=[amp1(1),amp2(1)];
R=8.3142;
F=96450;
%steric partitioning
phi=(1-as./rp).^2;
% phi=[0.2,0.6];% very sensitive to partitioning term
y=cpol(jv,q_cf);
rej=0;
amd=rej;
count2=0;
count3=10;
count4=1;
while count4<4
count1=1;
while count1<12
rej(count1)=count2+(count1-1)*count3;
cp=cfeed.*(rej(count1)/100);
ktrans=cpol(jv,q_cf);
% cmem=(jv.*cp+ktrans.*cfeed)./ktrans;
cmem=cp+(cfeed-cp)*exp(jv/ktrans);
%a_part
x0=[1,1,1];
fun=@partitioning;
a_part=fsolve(fun,x0);
x0=[1,1,1,1,1,1];
fun=@np;
out_prof=fsolve(fun,x0);
clc
y_rej(count1)=(cfeed(1)-out_prof(3))/cfeed(1)*100;
count1=count1+1;
end
count1=1;
err=y_rej-rej;
while count1<12
if err(count1)<0
amd=(count1-2)*count3;
count1=12;
end
count1=count1+1;
end
count2=count2+amd;
count3=count3/10;
count4=count4+1;
end
y=count2;
end

function z=hinder(ri)%[kd,kc]
global rp
lam=ri/rp;
kid=1-2.3*lam+1.154*lam*lam+0.224*lam*lam*lam;
kic=1+0.054*lam-0.988*lam*lam+0.441*lam*lam*lam;

%% from bowen 1995

```

```

% kid=-1.705*lam+0.946;
% kic=-0.301*lam+1.022;
%%

z(1)=kid;%diffusion
z(2)=kic;%convection
end

function y=np(x)
global a_part jv xd as rp diff l T z kc kd R F phi

%a_part is intial partitioning and potential term

%phi is net partitioning factor: steric

p=diff./l;
res=(R*T*1/F)./z./diff;
y(1,1)=-p(1)*(x(1)-a_part(1))+kc(1)*jv*a_part(1)+(x(5)-a_part(3))*a_part(1)/res(1)-jv*x(3);
y(2,1)=-p(2)*(x(2)-a_part(2))+kc(2)*jv*a_part(2)+(x(5)-a_part(3))/res(2)*a_part(2)-jv*x(4);
y(3,1)=z(1)*x(1)+z(2)*x(2)+xd;
y(4,1)=phi(1)*x(3)-x(1)*exp((x(6)-x(5))*z(1)*F/R/T);
y(5,1)=phi(2)*x(4)-x(2)*exp((x(6)-x(5))*z(2)*F/R/T);
y(6,1)=z(1)*x(3)+z(2)*x(4);
end

function y=partitioning(x)
global xd z cmem T R F rp as phi
cf1=cmem(1);
cf2=cmem(2);
z1=z(1);
z2=z(2);
% y(1,1)=x(1)-phi(1)*cf1*exp(z1*x(3)*F/R/T);
% y(2,1)=x(2)-phi(2)*cf2*exp(z2*x(3)*F/R/T);
y(1,1)=x(1)-
phi(1)*cf1*(1+(z1*x(3)*F/R/T)+(z1*x(3)*F/R/T)^2/2+(z1*x(3)*F/R/T)^3/6+(z1*x(3)*F/R/T)^4/24+(
z1*x(3)*F/R/T)^5/120+(z1*x(3)*F/R/T)^6/720+(z1*x(3)*F/R/T)^7/5040+(z1*x(3)*F/R/T)^8/40320
+(z1*x(3)*F/R/T)^9/362880+(z1*x(3)*F/R/T)^10/3628800+(z1*x(3)*F/R/T)^11/3628800/11+(z1*x(
3)*F/R/T)^12/3628800/11/12);
y(2,1)=x(2)-
phi(2)*cf2*(1+(z2*x(3)*F/R/T)+(z2*x(3)*F/R/T)^2/2+(z2*x(3)*F/R/T)^3/6+(z2*x(3)*F/R/T)^4/24+(
z2*x(3)*F/R/T)^5/120+(z2*x(3)*F/R/T)^6/720+(z2*x(3)*F/R/T)^7/5040+(z2*x(3)*F/R/T)^8/40320
+(z2*x(3)*F/R/T)^9/362880+(z2*x(3)*F/R/T)^10/3628800+(z2*x(3)*F/R/T)^11/3628800/11+(z2*x(
3)*F/R/T)^12/3628800/11/12);
y(3,1)=z1*x(1)+z2*x(2)+xd;
end

%masstransfer
function y=cpol(jv,q_cf)%jv in m/sec, q_cf in GPM

global chn_length chn_ht diff

diff=[1.33,1.062].*10^(-9);

q_cf=q_cf*3.7*0.001/60;%1 gpm flow through channels

```

```

chn_length=3.9*10^(-2);
chn_ht=0.23*10^(-2);
mean_diff=(diff(1)*diff(2))^(0.5);
cf_mean=q_cf/chn_length/chn_ht; %m/sec
% ken_mu_water=9.121*10^(-7); %m2/s
% Re=cf_mean*chn_ht/ken_mu_water;
% sc=ken_mu_water/mean_diff;
% sh=1.62*Re^(0.33)*sc^(0.33)*(2*chn_ht/chn_length)^(0.33);
% kc=sh*mean_diff/chn_length; %m/sec
abd=3*cf_mean/chn_ht*2;
ktrans=0.807*(abd*mean_diff*mean_diff/chn_length)^(1/3);
y=ktrans;
end

```

REFERENCES

1. Shiklomanov, I. A., Water in Crisis. In *Water in Crisis*, Gleick, P. H., Ed. Oxford University Press: New York, NY, 1993; pp 13-24.
2. Masten, S. J.; Davies, S. H.; McElmurry, S. P., Flint Water Crisis: What Happened and Why? *Journal - American Water Works Association* **2016**, *108* (12), 22-34.
3. Pelley, J., Taming Toxic Algae Blooms. *ACS central science* **2016**, *2* (5), 270-273.
4. Swain, A., *Water Wars*. 2015; p 443-447.
5. Van der Bruggen, B.; Everaert, K.; Wilms, D.; Vandecasteele, C., Application of nanofiltration for removal of pesticides, nitrate and hardness from ground water: rejection properties and economic evaluation. *Journal of Membrane Science* **2001**, *193* (2), 239-248.
6. Yoon, Y.; Lueptow, R. M., Removal of organic contaminants by RO and NF membranes. *Journal of Membrane Science* **2005**, *261* (1), 76-86.
7. Richard Bowen, W.; Wahab Mohammad, A., Diafiltration by nanofiltration: Prediction and optimization. **1998**, *44* (8), 1799-1812.
8. Cadotte, J.; Forester, R.; Kim, M.; Petersen, R.; Stocker, T., Nanofiltration membranes broaden the use of membrane separation technology. *Desalination* **1988**, *70* (1), 77-88.
9. Simpson, A. E.; Kerr, C. A.; Buckley, C. A., The effect of pH on the nanofiltration of the carbonate system in solution. *Desalination* **1987**, *64*, 305-319.
10. Weinman, S. T.; Bass, M.; Pandit, S.; Herzberg, M.; Freger, V.; Husson, S. M., A switchable zwitterionic membrane surface chemistry for biofouling control. *Journal of Membrane Science* **2018**, *548*, 490-501.
11. da Silva Bural, J.; Peeva, L.; Livingston, A., Negligible ageing in poly(ether-ether-ketone) membranes widens application range for solvent processing. *Journal of Membrane Science* **2017**, *525*, 48-56.
12. Marchetti, P.; Jimenez Solomon, M. F.; Szekely, G.; Livingston, A. G., Molecular Separation with Organic Solvent Nanofiltration: A Critical Review. *Chemical Reviews* **2014**, *114* (21), 10735-10806.
13. Aher, A.; Cai, Y.; Majumder, M.; Bhattacharyya, D., Synthesis of graphene oxide membranes and their behavior in water and isopropanol. *Carbon* **2017**, *116*, 145-153.
14. Hołda, A. K.; Vankelecom, I. F. J., Understanding and guiding the phase inversion process for synthesis of solvent resistant nanofiltration membranes. **2015**, *132* (27).
15. Schaep, J.; Van der Bruggen, B.; Uytterhoeven, S.; Croux, R.; Vandecasteele, C.; Wilms, D.; Van Houtte, E.; Vanlerberghe, F., Removal of hardness from groundwater by nanofiltration. *Desalination* **1998**, *119* (1-3), 295-301.
16. Akbari, A.; Remigy, J. C.; Aptel, P., Treatment of textile dye effluent using a polyamide-based nanofiltration membrane. *Chemical Engineering and Processing: Process Intensification* **2002**, *41* (7), 601-609.
17. Dyke, C. A.; Bartels, C. R., Removal of organics from offshore produced waters using nanofiltration membrane technology. **1990**, *9* (3), 183-186.
18. Nghiem, L. D.; Schäfer, A. I.; Elimelech, M., Pharmaceutical Retention Mechanisms by Nanofiltration Membranes. *Environmental Science & Technology* **2005**, *39* (19), 7698-7705.
19. Kose Mutlu, B.; Cantoni, B.; Turolla, A.; Antonelli, M.; Hsu-Kim, H.; Wiesner, M. R., Application of nanofiltration for Rare Earth Elements recovery from coal fly ash

- leachate: Performance and cost evaluation. *Chemical Engineering Journal* **2018**, *349*, 309-317.
20. Wijmans, J. G.; Baker, R. W., The solution-diffusion model: a review. *Journal of Membrane Science* **1995**, *107* (1), 1-21.
 21. Bowen, W. R.; Welfoot, J. S., Modelling the performance of membrane nanofiltration—critical assessment and model development. *Chemical Engineering Science* **2002**, *57* (7), 1121-1137.
 22. Peeters, J. M. M.; Boom, J. P.; Mulder, M. H. V.; Strathmann, H., Retention measurements of nanofiltration membranes with electrolyte solutions. *Journal of Membrane Science* **1998**, *145* (2), 199-209.
 23. Déon, S.; Escoda, A.; Fievet, P.; Dutournié, P.; Bourseau, P., How to use a multi-ionic transport model to fully predict rejection of mineral salts by nanofiltration membranes. *Chemical Engineering Journal* **2012**, *189-190*, 24-31.
 24. Bandini, S.; Vezzani, D., Nanofiltration modeling: the role of dielectric exclusion in membrane characterization. *Chemical Engineering Science* **2003**, *58* (15), 3303-3326.
 25. Cadotte, J. E.; King, R. S.; Majerle, R. J.; Petersen, R. J., Interfacial Synthesis in the Preparation of Reverse Osmosis Membranes. *Journal of Macromolecular Science: Part A - Chemistry* **1981**, *15* (5), 727-755.
 26. Gu, J.-E.; Lee, S.; Stafford, C. M.; Lee, J. S.; Choi, W.; Kim, B.-Y.; Baek, K.-Y.; Chan, E. P.; Chung, J. Y.; Bang, J.; Lee, J.-H., Molecular Layer-by-Layer Assembled Thin-Film Composite Membranes for Water Desalination. **2013**, *25* (34), 4778-4782.
 27. Li, X.; Chou, S.; Wang, R.; Shi, L.; Fang, W.; Chaitra, G.; Tang, C. Y.; Torres, J.; Hu, X.; Fane, A. G., Nature gives the best solution for desalination: Aquaporin-based hollow fiber composite membrane with superior performance. *Journal of Membrane Science* **2015**, *494*, 68-77.
 28. Moulherat, C.; Tengberg, M.; Haquet, J.-F.; Mille, B. t., First Evidence of Cotton at Neolithic Mehrgarh, Pakistan: Analysis of Mineralized Fibres from a Copper Bead. *Journal of Archaeological Science* **2002**, *29* (12), 1393-1401.
 29. Sahoo, C.; Baruah, P., Empire of Cotton; A New History of Global Capitalism. *Journal of Alternative Perspectives in the Social Sciences* **2018**, *9* (1), 118-121.
 30. Huq, A.; Yunus, M.; Sohel, S. S.; Bhuiya, A.; Emch, M.; Luby, S. P.; Russek-Cohen, E.; Nair, G. B.; Sack, R. B.; Colwell, R. R., Simple Sari Cloth Filtration of Water Is Sustainable and Continues To Protect Villagers from Cholera in Matlab, Bangladesh. **2010**, *1* (1).
 31. Banks, W.; Sharples, A., STUDIES ON DESALINATION BY REVERSE OSMOSIS .I. STRUCTURE AND ASYMMETRIC FLOW PROPERTIES OF CELLULOSE ACETATE DESALINATION MEMBRANES. *Journal of Applied Chemistry* **1966**, *16* (1), 28-+.
 32. Wang, S.; Lu, A.; Zhang, L., Recent advances in regenerated cellulose materials. *Progress in Polymer Science* **2016**, *53*, 169-206.
 33. Parthasarathi, R.; Balamurugan, K.; Shi, J.; Subramanian, V.; Simmons, B. A.; Singh, S., Theoretical Insights into the Role of Water in the Dissolution of Cellulose Using IL/Water Mixed Solvent Systems. *The Journal of Physical Chemistry B* **2015**, *119* (45), 14339-14349.

34. Li, X. L.; Zhu, L. P.; Zhu, B. K.; Xu, Y. Y., High-flux and anti-fouling cellulose nanofiltration membranes prepared via phase inversion with ionic liquid as solvent. *Separation and Purification Technology* **2011**, *83*, 66-73.
35. Novoselov, K. S.; Geim, A. K.; Morozov, S. V.; Jiang, D.; Zhang, Y.; Dubonos, S. V.; Grigorieva, I. V.; Firsov, A. A., Electric Field Effect in Atomically Thin Carbon Films. **2004**, *306* (5696), 666-669.
36. Zhou, S.; Xu, H.; Gan, W.; Yuan, Q., Graphene quantum dots: recent progress in preparation and fluorescence sensing applications. *RSC Advances* **2016**, *6* (112), 110775-110788.
37. Jana, N. R.; Ray, S. C., Chapter 3 - Graphene-Based Carbon Nanoparticles for Bioimaging Applications. In *Applications of Graphene and Graphene-Oxide Based Nanomaterials*, Ray, S. C., Ed. William Andrew Publishing: Oxford, 2015; pp 57-84.
38. Suk-Ho, C., Unique properties of graphene quantum dots and their applications in photonic/electronic devices. *Journal of Physics D: Applied Physics* **2017**, *50* (10), 103002.
39. Sun, Y. P.; Zhou, B.; Lin, Y.; Wang, W.; Fernando, K. A. S.; Pathak, P.; Meziari, M. J.; Harruff, B. A.; Wang, X.; Wang, H. F.; Luo, P. J. G.; Yang, H.; Kose, M. E.; Chen, B. L.; Veca, L. M.; Xie, S. Y., Quantum-sized carbon dots for bright and colorful photoluminescence. *J. Am. Chem. Soc.* **2006**, *128* (24), 7756-7757.
40. Ristic, B. Z.; Milenkovic, M. M.; Dakic, I. R.; Todorovic-Markovic, B. M.; Milosavljevic, M. S.; Budimir, M. D.; Paunovic, V. G.; Dramicanin, M. D.; Markovic, Z. M.; Trajkovic, V. S., Photodynamic antibacterial effect of graphene quantum dots. *Biomaterials* **2014**, *35* (15), 4428-4435.
41. Akhavan, O.; Ghaderi, E., Toxicity of Graphene and Graphene Oxide Nanowalls Against Bacteria. *ACS Nano* **2010**, *4* (10), 5731-5736.
42. Zhao, D. L.; Chung, T.-S., Applications of carbon quantum dots (CQDs) in membrane technologies: A review. *Water Research* **2018**, *147*, 43-49.
43. Wang, T.; Zhu, S.; Jiang, X., Toxicity mechanism of graphene oxide and nitrogen-doped graphene quantum dots in RBCs revealed by surface-enhanced infrared absorption spectroscopy. *Toxicology Research* **2015**, *4* (4), 885-894.
44. Wang, S.; Cole, I. S.; Li, Q., The toxicity of graphene quantum dots. *RSC Advances* **2016**, *6* (92), 89867-89878.
45. Shang, W.; Zhang, X.; Zhang, M.; Fan, Z.; Sun, Y.; Han, M.; Fan, L., The uptake mechanism and biocompatibility of graphene quantum dots with human neural stem cells. *Nanoscale* **2014**, *6* (11), 5799-5806.
46. Chong, Y.; Ge, C.; Fang, G.; Tian, X.; Ma, X.; Wen, T.; Wamer, W. G.; Chen, C.; Chai, Z.; Yin, J.-J., Crossover between Anti- and Pro-oxidant Activities of Graphene Quantum Dots in the Absence or Presence of Light. *ACS Nano* **2016**, *10* (9), 8690-8699.
47. Zhou, Y.; Sun, H.; Wang, F.; Ren, J.; Qu, X., How functional groups influence the ROS generation and cytotoxicity of graphene quantum dots. *Chemical Communications* **2017**, *53* (76), 10588-10591.
48. Li, Q.; Chen, B.; Xing, B., Aggregation Kinetics and Self-Assembly Mechanisms of Graphene Quantum Dots in Aqueous Solutions: Cooperative Effects of pH and Electrolytes. *Environmental Science & Technology* **2017**, *51* (3), 1364-1376.
49. Kumar, V. B.; Borenstein, A.; Markovsky, B.; Aurbach, D.; Gedanken, A.; Talianker, M.; Porat, Z., Activated Carbon Modified with Carbon Nanodots as Novel

Electrode Material for Supercapacitors. *The Journal of Physical Chemistry C* **2016**, *120* (25), 13406-13413.

50. Renkin, E. M., FILTRATION, DIFFUSION, AND MOLECULAR SIEVING THROUGH POROUS CELLULOSE MEMBRANES. **1954**, *38* (2), 225-243.

51. Freger, V., Swelling and Morphology of the Skin Layer of Polyamide Composite Membranes: An Atomic Force Microscopy Study. *Environmental Science & Technology* **2004**, *38* (11), 3168-3175.

52. Yaroshchuk, A. E., Non-steric mechanisms of nanofiltration: superposition of Donnan and dielectric exclusion. *Separation and Purification Technology* **2001**, (22-23), 143-158.

53. Ernst, M.; Bismarck, A.; Springer, J.; Jekel, M., Zeta-potential and rejection rates of a polyethersulfone nanofiltration membrane in single salt solutions. *Journal of Membrane Science* **2000**, *165* (2), 251-259.

54. Hagemeyer, G.; Gimbel, R., Modelling the rejection of nanofiltration membranes using zeta potential measurements. *Separation and Purification Technology* **1999**, *15* (1), 19-30.

55. Yaroshchuk, A. E., Dielectric exclusion of ions from membranes. *Advances in Colloid and Interface Science* **2000**, *85* (2-3), 193-230.

56. Hagemeyer, G.; Gimbel, R., Modelling the salt rejection of nanofiltration membranes for ternary ion mixtures and for single salts at different pH values. *Desalination* **1998**, *117* (1-3), 247-256.

57. Van der Bruggen, B.; Koninckx, A.; Vandecasteele, C., Separation of monovalent and divalent ions from aqueous solution by electrodialysis and nanofiltration. *Water Research* **2004**, *38* (5), 1347-1353.

58. Fang, W.; Shi, L.; Wang, R., Mixed polyamide-based composite nanofiltration hollow fiber membranes with improved low-pressure water softening capability. *Journal of Membrane Science* **2014**, *468* (0), 52-61.

59. Setiawan, L.; Shi, L.; Wang, R., Dual layer composite nanofiltration hollow fiber membranes for low-pressure water softening. *Polymer* **2014**, *55* (6), 1367-1374.

60. Fang, W.; Shi, L.; Wang, R., Interfacially polymerized composite nanofiltration hollow fiber membranes for low-pressure water softening. *Journal of Membrane Science* **2013**, *430* (0), 129-139.

61. Pérez-González, A.; Ibáñez, R.; Gómez, P.; Urtiaga, A. M.; Ortiz, I.; Irabien, J. A., Nanofiltration separation of polyvalent and monovalent anions in desalination brines. *Journal of Membrane Science* **2015**, *473* (0), 16-27.

62. Cavaco Morão, A. I.; Szymczyk, A.; Fievet, P.; Brites Alves, A. M., Modelling the separation by nanofiltration of a multi-ionic solution relevant to an industrial process. *Journal of Membrane Science* **2008**, *322* (2), 320-330.

63. Déon, S.; Dutournié, P.; Fievet, P.; Limousy, L.; Bourseau, P., Concentration polarization phenomenon during the nanofiltration of multi-ionic solutions: Influence of the filtrated solution and operating conditions. *Water Research* **2013**, *47* (7), 2260-2272.

64. Sharma, R. R.; Chellam, S., Solute rejection by porous thin film composite nanofiltration membranes at high feed water recoveries. *Journal of Colloid and Interface Science* **2008**, *328* (2), 353-366.

65. Mondal, S.; Wickramasinghe, S. R., Produced water treatment by nanofiltration and reverse osmosis membranes. *Journal of Membrane Science* **2008**, *322* (1), 162-170.

66. Tanninen, J.; Platt, S.; Weis, A.; Nyström, M., Long-term acid resistance and selectivity of NF membranes in very acidic conditions. *Journal of Membrane Science* **2004**, *240* (1–2), 11-18.
67. Boussu, K.; Zhang, Y.; Cocquyt, J.; Van der Meeren, P.; Volodin, A.; Van Haesendonck, C.; Martens, J. A.; Van der Bruggen, B., Characterization of polymeric nanofiltration membranes for systematic analysis of membrane performance. *Journal of Membrane Science* **2006**, *278* (1–2), 418-427.
68. Nightingale, E. R., Phenomenological Theory of Ion Solvation. Effective Radii of Hydrated Ions. *The Journal of Physical Chemistry* **1959**, *63* (9), 1381-1387.
69. Salgin, S., Salgin, U. , Soyer, Streaming Potential Measurements of Polyethersulfon Ultrafiltration membranes to Determine Salt Effects on Membrane Zeta Potential. *International Journal of Electrochemical Science* **2013**, *2013* (8), 4073-4084.
70. Garcia-Aleman, J.; Dickson, J. M., Permeation of mixed-salt solutions with commercial and pore-filled nanofiltration membranes: membrane charge inversion phenomena. *Journal of Membrane Science* **2004**, *239* (2), 163-172.
71. Coday, B. D.; Luxbacher, T.; Childress, A. E.; Almaraz, N.; Xu, P.; Cath, T. Y., Indirect determination of zeta potential at high ionic strength: Specific application to semipermeable polymeric membranes. *Journal of Membrane Science* **2015**, *478*, 58-64.
72. Cheng, S.; Oatley, D. L.; Williams, P. M.; Wright, C. J., Characterisation and application of a novel positively charged nanofiltration membrane for the treatment of textile industry wastewaters. *Water Research* **2012**, *46* (1), 33-42.
73. Aydiner, C.; Sen, U.; Topcu, S.; Ekinci, D.; Altinay, A. D.; Koseoglu-Imer, D. Y.; Keskinler, B., Techno-economic viability of innovative membrane systems in water and mass recovery from dairy wastewater. *Journal of Membrane Science* **2014**, *458* (0), 66-75.
74. Gur-Reznik, S.; Koren-Menashe, I.; Heller-Grossman, L.; Rufel, O.; Dosoretz, C. G., Influence of seasonal and operating conditions on the rejection of pharmaceutical active compounds by RO and NF membranes. *Desalination* **2011**, *277* (1–3), 250-256.
75. Çakmakce, M.; Kayaalp, N.; Koyuncu, I., Desalination of produced water from oil production fields by membrane processes. *Desalination* **2008**, *222* (1–3), 176-186.
76. Alzahrani, S.; Mohammad, A. W., Challenges and trends in membrane technology implementation for produced water treatment: A review. *Journal of Water Process Engineering* **2014**, *4* (0), 107-133.
77. McCool, B. C.; Rahardianto, A.; Faria, J. I.; Cohen, Y., Evaluation of chemically-enhanced seeded precipitation of RO concentrate for high recovery desalting of high salinity brackish water. *Desalination* **2013**, *317* (0), 116-126.
78. Azimi, G.; Papangelakis, V. G.; Dutrizac, J. E., Modelling of calcium sulphate solubility in concentrated multi-component sulphate solutions. *Fluid Phase Equilibria* **2007**, *260* (2), 300-315.
79. Haynes, W. M. L. D. R., CRC Handbook of Chemistry and Physics 95th Edition. CRC Press: Boca Raton, Fla., 2014.
80. Le Gouellec, Y. A.; Elimelech, M., Calcium sulfate (gypsum) scaling in nanofiltration of agricultural drainage water. *Journal of Membrane Science* **2002**, *205* (1–2), 279-291.

81. Mi, B.; Elimelech, M., Gypsum Scaling and Cleaning in Forward Osmosis: Measurements and Mechanisms. *Environmental Science & Technology* **2010**, *44* (6), 2022-2028.
82. Kestin, J., Sokolov, M., Wakeham, W., Viscosity of Liquid Water in the Range -8°C to 150°C. *Journal of Physical Chemistry Reference Data* **1978**, *7* (3), 941-948.
83. Simons, R., Trace element removal from ash dam waters by nanofiltration and diffusion dialysis. *Desalination* **1993**, *89* (3), 325-341.
84. Gui, M.; Papp, J. K.; Colburn, A. S.; Meeks, N. D.; Weaver, B.; Wilf, I.; Bhattacharyya, D., Engineered iron/iron oxide functionalized membranes for selenium and other toxic metal removal from power plant scrubber water. *Journal of Membrane Science* **2015**, *488*, 79-91.
85. Bates, R. G.; Staples, B. R.; Robinson, R. A., Ionic hydration and single ion activities in unassociated chlorides at high ionic strengths. *Analytical Chemistry* **1970**, *42* (8), 867-871.
86. Aher, A.; Papp, J.; Colburn, A.; Wan, H.; Hatakeyama, E.; Prakash, P.; Weaver, B.; Bhattacharyya, D., Naphthenic acids removal from high TDS produced water by persulfate mediated iron oxide functionalized catalytic membrane, and by nanofiltration. *Chemical engineering journal (Lausanne, Switzerland : 1996)* **2017**, *327*, 573-583.
87. Bowen, W. R.; Mohammad, A. W.; Hilal, N., Characterisation of nanofiltration membranes for predictive purposes—use of salts, uncharged solutes and atomic force microscopy. *Journal of Membrane Science* **1997**, *126* (1), 91-105.
88. Colburn, A. S.; Meeks, N.; Weinman, S. T.; Bhattacharyya, D., High Total Dissolved Solids Water Treatment by Charged Nanofiltration Membranes Relating to Power Plant Applications. *Ind. Eng. Chem. Res.* **2016**, *55* (14), 4089-4097.
89. Higuchi, A.; Tamai, M.; Ko, Y.-A.; Tagawa, Y.-I.; Wu, Y.-H.; Freeman, B. D.; Bing, J.-T.; Chang, Y.; Ling, Q.-D., Polymeric Membranes for Chiral Separation of Pharmaceuticals and Chemicals. *Polymer Reviews* **2010**, *50* (2), 113-143.
90. Ge, Q.; Wang, P.; Wan, C.; Chung, T.-S., Polyelectrolyte-Promoted Forward Osmosis–Membrane Distillation (FO–MD) Hybrid Process for Dye Wastewater Treatment. *Environmental Science & Technology* **2012**, *46* (11), 6236-6243.
91. Kim, J.; Van der Bruggen, B., The use of nanoparticles in polymeric and ceramic membrane structures: Review of manufacturing procedures and performance improvement for water treatment. *Environmental Pollution* **2010**, *158* (7), 2335-2349.
92. Ganesh, B. M.; Isloor, A. M.; Ismail, A. F., Enhanced hydrophilicity and salt rejection study of graphene oxide-polysulfone mixed matrix membrane. *Desalination* **2013**, *313* (Supplement C), 199-207.
93. Hosseini, S. M.; Jashni, E.; Habibi, M.; Nemati, M.; Van der Bruggen, B., Evaluating the ion transport characteristics of novel graphene oxide nanoplates entrapped mixed matrix cation exchange membranes in water deionization. *Journal of Membrane Science* **2017**, *541* (Supplement C), 641-652.
94. Zinadini, S.; Zinatizadeh, A. A.; Rahimi, M.; Vatanpour, V.; Zangeneh, H., Preparation of a novel antifouling mixed matrix PES membrane by embedding graphene oxide nanoplates. *Journal of Membrane Science* **2014**, *453* (Supplement C), 292-301.
95. Balta, S.; Sotto, A.; Luis, P.; Benea, L.; Van der Bruggen, B.; Kim, J., A new outlook on membrane enhancement with nanoparticles: The alternative of ZnO. *Journal of Membrane Science* **2012**, *389* (Supplement C), 155-161.

96. Mahajan, R.; Koros, W. J., Factors Controlling Successful Formation of Mixed-Matrix Gas Separation Materials. *Industrial & Engineering Chemistry Research* **2000**, *39* (8), 2692-2696.
97. Chou, W.-L.; Yu, D.-G.; Yang, M.-C., The preparation and characterization of silver-loading cellulose acetate hollow fiber membrane for water treatment. *Polymers for Advanced Technologies* **2005**, *16* (8), 600-607.
98. Aher, A.; Cai, Y.; Majumder, M.; Bhattacharyya, D., Synthesis of graphene oxide membranes and their behavior in water and isopropanol. *Carbon* **2017**, *116* (Supplement C), 145-153.
99. Akbari, A.; Sheath, P.; Martin, S. T.; Shinde, D. B.; Shaibani, M.; Banerjee, P. C.; Tkacz, R.; Bhattacharyya, D.; Majumder, M., Large-area graphene-based nanofiltration membranes by shear alignment of discotic nematic liquid crystals of graphene oxide. **2016**, *7*, 10891.
100. Zhang, C.; Wei, K.; Zhang, W.; Bai, Y.; Sun, Y.; Gu, J., Graphene Oxide Quantum Dots Incorporated into a Thin Film Nanocomposite Membrane with High Flux and Antifouling Properties for Low-Pressure Nanofiltration. *ACS Applied Materials & Interfaces* **2017**, *9* (12), 11082-11094.
101. Bouša, D.; Friess, K.; Pilnáček, K.; Vopička, O.; Lanč, M.; Fónod, K.; Pumera, M.; Sedmidubský, D.; Luxa, J.; Sofer, Z., Thin, High-Flux, Self-Standing, Graphene Oxide Membranes for Efficient Hydrogen Separation from Gas Mixtures. *Chemistry – A European Journal* **2017**, *23* (47), 11416-11422.
102. De Faria, A. F.; Perreault, F.; Shaulsky, E.; Arias Chavez, L. H.; Elimelech, M., Antimicrobial Electrospun Biopolymer Nanofiber Mats Functionalized with Graphene Oxide-Silver Nanocomposites. *ACS Applied Materials and Interfaces* **2015**, *7* (23), 12751-12759.
103. Bano, S.; Mahmood, A.; Kim, S.-J.; Lee, K.-H., Graphene oxide modified polyamide nanofiltration membrane with improved flux and antifouling properties. *Journal of Materials Chemistry A* **2015**, *3* (5), 2065-2071.
104. Zhuo, S.; Shao, M.; Lee, S.-T., Upconversion and Downconversion Fluorescent Graphene Quantum Dots: Ultrasonic Preparation and Photocatalysis. *ACS Nano* **2012**, *6* (2), 1059-1064.
105. Liu, Y.; Kim, D. Y., Ultraviolet and blue emitting graphene quantum dots synthesized from carbon nano-onions and their comparison for metal ion sensing. *Chemical Communications* **2015**, *51* (20), 4176-4179.
106. Zeng, Z.; Yu, D.; He, Z.; Liu, J.; Xiao, F.-X.; Zhang, Y.; Wang, R.; Bhattacharyya, D.; Tan, T. T. Y., Graphene Oxide Quantum Dots Covalently Functionalized PVDF Membrane with Significantly-Enhanced Bactericidal and Antibiofouling Performances. **2016**, *6*, 20142.
107. Zhang, P.; Zhao, X.; Ji, Y.; Ouyang, Z.; Wen, X.; Li, J.; Su, Z.; Wei, G., Electrospinning graphene quantum dots into a nanofibrous membrane for dual-purpose fluorescent and electrochemical biosensors. *Journal of Materials Chemistry B* **2015**, *3* (12), 2487-2496.
108. Nishiyama, Y.; Langan, P.; Chanzy, H., Crystal Structure and Hydrogen-Bonding System in Cellulose I β from Synchrotron X-ray and Neutron Fiber Diffraction. *Journal of the American Chemical Society* **2002**, *124* (31), 9074-9082.

109. Klemm, D.; Heublein, B.; Fink, H.-P.; Bohn, A., Cellulose: Fascinating Biopolymer and Sustainable Raw Material. *Angewandte Chemie International Edition* **2005**, *44* (22), 3358-3393.
110. Fink, H. P.; Weigel, P.; Purz, H. J.; Ganster, J., Structure formation of regenerated cellulose materials from NMMO-solutions. *Progress in Polymer Science* **2001**, *26* (9), 1473-1524.
111. Anokhina, T. S.; Yushkin, A. A.; Makarov, I. S.; Ignatenko, V. Y.; Kostyuk, A. V.; Antonov, S. V.; Volkov, A. V., Cellulose composite membranes for nanofiltration of aprotic solvents. *Petroleum Chemistry* **2016**, *56* (11), 1085-1092.
112. Shen, T.; Gnanakaran, S., The Stability of Cellulose: A Statistical Perspective from a Coarse-Grained Model of Hydrogen-Bond Networks. *Biophysical Journal* *96* (8), 3032-3040.
113. Swatloski, R. P.; Spear, S. K.; Holbrey, J. D.; Rogers, R. D., Dissolution of Cellulose with Ionic Liquids. *Journal of the American Chemical Society* **2002**, *124* (18), 4974-4975.
114. Isik, M.; Sardon, H.; Mecerreyes, D., Ionic Liquids and Cellulose: Dissolution, Chemical Modification and Preparation of New Cellulosic Materials. *International Journal of Molecular Sciences* **2014**, *15* (7), 11922-11940.
115. Livazovic, S.; Li, Z.; Behzad, A. R.; Peinemann, K. V.; Nunes, S. P., Cellulose multilayer membranes manufacture with ionic liquid. *Journal of Membrane Science* **2015**, *490*, 282-293.
116. Anokhina, T. S.; Pleshivtseva, T. S.; Ignatenko, V. Y.; Antonov, S. V.; Volkov, A. V., Fabrication of composite nanofiltration membranes from cellulose solutions in an [Emim]OAc–DMSO mixture. *Petroleum Chemistry* **2017**, *57* (6), 477-482.
117. Sukma, F. M.; Çulfaz-Emecen, P. Z., Cellulose membranes for organic solvent nanofiltration. *Journal of Membrane Science* **2018**, *545*, 329-336.
118. Yeh, T.-F.; Huang, W.-L.; Chung, C.-J.; Chiang, I. T.; Chen, L.-C.; Chang, H.-Y.; Su, W.-C.; Cheng, C.; Chen, S.-J.; Teng, H., Elucidating Quantum Confinement in Graphene Oxide Dots Based On Excitation-Wavelength-Independent Photoluminescence. *The Journal of Physical Chemistry Letters* **2016**, *7* (11), 2087-2092.
119. Kosan, B.; Michels, C.; Meister, F., Dissolution and forming of cellulose with ionic liquids. *Cellulose* **2008**, *15* (1), 59-66.
120. Sescousse, R.; Le, K. A.; Ries, M. E.; Budtova, T., Viscosity of Cellulose–Imidazolium-Based Ionic Liquid Solutions. *The Journal of Physical Chemistry B* **2010**, *114* (21), 7222-7228.
121. Yu Xing, D.; Peng, N.; Chung, T.-S., *Formation of Cellulose Acetate Membranes via Phase Inversion Using Ionic Liquid, [BMIM]SCN, As the Solvent*. 2010; Vol. 49.
122. Xing, D. Y.; Peng, N.; Chung, T.-S., Investigation of unique interactions between cellulose acetate and ionic liquid [EMIM]SCN, and their influences on hollow fiber ultrafiltration membranes. *Journal of Membrane Science* **2011**, *380* (1), 87-97.
123. Suzuki, N.; Wang, Y.; Elvati, P.; Qu, Z.-B.; Kim, K.; Jiang, S.; Baumeister, E.; Lee, J.; Yeom, B.; Bahng, J. H.; Lee, J.; Violi, A.; Kotov, N. A., Chiral Graphene Quantum Dots. *ACS Nano* **2016**, *10* (2), 1744-1755.
124. Werner, C.; Körber, H.; Zimmermann, R.; Dukhin, S.; Jacobasch, H.-J., Extended Electrokinetic Characterization of Flat Solid Surfaces. *Journal of Colloid and Interface Science* **1998**, *208* (1), 329-346.

125. Sato, Y.; Kusaka, Y.; Kobayashi, M., Charging and Aggregation Behavior of Cellulose Nanofibers in Aqueous Solution. *Langmuir* **2017**, *33* (44), 12660-12669.
126. Petrinić, I.; Bukšek, H.; Luxbacher, T.; Pušić, T.; Bischof, S., Influence of the structure of polymer fiber composites on the analysis of the zeta potential. *Journal of Applied Polymer Science* **2018**, *135* (21), 46227.
127. Edwards, J. V.; Howley, P.; Prevost, N.; Condon, B.; Arnold, J.; Diegelmann, R., Positively and negatively charged ionic modifications to cellulose assessed as cotton-based protease-lowering and hemostatic wound agents. *Cellulose* **2009**, *16* (5), 911-921.
128. Konkena, B.; Vasudevan, S., Understanding Aqueous Dispersibility of Graphene Oxide and Reduced Graphene Oxide through pKa Measurements. *The Journal of Physical Chemistry Letters* **2012**, *3* (7), 867-872.
129. Chen, J.-T.; Fu, Y.-J.; An, Q.-F.; Lo, S.-C.; Huang, S.-H.; Hung, W.-S.; Hu, C.-C.; Lee, K.-R.; Lai, J.-Y., Tuning nanostructure of graphene oxide/polyelectrolyte LbL assemblies by controlling pH of GO suspension to fabricate transparent and super gas barrier films. *Nanoscale* **2013**, *5* (19), 9081-9088.
130. Szymczyk, A.; Dirir, Y. I.; Picot, M.; Nicolas, I.; Barrière, F., Advanced electrokinetic characterization of composite porous membranes. *Journal of Membrane Science* **2013**, *429* (Supplement C), 44-51.
131. Chartrand, A.; Lavoie, J.-M.; Huneault, M. A., Surface modification of microcrystalline cellulose (MCC) and its application in LDPE-based composites. *Journal of Applied Polymer Science* **2017**, *134* (1), n/a-n/a.
132. Steele, D. F.; Moreton, R. C.; Staniforth, J. N.; Young, P. M.; Tobby, M. J.; Edge, S., Surface Energy of Microcrystalline Cellulose Determined by Capillary Intrusion and Inverse Gas Chromatography. *The AAPS Journal* **2008**, *10* (3), 494-503.
133. Wang, S.; Zhang, Y.; Pang, G.; Zhang, Y.; Guo, S., Tuning the Aggregation/Disaggregation Behavior of Graphene Quantum Dots by Structure-Switching Aptamer for High-Sensitivity Fluorescent Ochratoxin A Sensor. *Analytical Chemistry* **2017**, *89* (3), 1704-1709.
134. Wang, X.; Zhang, L.; Sun, D.; An, Q.; Chen, H., Effect of coagulation bath temperature on formation mechanism of poly(vinylidene fluoride) membrane. *Journal of Applied Polymer Science* **2008**, *110* (3), 1656-1663.
135. Durmaz, E. N.; Zeynep Çulfaz-Emecen, P., Cellulose-based membranes via phase inversion using [EMIM]OAc-DMSO mixtures as solvent. *Chemical Engineering Science* **2018**, *178*, 93-103.
136. Adani, F.; Papa, G.; Schievano, A.; Cardinale, G.; D'Imporzano, G.; Tambone, F., Nanoscale Structure of the Cell Wall Protecting Cellulose from Enzyme Attack. *Environmental Science & Technology* **2011**, *45* (3), 1107-1113.
137. Colwell, R. R.; Huq, A.; Islam, M. S.; Aziz, K. M. A.; Yunus, M.; Khan, N. H.; Mahmud, A.; Sack, R. B.; Nair, G. B.; Chakraborty, J.; Sack, D. A.; Russek-Cohen, E., Reduction of cholera in Bangladeshi villages by simple filtration. *Proceedings of the National Academy of Sciences of the United States of America* **2003**, *100* (3), 1051-1055.
138. Lonsdale, H. K.; Merten, U.; Riley, R. L., Transport properties of cellulose acetate osmotic membranes. **1965**, *9* (4), 1341-1362.
139. Yang, G.; Xiong, X.; Zhang, L., Microporous formation of blend membranes from cellulose/konjac glucomannan in NaOH/thiourea aqueous solution. *Journal of Membrane Science* **2002**, *201* (1), 161-173.

140. Mao, Z.; Cao, Y.; Jie, X.; Kang, G.; Zhou, M.; Yuan, Q., Dehydration of isopropanol–water mixtures using a novel cellulose membrane prepared from cellulose/N-methylmorpholine-N-oxide/H₂O solution. *Separation and Purification Technology* **2010**, *72* (1), 28-33.
141. Chen, H. Z.; Wang, N.; Liu, L. Y., Regenerated cellulose membrane prepared with ionic liquid 1-butyl-3-methylimidazolium chloride as solvent using wheat straw. *Journal of Chemical Technology and Biotechnology* **2012**, *87* (12), 1634-1640.
142. Lu, Y.; Liu, Y. X.; Yu, H. P.; Sun, Q. F., Preparation, characterization and biocompatibility of regenerated cellulose/PVA blend membranes in 1-allyl-3-methylimidazolium chloride. In *Materials Science and Engineering, Pts 1-2*, Zhu, G., Ed. 2011; Vol. 179-180, pp 1108-1111.
143. Lei, L.; Lindbråthen, A.; Sandru, M.; Gutierrez, M.; Zhang, X.; Hillestad, M.; He, X., Spinning Cellulose Hollow Fibers Using 1-Ethyl-3-methylimidazolium Acetate–Dimethylsulfoxide Co-Solvent. **2018**, *10* (9), 972.
144. Tian, M. W.; Qu, L. J.; Zhang, X. S.; Zhang, K.; Zhu, S. F.; Guo, X. Q.; Han, G. T.; Tang, X. N.; Sun, Y. N., Enhanced mechanical and thermal properties of regenerated cellulose/graphene composite fibers. *Carbohydrate Polymers* **2014**, *111*, 456-462.
145. Yang, J.; Zhang, E. W.; Li, X. F.; Zhang, Y. T.; Qu, J.; Yu, Z. Z., Cellulose/graphene aerogel supported phase change composites with high thermal conductivity and good shape stability for thermal energy storage. *Carbon* **2016**, *98*, 50-57.
146. Shi, H. C.; Li, W. S.; Zhong, L.; Xu, C. J., Methylene Blue Adsorption from Aqueous Solution by Magnetic Cellulose/Graphene Oxide Composite: Equilibrium, Kinetics, and Thermodynamics. *Industrial & Engineering Chemistry Research* **2014**, *53* (3), 1108-1118.
147. Bengani-Lutz, P.; Converse, E.; Cebe, P.; Asatekin, A., Self-Assembling Zwitterionic Copolymers as Membrane Selective Layers with Excellent Fouling Resistance: Effect of Zwitterion Chemistry. *ACS Applied Materials & Interfaces* **2017**, *9* (24), 20859-20872.
148. Zhao, J.; Baba, T.; Mori, H.; Shimizu, K., Effect of zwf gene knockout on the metabolism of Escherichia coli grown on glucose or acetate. *Metab Eng* **2004**, *6* (2), 164-74.
149. Chao, Y.; Zhang, T., Optimization of fixation methods for observation of bacterial cell morphology and surface ultrastructures by atomic force microscopy. *Appl Microbiol Biotechnol* **2011**, *92* (2), 381-92.
150. Kim, B.-K.; Lee, E. J.; Kang, Y.; Lee, J.-J., Application of ionic liquids for metal dissolution and extraction. *Journal of Industrial and Engineering Chemistry* **2018**, *61*, 388-397.
151. Kongdee, A.; Bechtold, T., The complexation of Fe(III)-ions in cellulose fibres: a fundamental property. *Carbohydrate Polymers* **2004**, *56* (1), 47-53.
152. Davenport, M. D.; Gui, M.; Ormsbee, R. L.; Bhattacharyya, D., Development of PVDF Membrane Nanocomposites via Various Functionalization Approaches for Environmental Applications. *Polymers* **2016**, *8* (2).
153. Houtman, C. J.; Atalla, R. H., Cellulose-Lignin Interactions (A Computational Study). *Plant physiology* **1995**, *107* (3), 977-984.

154. Kernan, C.; Chow, P. P.; Christianson, R. J.; Huang, J., Experimental and Computational Investigation of Biofilm Formation by *Rhodopseudomonas palustris* Growth under Two Metabolic Modes. *PLOS ONE* **2015**, *10* (6), e0129354.
155. Nguyen, T.; Roddick, F. A.; Fan, L., Biofouling of water treatment membranes: a review of the underlying causes, monitoring techniques and control measures. *Membranes* **2012**, *2* (4), 804-840.
156. Zhang, F.; Wu, Y.; Li, W.; Xing, W.; Wang, Y., Depositing lignin on membrane surfaces for simultaneously upgraded reverse osmosis performances: An upscalable route. **2017**, *63* (6), 2221-2231.

VITA

Andrew Colburn graduated Magna Cum Laude with a B.S. in Chemical Engineering from the University of Kentucky in 2009. In 2013 he began his PhD work at the University of Kentucky continuing research he began in his last semester of his undergraduate studies.

Awards

AIChE Separations Division

2018 Graduate Student Research Award for Membranes

North American Membrane Society Student Poster Competition

Third Place Liquids Division (2018), Honorable Mention Membrane Processes Division (2015)

Imagine Membrane Conference and ECI: Advanced Membrane Technology VII
Student Poster Award (2016 and 2017)

Publications

Andrew Colburn, RJ Vogler, Mariah Bezold, John Craven, Dibakar Bhattacharyya
Advancing in Lignocellulosic Membranes: New Composite Materials Modify Selectivity and Add Functionality to Membrane Surface, *Journal of Membrane Science*, December 2018, *To be submitted*

Andrew Colburn, Namal Wanninayake, Doo Young Kim, Dibakar Bhattacharyya,
Cellulose Graphene Quantum Dot Composite Membranes Using Ionic Liquid, *Journal of Membrane Science*, Volume 566, 15 June 2018, Pages 293-302, <https://doi.org/10.1016/j.memsci.2018.04.009>

Andrew Colburn, Noah Meeks, Steven Weinman, and Dibakar Bhattacharyya, **High Total Dissolved Solids Water Treatment by Charged Nanofiltration Membranes Relating to Power Plant Applications**, *Industrial & Engineering Chemistry Research*, 2016, 55 (14), <http://dx.doi.org/10.1021/acs.iecr.6b00098>

Minghui Gui, Joseph K. Papp, Andrew S. Colburn, Noah D. Meeks, Benjamin Weaver, Ilan Wilf, Dibakar Bhattacharyya, **Engineered iron/iron oxide functionalized membranes for selenium and other toxic metal removal from power plant scrubber water**, *Journal of Membrane Science*, Volume 488, 15 August 2015, Pages 79-91, <http://dx.doi.org/10.1016/j.memsci.2015.03.089>.

Publications (cont.)

Ashish Aher, Joseph Papp, Andrew Colburn, Hongyi Wan, Evan Hatakeyama, Prakhar Prakash, Ben Weaver, Dibakar Bhattacharyya, **Naphthenic acids removal from high TDS produced water by persulfate mediated iron oxide functionalized catalytic membrane, and by nanofiltration**, Chemical Engineering Journal, Volume 327, 2017, Pages 573-583, <https://dx.doi.org/10.1016/j.cej.2017.06.128>

Selected Conference Presentations

A. Colburn, M. Bezold, D. Bhattacharyya, **Lignocellulosic Materials for Nanofiltration Membrane Synthesis**, AIChE National Conference, Pittsburgh, PA, October 2018.

A. Colburn, N. Wanninayake, D.Y. Kim, D. Bhattacharyya, **Graphene quantum dot modification of cellulose membrane pores**, International Congress on Membranes, San Francisco, CA, July 2017.

A. Colburn, N. Wanninayake, D.Y. Kim, D. Bhattacharyya, **Fouling and Scaling Behavior of Charged Nanofiltration Membranes and the Influence of Graphene Quantum Dot Surface Modification**, North American Membrane Society Annual Meeting, Bellevue, WA, June 2016.

A. Colburn, M. Gui, D. A. Whitehead, D. Bhattacharyya, **Integrated NF and Functionalized Membranes for Industrial Water Reuse: Role of Gypsum Precipitation and High Hardness**, North American Membrane Society Annual Meeting, Boston, MA, May 2015.